Investigations of the Triple-GEM-Tracking Detector for COMPASS++/AMBER

Karl Jonathan Flöthner

Masterarbeit in Physik
angefertigt im Helmholtz-Institut für Strahlen- und Kernphysik

vorgelegt der
Mathematisch-Naturwissenschaftlichen Fakultät
der
Rheinischen Friedrich-Wilhelms-Universität
Bonn

November 2020

I hereby declare that this thesis was formulated by myself and that no sources or tools other than those cited were used.

Bonn, 02.11.2020 ....

Date Signature

1. Gutachter: Prof. Dr. Bernhard Franz Ketzer
2. Gutachter: Prof. Dr. Jochen Dingfelder

Acknowledgements

First of all I would like to thank Prof. Bernhard Ketzer who gives me the opportunity to work for one year on this unique master thesis. The chance to contribute as a main part of the COMPASS upgrade is for sure not usual for a master student.
I also would like to thank Prof. Jochen Dingfelder for being the second reviewer.
Furthermore, I would like to thank the entire AG-Ketzer which has regarded me as a member of the team from day one on. The hardware group in particular was always ready to help and clarify questions. One of the biggest help was the always good mood, which helped to keep the work-work balance without any problems.
Especially I would like to thank C. Honisch for his expertise on electronics and its design. He supported me although he is not a part of the AG-Ketzer.
Additionally, I would like to thank M. Hoesgen, M. Ball and M. Lupberger[1] for their steady support either concerning general issues or measurements.
This thesis would not be fine tuned without all persons mentioned before and last but not least P. Hauer.
Furthermore, I would like to thank my family for their unconditional support. Special thanks go to my mother which enabled me to fully focus on my studies.

Finally and very particularly I would like to thank HannaH. You have always supported me and stayed by my side till the end. Many thanks that you believed in me and for all the encouragement you gave me on this journey!

[1] One could say three Ms for Karl

Contents

CHAPTER 1

Introduction

In modern particle detector physics, gas-based detectors have become a widely used element. Reasons for that are on the one hand the possibility to cover large volumes with active medium and low dead detector material. On the other hand this detector type is rather radiation hard because the gas that is used to interact with particles is in a continuous flow. Thus, radiation damages of the active medium are negligible. Furthermore, gas-based detectors are cheaper compared to semiconductors regarding production costs.
The concept of this detector was revolutionised by the change from classical wire techniques, e.g. like in a **MWPC** (**M**ulti **W**ire **P**roportional **C**hamber), to modern **MPGD**s (**M**icro **P**attern **G**aseous **D**etector). By setting new limits with micropatterns it gets possible to achieve excellent spatial and time resolution.
One concept of the MPGD-zoo[1] which has shown a wide range of usability with excellent performance is the **GEM** (**G**as **E**lerctron **M**ultiplier). As a standalone amplification stage without a fixed readout one has several possibilities for the design of a GEM-based detector.
In addition, one is not bound to a certain readout which allows the customisation adapted to the purpose. Therefore, detectors based on an amplification consisting of three GEM stages with either strip or pixel readout are commonly used.
One pioneer experiment for this detector type is the COMPASS experiment located at CERN. It was the first large experiment that has implemented a set of large area triple-GEM-tracking detectors for the tracking system. With an continuous urge to further develop this special detector setup, the development is still ongoing.
In this thesis the development towards a new generation of a triple-GEM-tracking detector is done. The aim is to introduce a complete new design of the whole detector granting a proper replacement of the first generation and preparing for huge steps towards further generations e.g. the usage of self-triggered readout to measure at higher rates.
Therefore, this thesis treats the individual components and their introduced advantages compared to previous generations. Before starting with the main part the physics background and especially the working principle of a GEM is explained in chapter 2. Because of the long time in operation for such a detector there is section 2.4 dealing with ageing and material choice.
To understand the aim of the new design the COMPASS experiment and its planned upgrade is introduced in chapter 3.

[1] At the beginning of the MPGDs many different types and structures were invented - the "zoo"

After that the development of the triple-GEM-tracking detectors of the experiment are discussed in chapter 4. Therefore, firstly the working principle of such a detector is discussed to understand the design of the first generation. This is explained in detail in section 4.1. Reasons for a first development towards a second generation and its design is then outlined in section 4.2. Finally, the third generation is introduced in section 4.3.

A detailed explanation of this design is given in chapter 5. The complete mechanical design and its properties are discussed in section 5.1. This contains the used support plates and spacer frames. Moreover, the design of the foils (GEM, drift and readout) are outlined in section 5.2. The required equipment to build the detector - including the quality assurance - is explained in section 5.3. Finally, the used electronics regarding the stabilized voltage divider and the designed readout chain are characterised in section 5.4 and 5.5.

The last part of the thesis (chapter 6) deals with conducted measurements concerning the new **APV** (**A**nalog **P**ipeline **V**oltage) front-end which is a part of the new readout chain.

CHAPTER 2

Physics Background

This chapter covers topics of interest for the understanding of the following work. It deals mainly with topics connected to gas-filled detectors, their construction and their mode of operation. First the nomenclature for high energy physics will be introduced in section 2.1. Processes inside the detector will be discussed in section 2.2.1 to understand the principle of gas-based trackers. Furthermore, the GEM will be explained in detail in section 2.3. This is done with respect to the design of the new triple-GEM-tracking detector, outlined in chapter 5. The last section 2.4 of this chapter gives a look into ageing of gaseous detectors which is important by the choice of materials.

2.1 Relativistic Units in High-Energy-Physics

This section clarifies some typical nomenclature which is commonly used in high energy physics and also in this thesis. As Einstein explains in "The Foundation of the General Theory of Relativity" [1], Newtonian mechanics cannot be applied for speeds near the speed of light. This results in so-called relativistic corrections which prohibit that some objects with mass can reach the speed of light. It shall be specified and defined as follows:

$$
\begin{aligned}
&\epsilon_0, \hbar, c = 1 && = \text{use of natural units} \\
&\beta = \tfrac{v}{c} (= v) && = \text{relativistic velocity} \\
&\gamma = \tfrac{1}{\sqrt{1-\beta^2}} && = \text{Lorentz-factor} \\
&p = \gamma m_0 v && = \text{relativistic momentum} \\
&E = \sqrt{p^2 - m_0^4} && = \text{total energy} \\
&\beta\gamma = \tfrac{p}{m} && = \text{useful relation by use of natural units}
\end{aligned}
$$

In physics derivations are often done in natural units, which simplifies many expressions and calculations. With proper use of $\hbar c \approx 200\,\mathrm{MeV\,fm}$, the corresponding quantities can be converted to SI-units.

2.2 Energy Loss in Matter of charged Particles and Photons

If a charged particle traverses through a medium, it interacts along the path and looses energy. This is needed to generate a measurable signal in all detectors. As long as one cannot detect any energy loss from a particle it is invisible and thus not observable[1].

2.2.1 Charged Particles Interaction

As a common approach the mean energy loss of charged particles in matter can be described by the Bethe equation [2], see equation 2.1. Here it is important to mention that the energy loss underlies statistical fluctuations, since it is mainly based on collisions of charged particles which is a statistical process. Therefore, one has to clarify that defining an average requires fluctuations in a certain frame.

$$\left\langle -\frac{dE}{dx} \right\rangle = \frac{4\pi}{(4\pi\epsilon_0)^2} \frac{z^2 e^4 n_\mathrm{e}}{m_\mathrm{e} c^2 \beta^2} \left[\frac{1}{2} \ln \frac{2m_\mathrm{e} c^2 \beta^2 \gamma^2 T_\mathrm{max}}{I^2} - \beta^2 - \frac{\delta(\beta\gamma)}{2} \right] \tag{2.1}$$

where:

ϵ_0	= vacuum permittivity
ze	= charge of incoming particle
$n_\mathrm{e} = \frac{Z}{A} N_\mathrm{A} \rho$	= electron number density of material
m_e	= electron mass
$\beta = \frac{v}{c}$	= velocity of incoming particle
γ	= relativistic Lorentz factor
$T_\mathrm{max} \underset{M \gg 2m_\mathrm{e}\gamma}{\simeq} 2m_\mathrm{e} v^2 \gamma^2$	= maximum kinetic energy imparted to one electron in a single collision
I	= mean excitation energy
$\delta(\beta\gamma)$	= density effect correction

Figure 2.1 shows the characteristics of the Bethe curve. For small values of $\beta\gamma$, the mean energy loss decreases with $1/\beta^2$. For $\beta\gamma \approx 3$ the mean energy loss reaches a minimum. A particle with this energy is called **MIP** (**M**inimal **I**onizing **P**article). For higher values of $\beta\gamma$, the curve rises logarithmically. A more detailed explanation can be found in [3].

[1] $E_\text{t-miss}$ would be an exception under specific assumptions

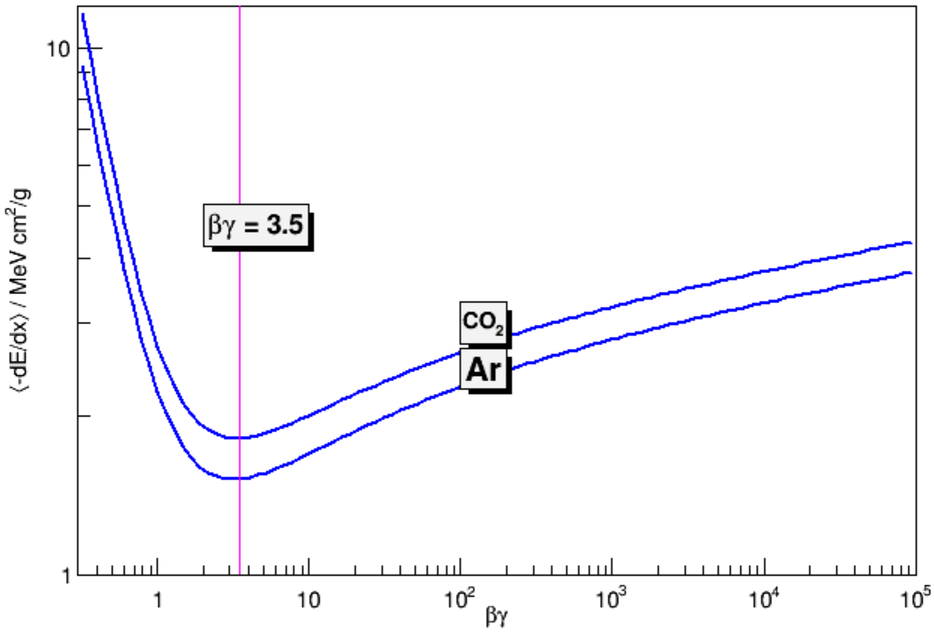

Figure 2.1: Mean-Energy-Loss of charged particles in different media.

2.2.2 Photon interaction

In general, there are three effects which describe the interaction of photons with matter. A schematic representation can be found in fig. 2.2. Thereby, a common quantity to classify the cross sections is the reduced photon energy $\epsilon = E_\gamma/(m_e c^2)$ [4].

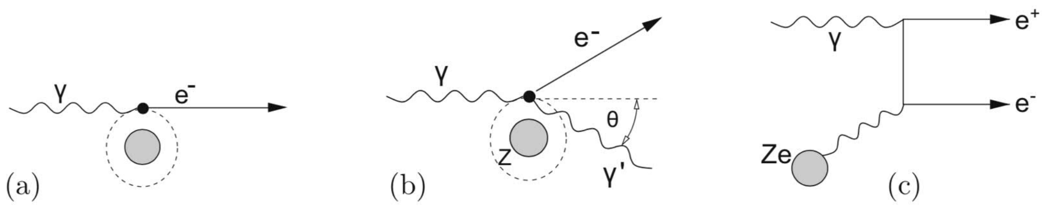

Figure 2.2: Schematic representation: (a) photoelectric effect (b) Compton effect and (c) pair production [3].

Photoelectric effect:

A photon with frequency ν and energy $E_\gamma = h\nu \geq E_A$, where E_A is the release energy of the electron, is absorbed and the released electron receives the remaining energy as free kinetic energy, $E_{kin} = E_\gamma - E_A$. For the effective cross section in the energy range between K-absorption edge ϵ_k and $\epsilon = 1$ one finds approximately [4]: $\sigma_{Ph} \propto \frac{Z^5}{\epsilon^{7/2}}$, with Z the nuclear charge number of the absorber.
At high photon energies $\epsilon \gg 1$ the approximation [4] $\sigma_{Ph} \propto \frac{Z^5}{\epsilon}$ is valid.

Compton effect:

When a photon hits a free or quasi-free electron a part of the momentum is transferred to the electron. The binding energy is thereby neglected. The wavelength of the photon (and therefore the energy) changes by $\Delta\lambda = \lambda_0(1 - \cos(\Theta))$, where Θ is the deflection angle and λ_0 is the Compton wavelength. The maximum pulse transfer is at a deflection angle of $\Theta = 180\,^\circ$.
The scattering cross section per electron for the boundary in case of low photon energy is given by the classical Thomson formula [4], with $\sigma_{\mathrm{Th}} = 0.665\,\mathrm{b}$. Two extreme cases of the Klein-Nishina cross section are considered. For $\epsilon \ll 1$ the following applies [4]: $\sigma_{\mathrm{c}} = \sigma_{\mathrm{Th}}(1 - \epsilon)$.
In the case of $\epsilon \gg 1$ it is more complex [4]: $\sigma_{\mathrm{c}} = \frac{3}{8\epsilon}\sigma_{\mathrm{Th}}(\frac{1}{2} + \ln 2\epsilon)$.

Pair production:

If the photon has an energy $E_\gamma \geq 2m_{\mathrm{e}}c^2$ it can produce an electron-positron pair near the nucleus of an atom[2]. Thereby, the entire photon energy is absorbed and the surplus $E_\gamma - 2m_{\mathrm{e}}c^2$ is used as kinetic energy.
For the effective cross section, in the range $1 < \epsilon < 137Z^{-\frac{1}{3}}$, the following approximation applies [5]: $\sigma_{\mathrm{Pb}} \propto Z^2 \ln(2\epsilon)$

2.3 Gas Electron Multiplier

After the invention of the gas amplification principle decades ago, gas-based detectors are still widely used and no end of further possible developments is seen.
The last huge step was the development of MPGD which replaces wire-based detectors. The main characteristic is the fixed connection of insulator and conductor, which allows high voltages without any displacement of electrodes what was a limiting factor for wires. Therefore, this detector type can achieve outstanding spatial and time resolutions while simultaneously being highly radiation resistant [6]. Additionally, they are suitable for high rate capabilities and can longer operate in experiments because of low ageing when they were used under right conditions (ageing is mostly caused by impurities of other detector materials as discussed in section 2.4) [7].
Due to their wide range of possibilities they are not only used in particle physics but also e.g. in medicine [8].
One commonly used type of MPGDs is the **GEM** (**G**as **E**lectron **M**ultiplier) which was introduced in the late nineties by F. Sauli[3] [11]. Because they can cover large areas many experiments are using them or plan to use them in future upgrades (e.g. COMPASS, LHCb, TOTEM, JLab Hall A, ALICE and CMS [12]).
A GEM foil is a perforated composite with a polyimide core between thin copper layers. Looking at a single hole, fig. 2.3, one can see the typical double conical shape.

[2] The reason for this is the energy-momentum-conservation

[3] Officialy introduced in 1997 but there can be found also some previous publications: e.g. [9][10]

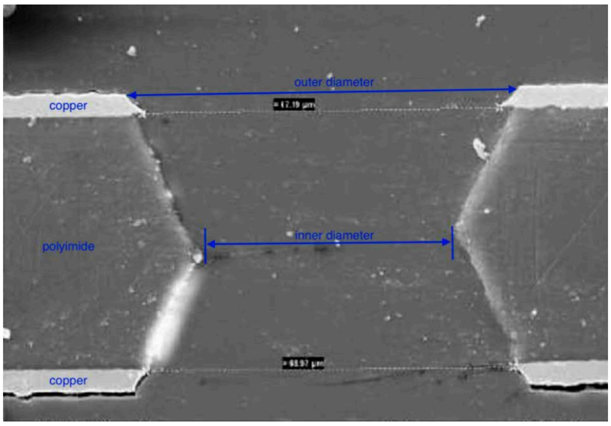

Figure 2.3: Cut through a single hole [13].

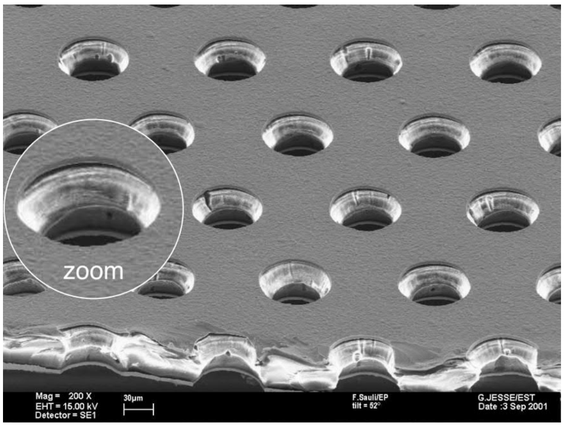

Figure 2.4: Section of a GEM foil [13].

The structure of hole distribution is typically hexagonal, as one can see in fig. 2.4. This leads to a pattern whereby all adjacent holes have the same distance from their neighbours. Both, fig. 2.4 and fig. 2.3, were taken with an electron microscope, to get a good resolution of the foils with a total thickness of 60 µm.

2.3.1 Manufacturing Process

The production of a GEM foil starts with a high-quality polymer foil (typ. 50 µm thick polyimide) with thin metal-clad on both sides (typ. 5 µm thin copper). Via photolithography it is possible to obtain 10^4 holes cm^{-2}. Fig. 2.5 shows two manufacturing processes which is on the one hand the double mask technique and on the other the single mask technique. The hole pattern is brought to the surface with UV-light exposure through the mask. Therefore, the foil was laminated with a photoresistive resin beforehand. After developing, the first metal chemical etching[4] follows. Now the holes in the copper are used as masks for the polymer etching[5]. By this step one can already see the typical shape of a double conical GEM for the double mask technique. Here the single mask process requires an additional metal etching to remove the copper which is left at the bottom of the holes. For a proper use of the foils a second masking to define electrodes[6] and the corresponding last metal etching are performed.
Each technique has its own benefits. As depicted in fig. 2.5 the hole geometry[7] is more symmetric for the double mask technique. The downside is that the two masks need a precise alignment to achieve homogeneous geometries over the whole foil. This makes it rather impossible to produce foils larger than 40 cm × 40 cm [14]. Here the single mask technique becomes relevant, since the alignment of the masks no longer limits the process.

[4] Copper etching with: $FeCL_3$ + HCl, chromic acid H_2CrO_4 and Ammoniumpersulfate $(NH_4)_2S_2O_8$
[5] Polyimide etching with: Ethylendiamine $C_2H_8N_2$ and KOH
[6] Also used to remove dead copper from the foils
[7] Not to be underrated, as the shape influences the performance - e.g. the gain

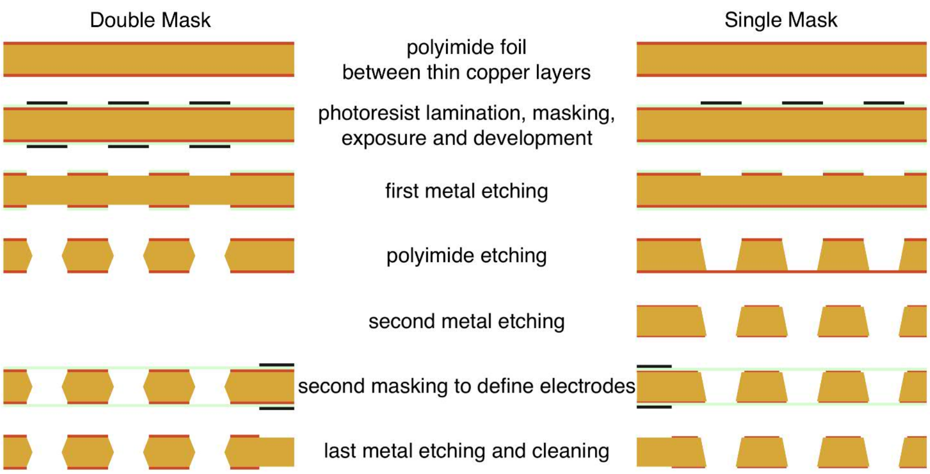

Figure 2.5: Schematic representation of the main GEM foil etching processes [14].Left the double mask technique is shown and on the right side the single mask technique.

2.3.2 Characteristics and Operating Principle

The basic idea of a GEM is described in the following.
By applying a certain voltage difference between the two copper layers one creates an electric field in the holes which is strong enough to accelerate free electrons, such that they can ionise the gas and ending up to an avalanche effect and an effective multiplication of the incoming charge.
The parameter for the degree of amplification is called gain. A simulation of the process can be seen in fig. 2.7. Due to the insulator between the metal layers the electric field and corresponding amplifications only occur inside the holes. Therefore, the GEM is a great standalone amplification stage and can be staged in cascades to decrease the voltage difference across a single stage by maintaining the overall gain. This is commonly done in a triple GEM configuration.
Additionally, this allows a huge flexibility of the readout which is separated to the amplification process.
After amplification in the GEM holes the avalanche-ions drift back towards the cathode and one obtains a fast electron signal[8] proportional to the incoming charge above the anode.

[8] Without slow ion tail because of the shielding from the GEM itself

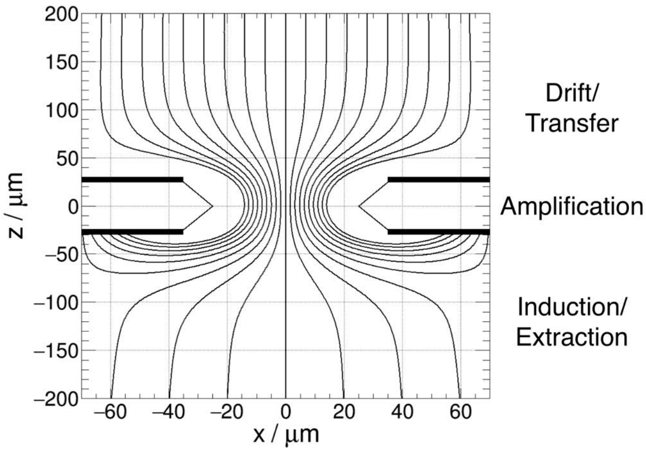

Figure 2.6: Electric field lines of a single GEM hole [15] with common used names for the fields to the right.

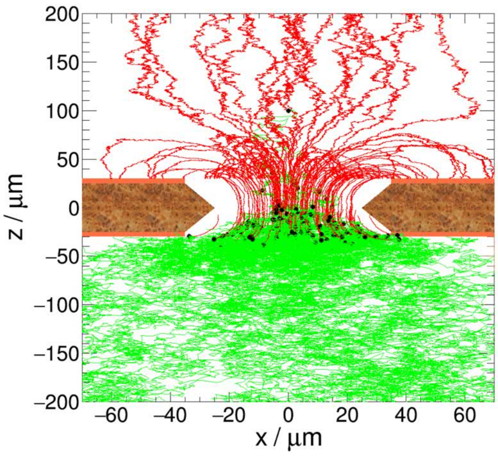

Figure 2.7: Simulated GEM hole [15]. Black dot means ionisation, red depicts the ions and green the electrons.

Having a closer look at the field lines in fig. 2.6 it gets more complicated. Here one sees that some of them ending up on the copper which leads to loss of charges and thus the gain has to be corrected. That some of the charges should end up on the metal surface[9] can also be seen in fig. 2.6. Therefore an effective gain G_{eff} will be defined [15]:

$$G_{\text{eff}} = \epsilon_{\text{coll}} G_{\text{abs}} \epsilon_{\text{extr}} \tag{2.2}$$

where:

G_{eff} = effective gain
ϵ_{coll} = collection efficiency (percentage of collected electrons/ions)
G_{abs} = absolute gain
ϵ_{extr} = extrection efficiency

This holds for electrons and ions. Normally one tries to achieve high efficiencies for electrons with simultaneously small ion efficiencies[10]. Therefore, it is necessary to tune the efficiencies by changing the ratios of the corresponding fields. Concrete simulations for different setups can be found in [15]. In addition it is possible to use multiple GEM stages to achieve higher gains at lower GEM voltages which results in a better discharge prevention, as shown in fig. 4.2.
Another way to change the detector performance would be the combination of different MPGDs, which is than called a hybrid. Here a detailed calculation for different multi-stage MPGDs in modelling charge transfer and energy resolution can be found in [17].
For an optimised usage of a GEM-based readout one can also vary the design parameters of the holes, see fig. 2.8 and fig. 2.9. For example, a standard GEM has an outer diameter of 70 µm and inner of 50 µm. Thereby, the pitch is 140 µm.

[9] Charges collected on the polyimide result in a local change of the electric field, alias the charge up effect [12]
[10] Low ion efficiencies lead to a small ion backflow which is especially interesting for a GEM based TPC [16]

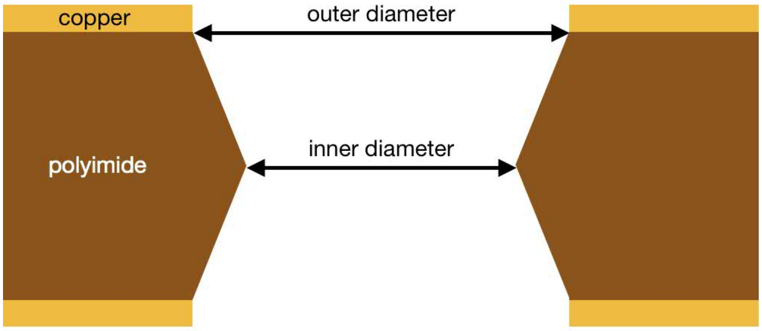

Figure 2.8: Schematic view of a single hole.

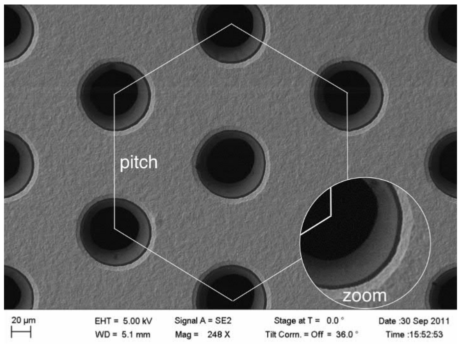

Figure 2.9: Top view of a GEM foil [2].

Because of the wide spectrum of modifications to construct a reasonable detector for special requirements GEM-based detectors also find applications beside particle physics as mentioned in the beginning of this section.

2.4 Ageing and Material Choice

This section gives an idea why one has to be careful by choosing the gas mixture and materials which are connected to the gas system.
In first line ageing is defined as the performance reduction of a detector due to time and exposure. A detailed description of the topic can be found in [18].
Evaluating the microscopic processes and do precise measurements is complicated. One reason for that is the fact that one cannot imitate the processes for long term operation of the detector. One option is to scale up the exposure to achieve equivalent doses which would be collected over years, but this gives no guarantee for the same performance over time in normal operation.
Having this in mind it is clear that one should draw attention to first minimise the possible ageing by a proper choice of material which is related to the construction of the detector.
Even small pollution during the manufacturing and assembling process can result in a worse performance. Therefore, it is important to stay clean whenever possible e.g. keep everything in a clean room.
Hence, every foreign substance could potentially lead to an adverse effect by radiative interaction or chemical reaction. This can be brought to a minimum by choosing materials with a low outgassing rate. Measurements for this purpose where presented in [19]. As an example some feasible plastic pipe materials are shown in tab. 2.1. A compact presentation which materials should be used for gaseous detectors is given in [20].

Material	Type	Outgassing	Effect in Detector	Global Result
PP	**Poly** **pro** pylene	NO	NO	OK
PA/RILSAN™/NYLON™	**Poly** **a** mide	Water	NO	OK[11]
PEEK Crystalline	**Poly** **e** ther **e** ther **k** etone	NO	NO	OK

Table 2.1: Outgassing properties of some plastic pipes, results taken from [21].

One popular aging effect, especially observed for wire chambers, is called polymerisation. In fact this is a formation of large hydrocarbon chain complexes on the anode[12]. Some pictures are shown in fig. 2.10. It is possible to prevent this by usage of a proper gas mixture. As a rule of thumb all hydrocarbon-based mixtures are not useful to avoid polymerisation. A good alternative is given by carbon dioxide. For a detailed observation it is referred to [22].

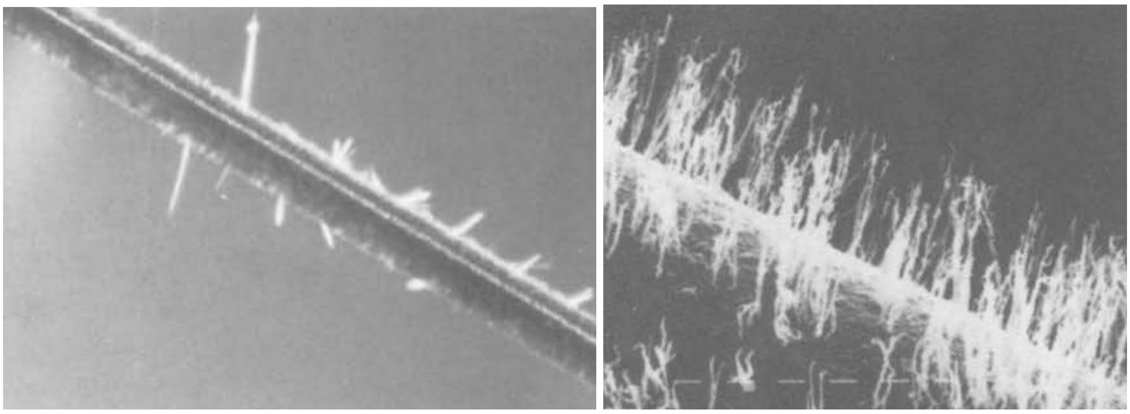

Figure 2.10: Examples for polymerisation on anode wires [23].

[12] For sure has something to do with the comparable low electronegativity difference in C_xH_{2x+2} molecules

CHAPTER 3

Experimental Environment

COMPASS (**CO**mmon **M**uon and **P**roton **A**pparatus for **S**tructure and **S**pectroscopy) [24] is a multipurpose fixed-target[1] experiment which is optimized to measure scattering reactions of high-energy hadron and muon beams.
The spectrometer with a total length of 50 m [24] can be divided into two magnetic stages which results in an improved resolution of momenta and scattering angle. Also the possibility to modify the setup according to the requirements of the physical program comparatively easily, makes COMPASS unique. Using the high-intensity beams[2] from CERN's **SPS** (**S**uper **P**roton **S**ynchrotron) via the M2 beam line, one has a adequate environment to further investigate the subnuclear structure of nucleons and for the spectroscopy of hadrons. One should mention that such high resolutions require a tracking directly along the beam. The main part of the COMPASS tracking system is based on ultra-light trackers in the beam, e.g. the triple-GEM-tracking-detectors, which will be described in more detail in chapter 4.

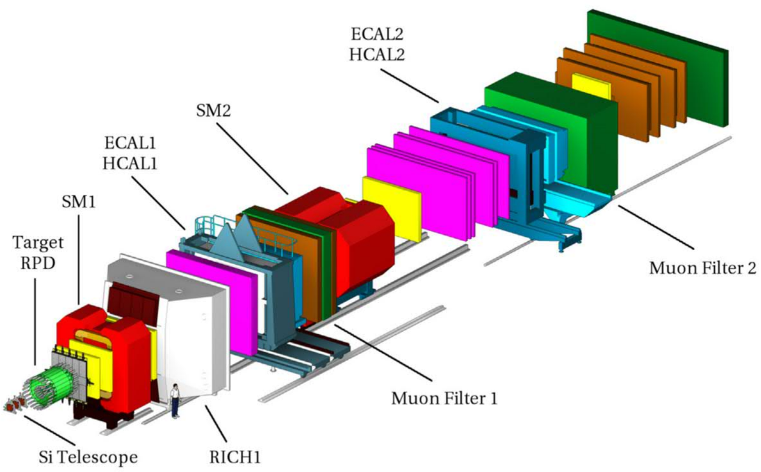

Figure 3.1: Three-dimensional view of the COMPASS setup for measurements with hadron beams [25].

[1] Solid polarized targets: Either ^{6}LiD or NH_3 [24]
[2] M2 can deliver high-energy secondary hadron beams and tertiary muon/electron beams up to 190 GeV/c [24]

3.1 CERN

The COMPASS spectrometer is placed at the north area of CERN. Thus, in this section the CERN and its role in physics is explained.
CERN, the European Organization for Nuclear Research, contains not only the largest and intricate accelerator complex (as shown in fig. 3.2) of the world but is also a platform for researchers to work together at the forefront of science. In 2019 more than 17 600 scientists participated in the research work [26]. With over 7 000 member states [26] CERN shows that there exist no borders because of origin or anything similar in science.

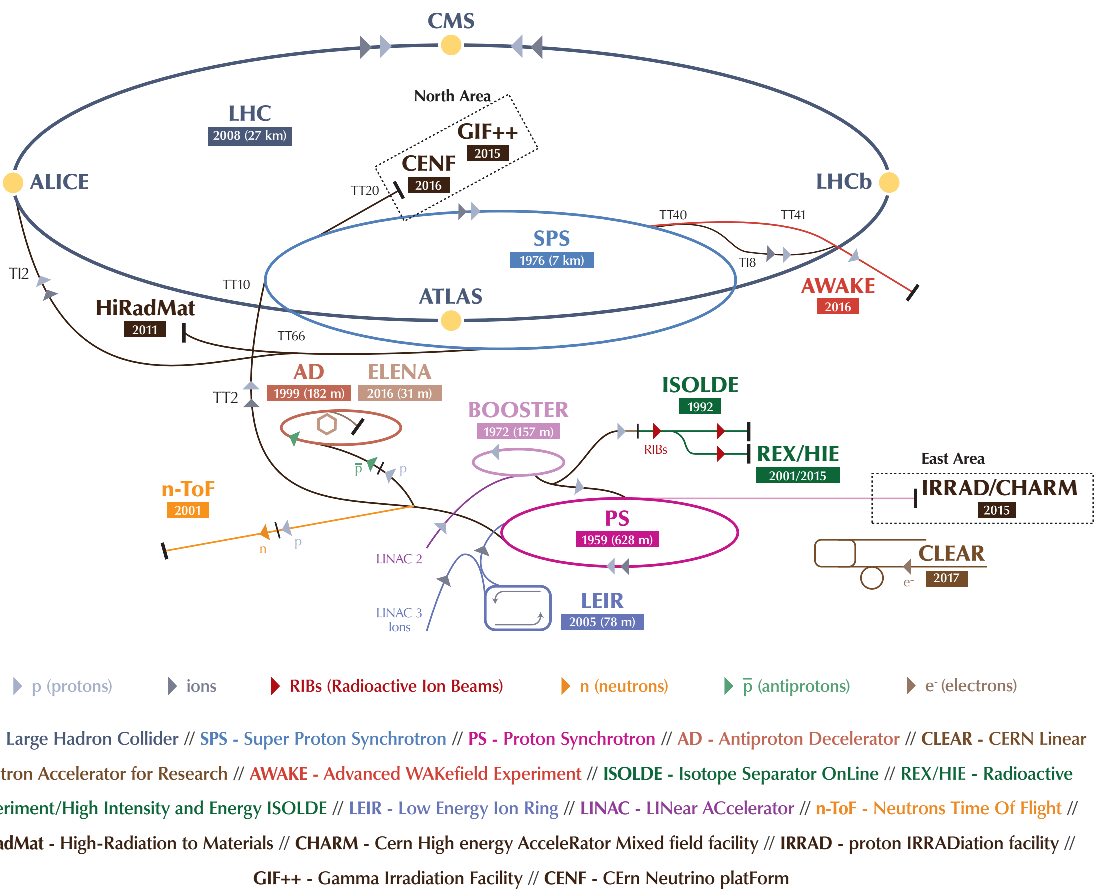

Figure 3.2: CERN accelerator complex [27]. Labels show the acronym, the first year of operation and the lengths for the synchrotron-structures.

The accelerator complex has grown over the time, such that the achievable collision energy has reached at last 6.5+6.5 TeV/c for p^{+}-p^{+} collisions in the **LHC** (**L**arge **H**adron **C**ollider). Several steps are needed in order to reach such high beam energies.
In the beginning the protons are extracted via stripping hydrogen in an electric field. Over the **Linac 2**[3] (**Lin**ear **ac**celerator **2**) and the **PSB** (**P**roton **S**ynchrotron **B**ooster) they were already injected with

[3] This year replaced by Linac 4

an energy of 1.4 GeV/c to the **PS** (**P**roton **S**ynchrotron). With a boost to 25 GeV/c the next stage is the **SPS** (**S**uper **P**roton **S**ynchrotron) which than achieves 450 GeV/c [28]. The SPS directly feeds the LHC which than can reach the maximum energy.

3.2 COMPASS++/AMBER

COMPASS++/Amber is a proposal for new measurements at beam line M2, by using the existing COMPASS environment as a base. Therefore, a whole new spectrometer would be build up by using all the experience and benefits from the past and combine them with state-of-the-art technology to gain an optimal performance for new experiments. Part of this is the upgrade of the tracking system that contains the triple-GEM-tracking detector upgrade.
One should mention three experiments which would be possible with the new spectrometer:

Proton charge-radius measurement using muon-proton elastic scattering
Investigations of proton-radius mismatch corresponding to the lepton-flavour.

Drell-Yan and J/Ψ production experiments using the conventional M2 hadron beam
Here the primary aim is to determine the barely worked out **PDF**s (**p**arton **d**istribution **f**unction) for valence and sea-quarks of the pion.

Measurement of proton-induced antiproton production cross sections for dark matter searches
The experiment will be used to determine the antiproton production cross sections for p^+-p^+ and p^+-^4He scattering. Combined with measurements of LHCb in the TeV range, the measurements in the GeV range should provide a basic data set. Thereby, a much higher accuracy of the predicted natural flux of antiprotons in the galactic cosmic rays would be possible.

A sketch of the COMPASS spectrometer for 2021 is shown in fig. 3.3. As shown, the idea remains the same. Something that cannot be seen in the picture are the upgrades for the different detectors.
For example, many of the GEM detectors will be replaced by the new detector which was designed during this thesis, such that the overall performance of the spectrometer is improved by changing the individual detectors. For more detailed information it is referred to the official proposal [29].

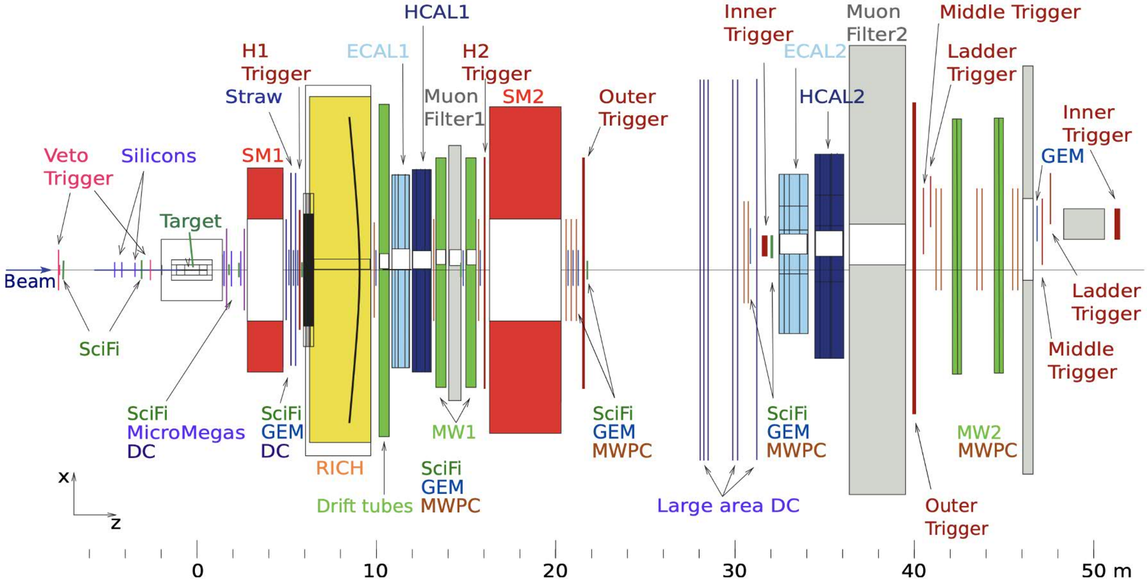

Figure 3.3: Top view of the 2021 COMPASS spectrometer setup [29]. The GEM detectors are distributed over the whole spectrometer and are illustrated in blue.

CHAPTER 4

Triple-GEM-Tracking-Detectors

This chapter will summarise previous Triple-GEM-Tracking-Detectors maintained by COMPASS. It starts with the first large area GEM-based tracking detector, discussed in section 4.1, installed in such a huge experiment. Therefore, a bunch of requirements were made and achieved. These can be found in table 4.1.

Since COMPASS has done some pioneer work for this system and forced great developments, the "detector nomenclature" is as follows: **C**OMPASS **G**EM **#**generation **g**eneration which results in **CG1G** for the first detector.

After this introduction the further developments of the CG1G are explained - beginning with the first investigations to CG2G (section 4.2) and followed by the main subject of this thesis: the upgrade of the triple-GEM-tracking detector to the CG3G discussed in section 4.3.

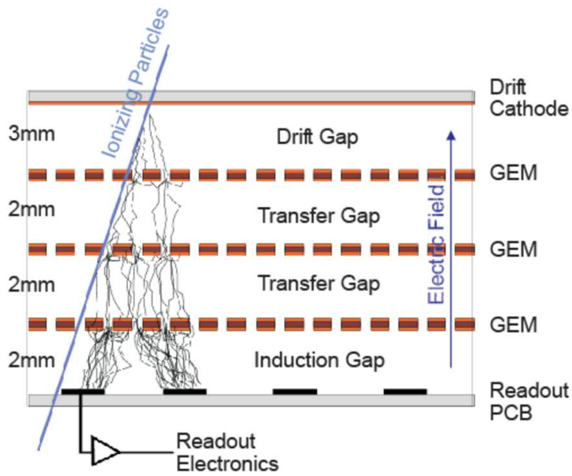

Figure 4.1: Setup for the triple GEM COMPASS detector [2].

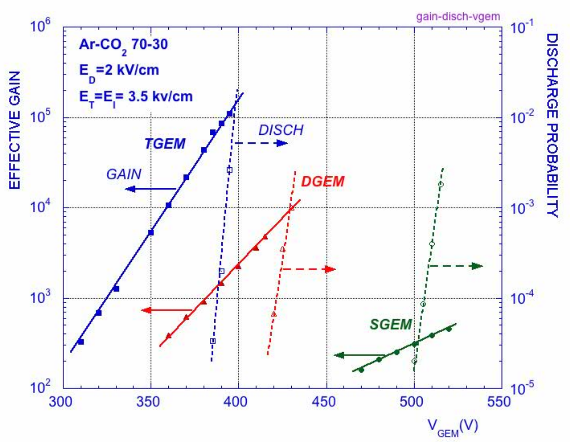

Figure 4.2: Gain and discharge probability for different setups in dependence of effective gain [30].

Before the different iterations will be discussed, the principal of a GEM-based detector will be explained.

Therefore, the triple GEM setup from fig. 4.1 will be discussed. A MIP on average leaves a track with 100 electron−ion pairs/cm in Ar/CO_2 [31]. For a 3 mm drift gap this results in 30 electron−ion pairs between drift cathode and the first GEM stage. The ions drift back to the cathode while the electrons

drift through the first amplification stage. Every time the electron cloud passes a GEM stage the signal will be amplified proportional to the gain. To get the total effective gain one has to multiply the individual effective gains.
This allows higher amplifications at lower individual GEM voltages. Therefore, one can achieve a good discharge prevention with high gains as also shown in fig. 4.2. There one sees e.g. that the discharge probability (right scale) for a single GEM (green) increases at the range of 500 V while this is shifted to approximately 420 V for a double GEM (red) and even further to lower GEM voltages for the triple GEM (blue). On the other hand an increase of the effective gain (left scale) is achieved for a triple GEM compared to a double and single GEM by equivalent discharge probability.
Behind the GEM foil a signal is induced on the readout electrode proportional to the initial energy deposit.
All detectors using a multi layer readout electrode consist of copper with an Kapton™ substrate. Hence, all generations have (at least partly) a strip based readout, that will be discussed in the following.

Spatial resolution	< 100 µm
Time resolution	∼ 10 ns
Rate capability	> 10^4 part. mm^{-2} s^{-1}
Small material budget	0.4 $\%X_0$ [1]
Large active area	31 cm x 31 cm
Low aging	up to 7 mC mm^{-2}
Discharge prevention	prohibit channel loss

Table 4.1: Requirements for one CG1G [32].

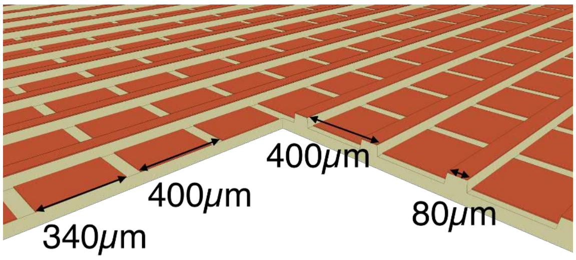

Figure 4.3: Schematic view of the strip readout with 5 µm copper(red) strips and 50 µm Kapton™(beige).

Basically two sets of orthogonal 5 µm thin copper strips were used which are separated and supported by 50 µm thick Kapton™ layers. In the crosscut shown in fig. 4.3 one finds the design values for pitch and strip size. The parameters are chosen such that one gets a charge sharing adjusted readout.
That means the upper strips collect the same amount of charge as the lower ones. This can be measured by the cluster charge as depicted in fig. 4.4. There the results for a CG1G detector are shown.
Therefore, the ratio of both cluster charges can be build. Fig. 4.5 presents the result for the used configuration of 90 µm upper strips and 340 µm lower strips. In a graphical representation like this a delta peak at one would correspond to a perfect adjustment of the ratio. Because then the collected charge would be exact the same for each cluster size.
As predicted for charge sharing adjusted readout a peak around one occurs in the data which is smeared out due to fluctuations of the cluster charge.
With a charge sharing adjustment of ∼ 1 : 1 later on one can achieve better resolutions due to similar signals independent of the strip coordinate.

[1] Nominal thickness of 15 mm for one detector with two projections

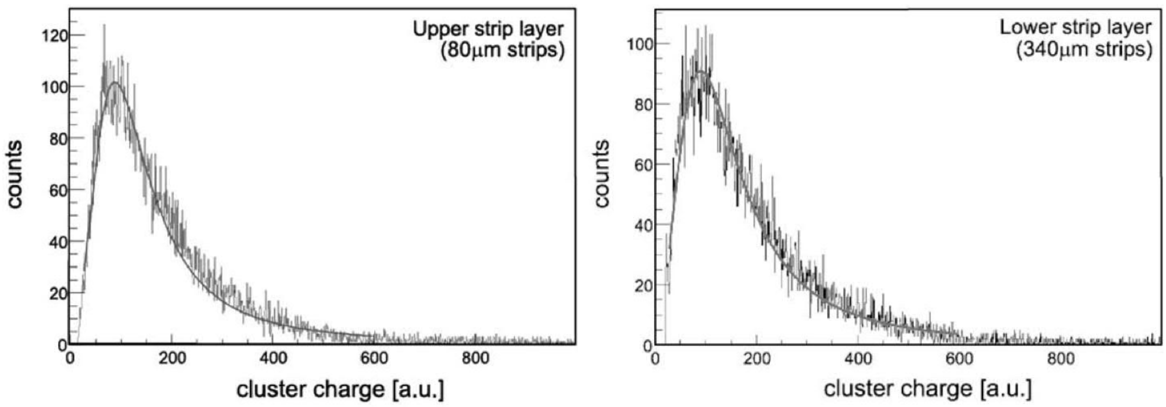

Figure 4.4: Cluster charge in a.u. for the different strip sizes. Left for 80 µm and right for 340 µm [33].

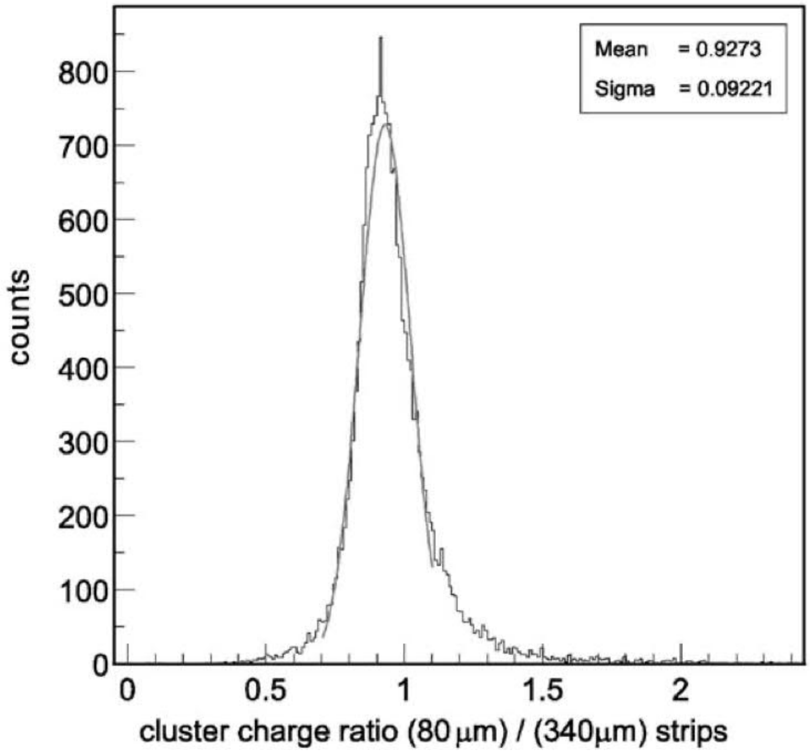

Figure 4.5: Cluster charge ratio for 80 µm/340 µm copper strips separated by 50 µm Kapton™ [33].

4.1 CG1G

The first generation is in operation since 2001. Meanwhile a total set of 22 large-size triple-GEM detectors is installed along the COMPASS spectrometer. They were an essential part of the tracking system, cause they are placed allover the spectrometer. Over years the performance was stable with an average single plane efficiency of > 97 % and a spatial resolution around 70 µm for all detectors [29]. Early ageing studies found that there should be no restriction for at least seven years in operation which corresponds to a total exceeding of collected charge of 7 mC mm^{-2} [34]. A good presentation of the performance is given by [35]. For more details, e.g. containing construction, one should refer to [33]. Further the design should be outlined. In fig. 4.6 one can see the raw structure consisting of the corpus with the GEMs and the support plates as maintaining element.

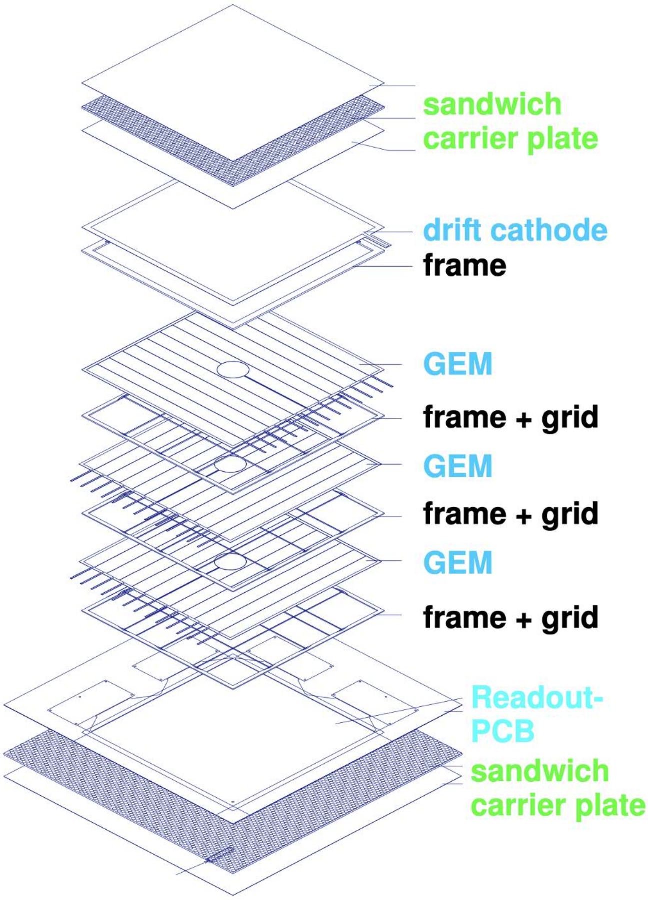

Figure 4.6: Exploded view of CG1G [33].

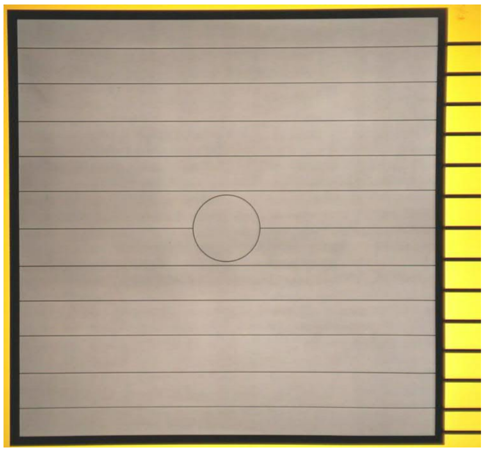

Figure 4.7: GEM segmentation of CG1G [33].

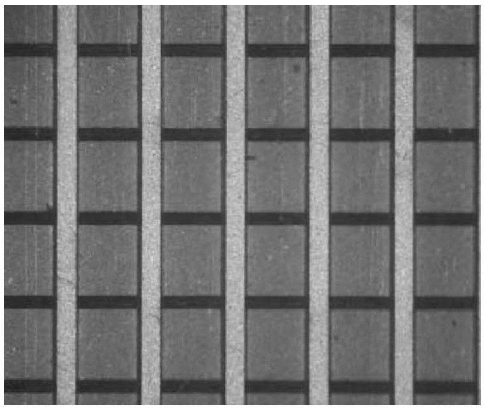

Figure 4.8: Readout of CG1G [33].

All components in depicted order are glued together as the frames are also separating the gas volume from the outside. As one can see each GEM will be glued on a grid frame, shown in fig. 4.9, to guarantee the uniform distance. This should avoid any gain fluctuations caused by sagging of foils. A bad side-effect is that the detector performance is affected as can be seen from the efficiency. In fig. 4.10 this effect is represented for the efficiency in the u-v-plane of a CG1G detector. The structure of the grid is depicted by lower efficiencies.

The readout and drift foil were glued on the corresponding sandwich carrier plates. Here a composite out of fiber glass and honeycombs was used to achieve high stiffness with very low material.
The gas pipes were glued into the large support plate where also the front-end electronics are mounted on.
The GEM foil design is for long operation propose such that even with a dead sector one still can run the detector. Therefore, it was 12 fold top sectored with an additional centre sector which could be turned of for the last GEM[2] as shown in fig 4.7. The readout itself is based on 2D strips perpendicular to each other. Hence, COMPASS operates all detectors in sets of two and rotate them by 45° to each other. Thereby, one gets the X/Y- as well as the UV-coordinates from a traversing MIP. Here the typical design parameters were used like discussed above and a close up of the readout plane can be seen in fig. 4.8.

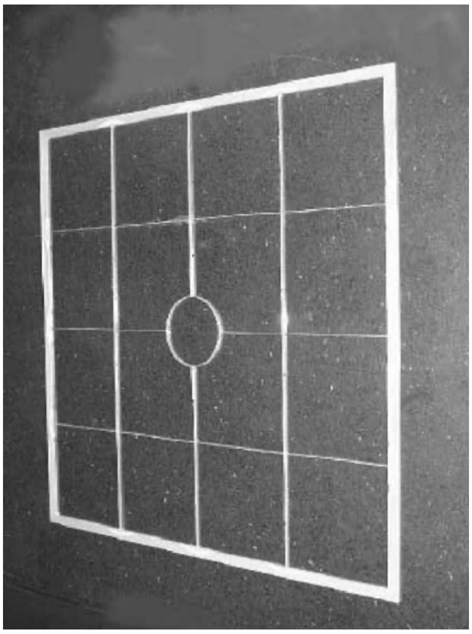

Figure 4.9: Spacer grids of CG1G [33].
.

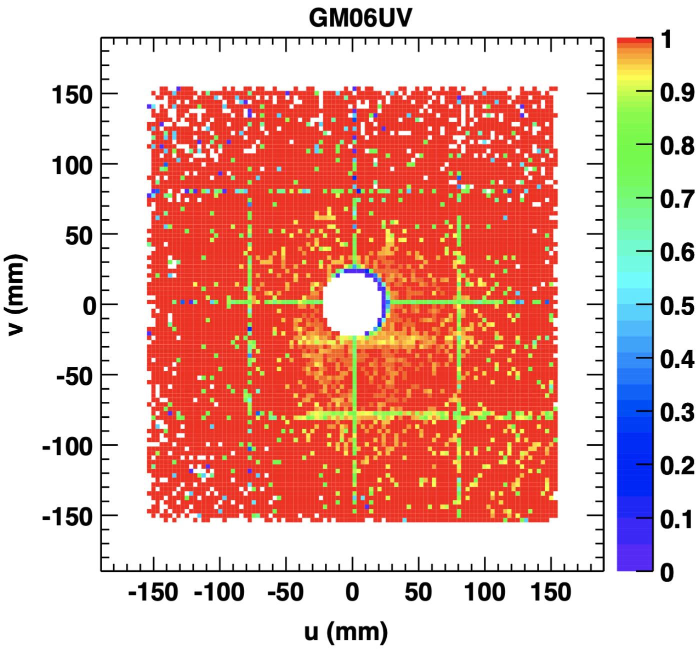

Figure 4.10: 2D efficiency map for one CG1G detector with the beampipe in the middle [35].

4.2 CG2G

After proper prototyping a new triple-GEM-tracking detector was setup and in spring 2008 five CG2G were installed in the COMPASS spectrometer [36]. With the high-intensity hadron beam up to 2×10^7 part. s^{-1} the occupancy with continues strip readout is too high to operate the central region of CG1G. Therefore, the CG2G detector was designed for a extraordinary high rate capability as well as outstanding detection efficiency. In addition, a low material budget of a GEM-based detector yields an improvement by lowering hadronic interactions with detector material in comparison to **SciFi**s (**Sci**ntillating **Fi**ber tracker)[3] as presented in [37].
In fig. 4.11 one can see that the design is derived from the CG1G. Like previously the gas inlets are

[2] Intervention to protect the readout from the high rates caused by the beam
[3] Used to measure the beam and nearby since the good spatial (130 µm) and time (0.4 ns) resolution [24]

through the large support plate and spacer grids where used. Thereby, the grid was reduced, such that the active area is not affected. The low material budget solution for the carrier plates was taken over. Fig. 4.12 shows the GEM foil with an active area of 100 mm x 100 mm which is sectored five times on the top side, including the central area. In the outer region large holes for gas exchange were made. There also no copper is coated and no amplification takes place. Here a further reduction of the material budget was achieved by additional copper etching without performance losses [38]. With 1-2 µm instead of 5 µm copper layers the material budget for one detector could be reduced by approximately 30 % [36].

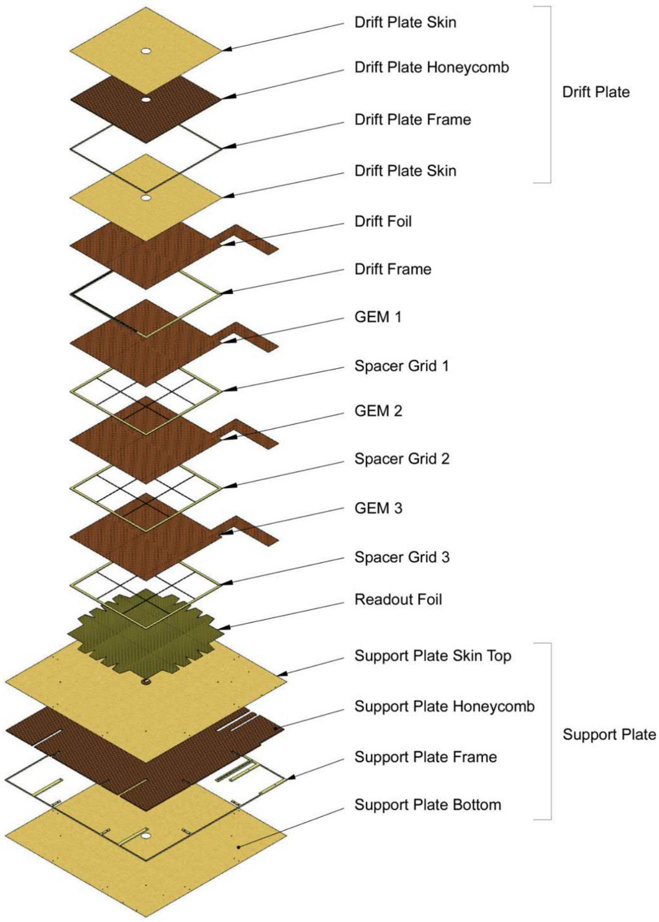

Figure 4.11: Exploded view of CG2G [39].

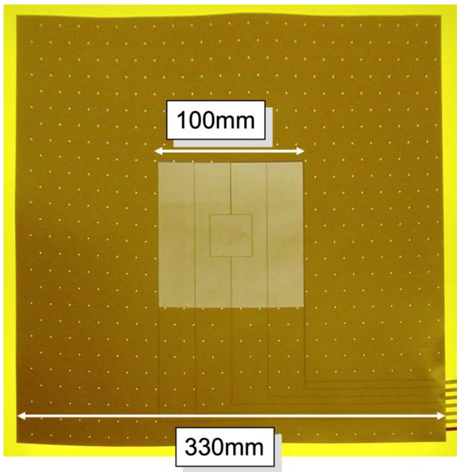

Figure 4.12: GEM segmentation of CG2G [39].

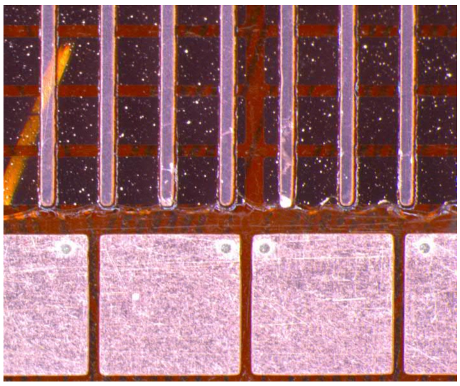

Figure 4.13: Readout of CG2G [39].

The readout is based on 32 x 32 pixels in the centre with 1 mm pitch and size of 0.95 mm x 0.95 mm. With ambient cut 1 024 2D strips the active area is expanded to 100 mm x 100 mm. A close up of the crossover region can be seen in fig. 4.13. With this the CG2G detector achieves a spatial resolution of 90 µm with a time resolution of 10 ns for high rates $\sim 10^5\,\mathrm{mm}^{-2}\,\mathrm{s}^{-1}$ [2].

4.3 CG3G

The CG3G detector is on the one hand proposed as a replacement for the old CG1G[4] which are starting to lack in efficiency and on the other hand a transition state to go to large area PixelGEM detectors with self-triggering readout.
Therefore, the detector should combine all advantages which have been worked out in the previous generations. The timeline foresees the prototype detector until 2020 and 5-10 more detectors until 2021/2022 for replacement.
Thereby, also new front end electronics should be developed for 2021. Since the CG3G will be discussed further in detail, it will be just scanned in comparison to CG1G and CG2G. Having a look at the exploded view shown in fig. 4.14 it is apparent that this design equals the previous designs. One difference can be seen in the spacer frames where the grids got removed. The gas inlets are placed on the upper support plate, since this caused some troubles for the CG2G.

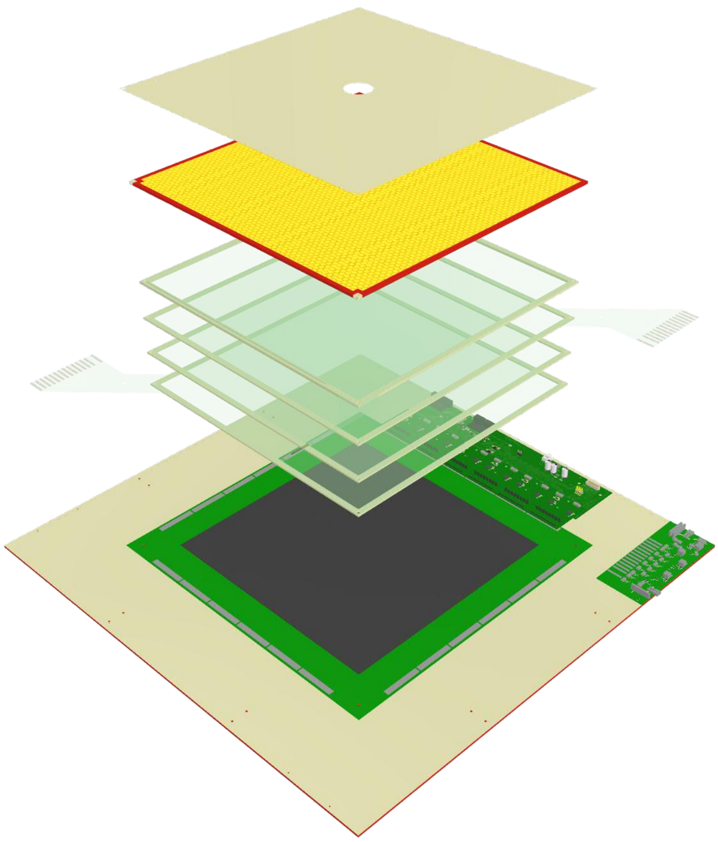

Figure 4.14: Exploded view of CG3G.

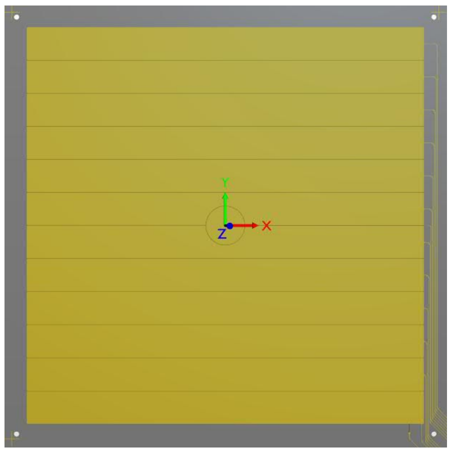

Figure 4.15: GEM segmentation of CG3G.

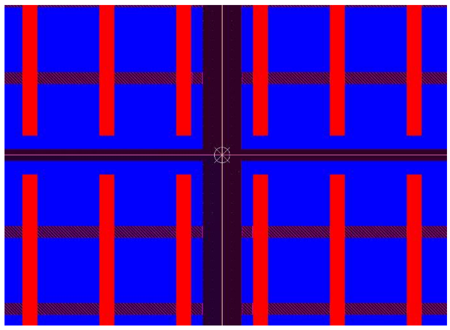

Figure 4.16: Readout of CG3G.

The GEM foils are conceptional equal to them from CG1G as shown in fig. 4.15. That means the foil is sectored on one side into 13 areas within the centre. One difference which can be seen is the tracing of the tracks. For the CG3G this is concentrated to one corner considering the spacing of the outer

[4] From the years of 2015 to 2017 a efficiency drop down to 60 % for some detectors has been observed

electronics to reduce any undesirable influence. For several aspects, e.g. exchange outdated electronic components, the whole readout chain was redesigned. A close up of the centre from the readout plane is depicted in fig. 4.16. It contains 4 x 768 strips to have a 2D readout which is cut in the middle. This lowers the occupancy and leaves space for upgrades regarding an additional pixel readout in the centre. Due to the additional copper etching the material budget for the CG3G is also reduced like for CG2G. Thus, it should be a proper replacement.
Nevertheless the CG3G offers the possibility to exchange the APV-S1 (discussed in detail in section 5.5.1) chip for the VMM chip with minor changes. This would integrate self-triggered readout on the front-end which directly grants a higher rate capability - a step that is needed to be competitive in high energy physics.
Moreover, an advantage is to test the different chips under the same conditions with the identical detector.

CHAPTER 5

New Large-Area-Triple-GEM-Tracking-Detectors

This chapter describes the main part of the thesis which is the complete design and presentation of the new CG3G detector.
Therefore, each component will be shown and characterised. Beginning with a detailed description of the mechanical design outlined in section 5.1. Followed by the illustration and discussion of the different foils used for the detector (section 5.2). The designed tools which are required to manufacture the prototype are explained in section 5.3. Finally, the last sections cover the used high voltage supply card (section 5.4) and the redesigned readout chain (section 5.5).

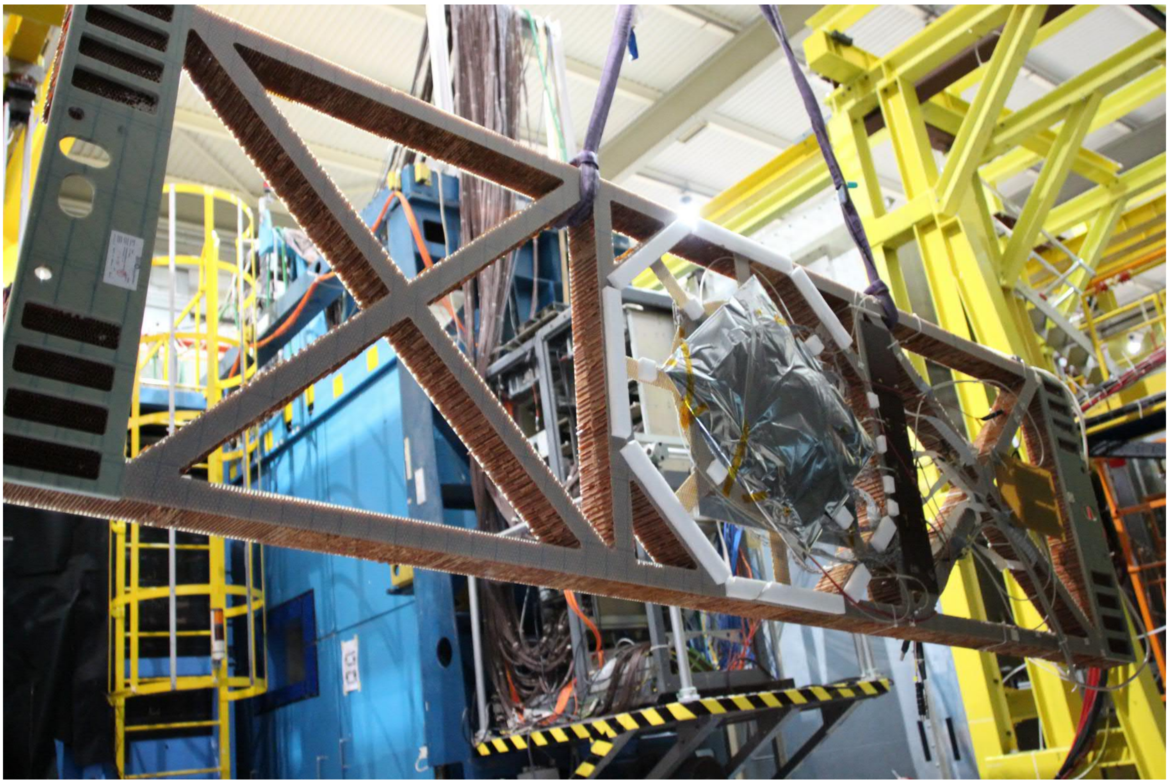

Figure 5.1: Picture of a existing CG2G station hanging on a COMPASS crane.

In order to keep all files and useful information in one place, the cloud system "sciebo" is used. It is a non-commercial file-hosting system which is supported by the state of North Rhine-Westphalia, suited for long-term use (as long as the support is valid) and easily accessible. In order to prevent misuse, the files are protected with a password (CG3G4all). The over all design has to be backward compatible for different reasons. One, e.g., would be the reuse of the carrier structures. One of those can be seen in fig. 5.1.
There two CG2G detectors sitting back to back with 45° tilt in the centre covered by aluminised mylar[1].

5.1 Mechanical Design

The most time of the master thesis was spend in the mechanical design, when expecting all iterations and the time for consultation with the workshop. This is important because each mistake increases the time and costs of the prototyping process. Therefore, each step should be planned in advance to keep the production as fluent as possible.
The dimensions of the designed detector were taken from previous detector generations. Reasons for this are the reusability of consisting mounting structures that are needed to install the detector in the spectrometer, the required backward compatibility to be able to exchange the CG1G and furthermore the stable performance of the design. On the electronics side the compatibility to the existing **DAQ** (**D**ata **A**c**Q**uisition) system of the experiment has to be ensured.
Based on this, all parts were redrawn from scratch with AUTODESK©Inventor and are not for commercial use. All CAD drawings can be found on sciebo[2].

5.1.1 Support Plates

The support plates carry the detector and prevent a up blowing due to the inner pressure. To achieve high stiffness with a minimal amount of material a composite out of glass fibre strength plates with honeycomb core were used. To keep the material as low as possible is necessary to minimize inefficiency as the detector stands in the beam and also with the complete volume in front **MWPC**s (**M**ulti **W**ire **P**roportional **C**amber), as can be seen in fig. A.5. A example for such a composite with a thick Nomex©core would be the carrier structure depicted in fig. 5.1. Here one can also see the huge advantage of composites: One can gain sufficient more stiffness with increasing the honeycomb high by having comparable small amount of additional material, since the major factor comes in from the closing laminate layers. Since this concept has shown to be reliable from CG1G and CG2G it is taken over for the new design.
Taking a closer look on fig. 4.11 one sees that the support plates also contain a frame and bridges in the honeycomb layer. There especially the walkways to prop holes yield to additional material.
Therefore, in the current design this is exchanged by potting[3]. The plates were ordered from Piekenbrink Composite.

[1] Serves as protection against bird droppings
[2] Link for the CAD drawings: `https://uni-bonn.sciebo.de/s/5kfsDZjFOWFYGRS` pw:5
[3] Specific filling of cells which can be done after the production process of the panels to increase local durability

Small Plate

The small plate contains the gas inlet/outlet and the honeycombs are covert with potting around the sides. With the drift foil glued on it it covers the topside of the detector. The technical drawing sent to the manufacturer can be seen in fig. 5.4. There the potting regions are marked in red.
Furthermore, detailed views are implemented with their origin and scaling, e.g. D shows the circled region in a 5:1 scale. That way one can show all characteristics within one pdf file.
In the technical drawing one sees that the honeycomb core should have a thickness of 3 mm with 100 µm skins on each side. In the centre honeycomb and skins are removed to get as minimal material as possible in the direct beam region.
As the small plate is the in- and output of the detector gas system two blocks consisting of PEEK with milling are implemented for this usage. PEEK is used for his good outgassing and glueing properties. The tubes from the outer system will be glued into the milling. The glue surface is enlarged by special cutting of the tube.
To test the concept a **GSD** (**G**as **S**ystem **D**ummy) was designed, consisting of two parts as shown in fig. 5.2. The parameters from the left part correspond to the design of the small plate. The right one is used to simulate the narrowest passage of the gas system.
Fig. 5.3 shows a fully glued GSD. Here one can also see how the tube was modified, such that the resulting flap reinforces the connection.
This dummy was tested up to 5 bar without leaking or cracking. By installing it into a gas system of one of the setups in the lab no harms were detected e.g. reduction of flux.

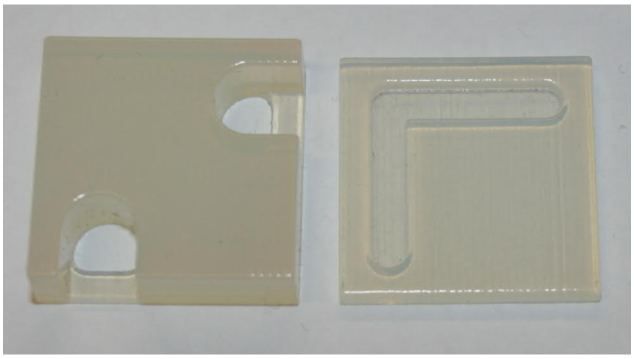

Figure 5.2: Gas system dummy components.

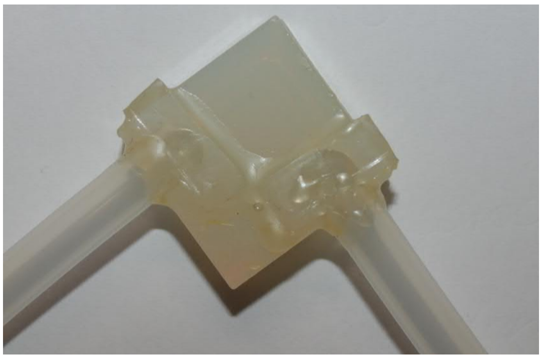

Figure 5.3: Glued gas system dummy.

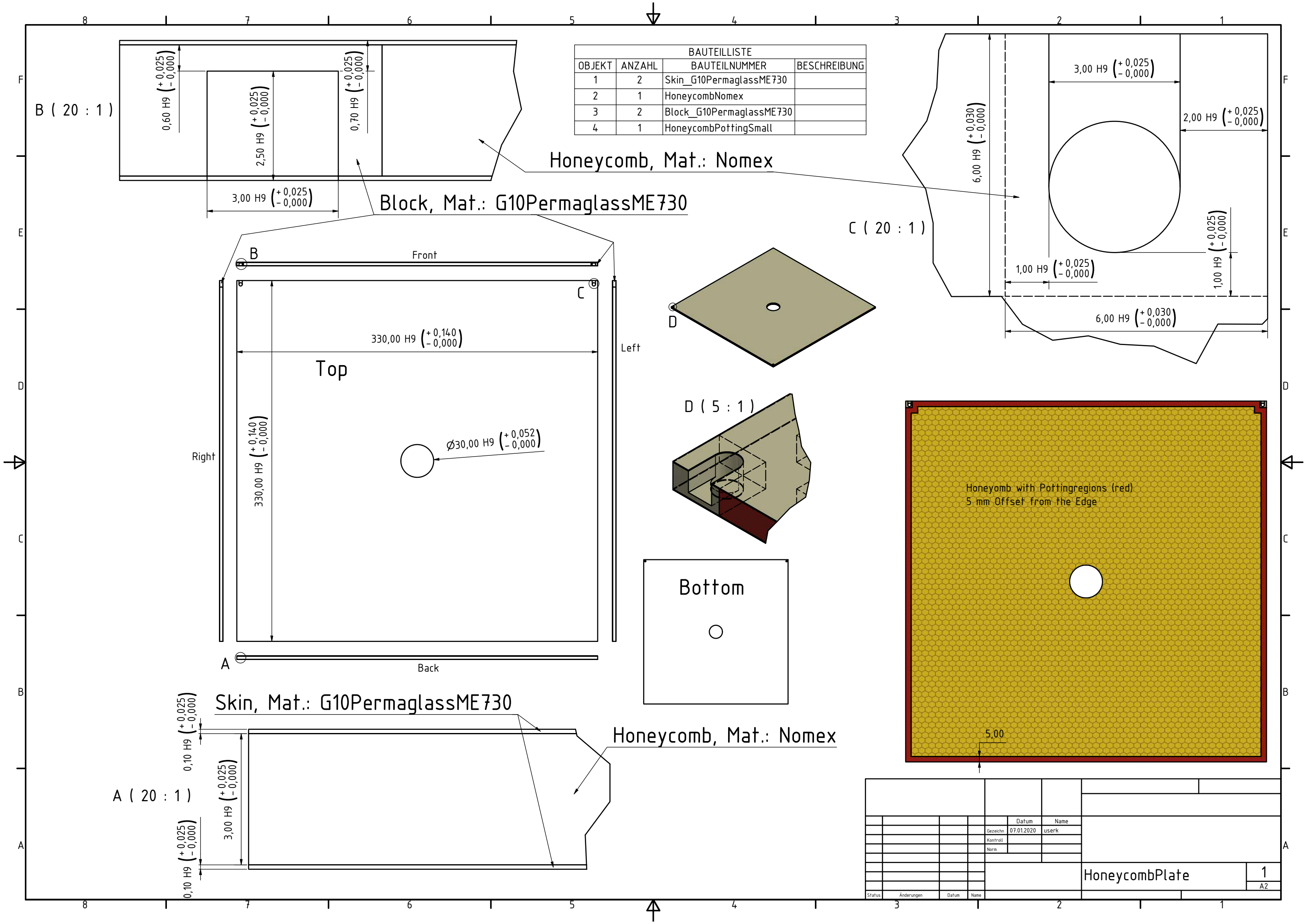

Figure 5.4: Technical drawing of the small support plate which was sent to Piekenbrink Composite. All size indications given in mm. Deviations from the technical drawing: Tolerances set to ±0.02 mm, an other skin material A.9 and PEEK for the gas inlets ("Block" in the drawing).

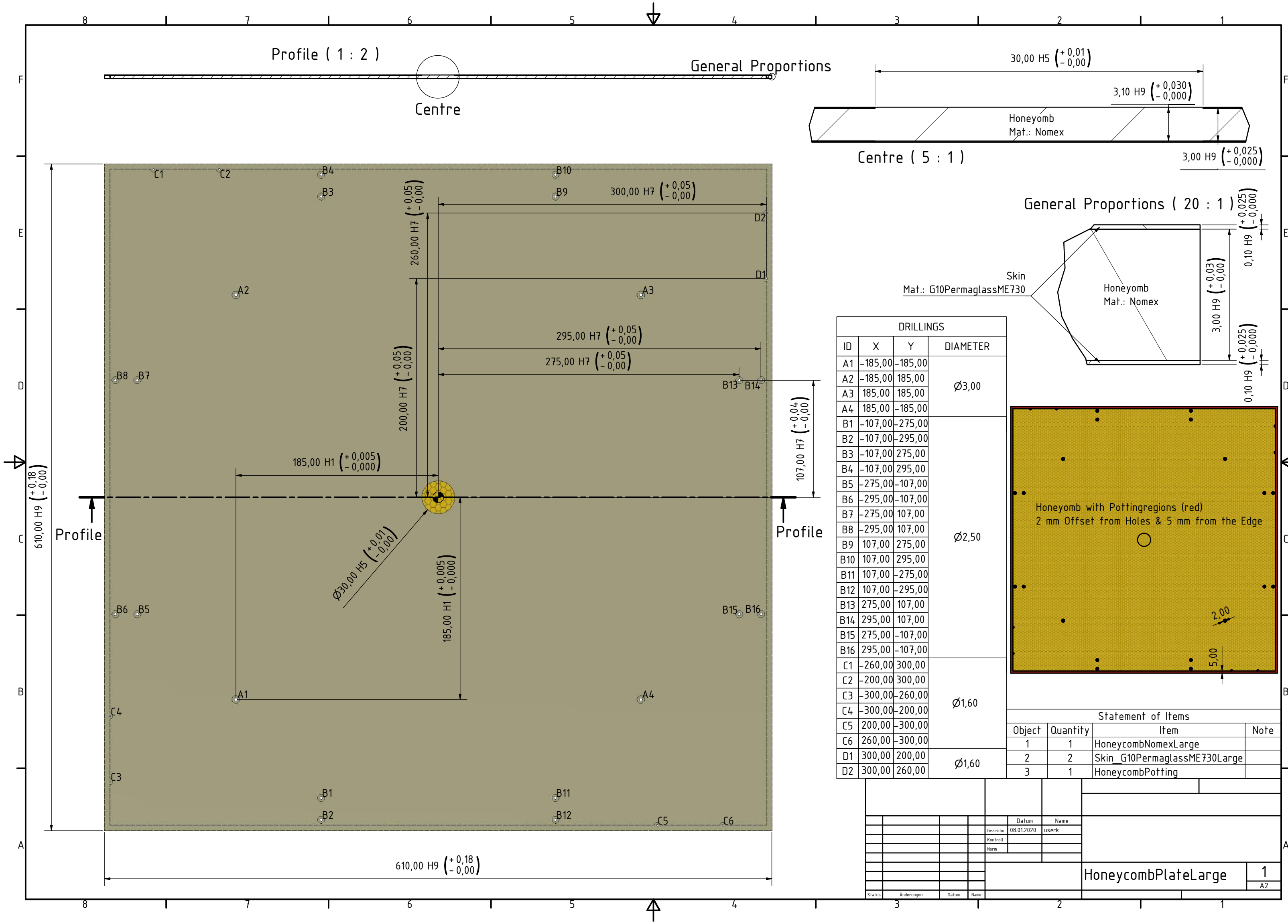

Figure 5.5: Technical drawing of the large support plate which was sent to Piekenbrink Composite. All size indications given in mm. Deviations from the technical drawing: Tolerances set to ±0.02 mm and an other skin material A.9.

Large Plate

The large plate is the base of the detector. All PCBs are mounted with plastic screws as they should stay exchangeable. For this reason the plate not only consists of the honeycomb core and the skins but also has some potting to stabilise the holes.
As can be seen in fig. 5.5 one can distinguish between three types concerning the diameter: The 1.6 mm are for the HV-board mounting, 2.5 mm for supply card mounting and the 3 mm for the alignment during manufacturing. The alignment holes are also used to mount the detector at the carrier structure for installation in the COMPASS spectrometer as seen in fig. 5.1.

Alternatives for Support Plates

In the beginning of the project several materials have been explored to find alternatives for the previously used composite plates. Since they are quite expensive and it is not easy to find manufactures which produce the small amount of composite plates at all, it might be also sufficient to use material which could be taken directly from the supplier and process it in the own workshop.
After some samples from different suppliers it was clear that raw materials obviously cannot keep up with a composite.
Nevertheless, some interesting stuff could be gained. Tab. 5.1 compares some possible materials/composites which could be used. Like said all raw materials need to be modified. Mostly they need to be smoothed down because of the thickness. After that obviously the amount of radiation length is even lower but then also the stiffness gets to low.
For the raw materials the PP-Honeycomb sticks out. Actually this is kind of composite with a 10 mm PP honeycomb core between two 1 mm PP honeycomb plates. Since the most material comes from the skins, here one could mill away the most amount without decreasing the stiffness to much. One problem remains as one can not go below the core height. This may cause bigger problems by installation in the experiment since there the detectors have only small space.
An interesting thing would be to test the composite with Sigraflex TH mentioned in table 5.1. But without the tools to manufacture this by self it is quite to expensive to be tested.

Origin	Part	Material	Thickness in µm	Fraction	Density in $g\,cm^{-3}$	Rad Length in $g\,cm^{-2}$	x/X0 in ‰	Total in ‰	Cost in €	Modifications required	Pro	Contra
Previous	Honeycomb skin	G10	200	1	1,700	33	1,03					
	Glue	Epoxy resin	62	1	2,000	49,25	0,25					
		NOMEX	3000	0,018	1,380	33	0,23					
	Glue	Epoxy resin	62	1	2,000	49,25	0,25					
	Honeycomb skin	G10	200	1	1,700	33	1,03	2,79	-	Not expected	Approved	Not available
SCEI Aeronautique Defense Spatial	Honeycomb skin	7781 e-glass	200	1	1,210	31,52	0,77					
	Glue	Epoxy resin	62	1	2,000	49,25	0,25					
		NOMEX	3000	0,018	1,380	33	0,23					
	Glue	Epoxy resin	62	1	2,000	49,25	0,25					
	Honeycomb skin	7781 e-glass	200	1	1,210	31,52	0,77	2,26	3236,00	Not expected	Approved	Very Expensive
Piekenbrink Composite	Comparable with SCEI							2,26	1928,50	Not expected	Approved	Expensive
	Sigraflex TH	C/C	150	1	0,7	42,7	0,25					
	Glue	Epoxy resin	62	1	2,000	49,25	0,25					
		NOMEX	3000	0,018	1,380	33	0,23					
	Glue	Epoxy resin	62	1	2,000	49,25	0,25					
	Sigraflex TH	C/C	150	1	0,7	42,7	0,25	1,22	-	Not expected	Low x/X0	R&D needed
	Foamlite P	PP	6000	1	0,65	44,085	8,85	8,85	-	Yes	Low density	Thick/fragile
	Slentite	Polyurethan-Aerogel	10000	1	0,135	44,64	3,02	3,02	-	Yes	Low density	Thick
	Sigratherm LN	Carbon(C/C)	15000	1	0,05	42,7	1,76	1,76	-	Yes	Low density	Thick
	Sigraflex TH	C/C	150	1	0,7	42,7	0,25	0,25	-	Yes	Low density	Foil
	Nidaplast 8	PP	5000	1	0,065	44,085	0,74	0,74	-	Yes	Low density	Thick/abrasion
	PP-Honeyc.	PP	12000	1	0,25	44,085	6,81	6,81	125,88	Yes	Cheap	Thick
	Sigrabond Performance	C/C	2200	1	1,5	42,7	7,73	7,73	575,00	Yes	Thin	High x/X0

Table 5.1: Comparison of materials/composites sufficient for support plates. Prices given for one set (one large and one small plate) excluding one time costs at the start of production. Radiations lengths calculated with values taken from [31].

5.1.2 Spacer Frames

In the used design the frames have several functions and requirements. As they are in direct contact to the gas volume one needs to avoid outgasing in order to minimise ageing effects. Hence, they are also the barrier to the outside they should suppress any diffusion of unlike materials through the detector. During the mounting and operation a sufficient amount of tension is applied to the material, such that it has also to be stiff. Because the whole system is glued together it has to be bondable. Since all requirements were admissible fulfilled by Vetronit EGS 103 as shown in fig. A.7 and it is already used for the ALICE GEM upgrade [40], it becomes the chosen one.
The raw material was delivered in 384 mm x 384 mm plates by vonRoll©. With additional polishing by the supplier a flatness of (3.00 ± 0.06) mm and (2.00 ± 0.04) mm was ensured.
The frames then were drilled out of the plates by our workshop in the HISKP. To get a sufficient precision and avoid demolishing the material, more expensive milling heads for higher rotations per minute (rpm) and cutting fluids are required. The data sheet for this can be found in appendix A.2.
One important thing would be that it is without silicone.
Hence, this could outgas later on an cause aging effects.
Furthermore, to lower the material costs, all drawings were attuned such that all contours can be milled with just one head size.

Figure 5.6: Frame cleaning with ultrasonic bath.

Figure 5.7: Frame stack construction.

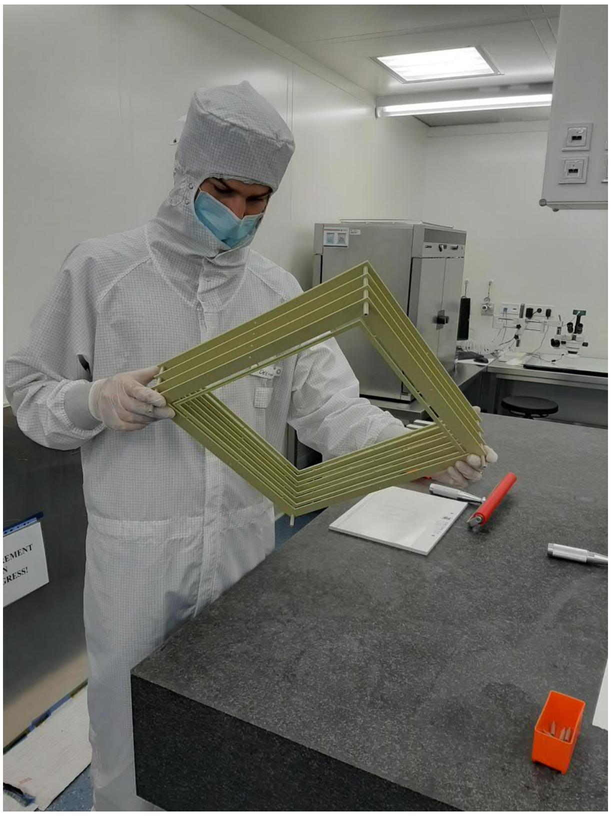

Figure 5.8: Stack ready for drying cabinet.

After fabrication the cleaning process starts. As implied in fig. 5.6 all frames undergo a three stage cleaning with an ultrasonic bath. The first two with a 50:50 mixture of isopropanol and deionised water to remove all major pollution. The last passage is with only deionised water to get rid of smaller impurities and leftovers. After the baths they get dried with gloves and a nitrogen gun, which is the process shown in fig. 5.6.
Here we are already in a passage towards the clean room such that normal shoes were only allowed with overcoat or even clean slippers should be used. In the clean room a set of frames which corresponds to one detector is stacked with spacers like depicted in fig. 5.7. After a rough inspection by eye if all components from the drawings were done, the stack will be stored in the dry cabinet till assembly.
In fig. 5.8 one can see myself checking if the gas system through the frames should work (due to asymmetry of drift and readout frame this is not obvious). The frames will be discussed starting with the most rudimentary.

GEM Frame

A triple-GEM detector needs two GEM frames which will be glued between the GEM foils and serves as separation of the gas volume from the outside. A frame preserves the stretching of the foils to avoid sagging. The thickness of the frames also defines the transfer gap which has a design value of 2 mm. The frame itself is just 7 mm wide but surrounded by the alignment and holding framework. A drawing can be seen in fig. 5.9 with the alignment holes of 3.1 mm diameter in the corners.
The outer frame will be removed after construction by cutting the thinner bridges which can be seen in fig. 5.10.
The hole in the inner frame is for the gas system, hence the gas-outlet is guided through the hole frame stack. To avoid glue flowing into GEM holes, rims were foreseen on the corner which act as a reservoir for overflowing glue. Fig. 5.13 shows a microscope picture from a readout frame were the rims are visible.

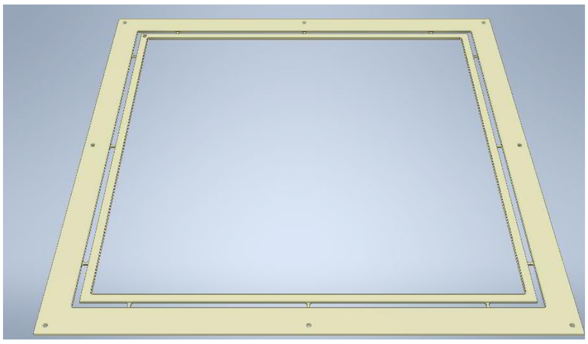

Figure 5.9: View of 2 mm thick GEM frame.

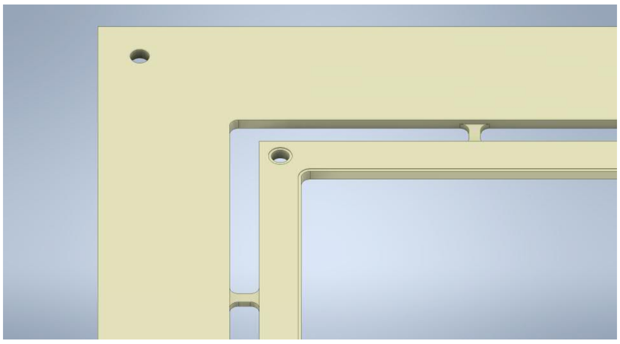

Figure 5.10: Zoom of GEM frame.

Readout Frame

The readout frame is placed between the last GEM foil and the readout plane. The structure is similar on the GEM frame. In principle there is an additional drilling along two sides for the gas system as can be seen in fig. 5.11. Through this corridor the gas should be guided to the corner and flow the whole stack back out of the detector. The two corridors are connected to the gas volume via four slits each where one is depicted as example in fig. 5.12.
Here one can also see that the glueing rims are not only used to protect the GEM foils but also to avoid any blocking caused by glue inside the gas system. This is important because otherwise the detector could blow up and become irreparable destructed.

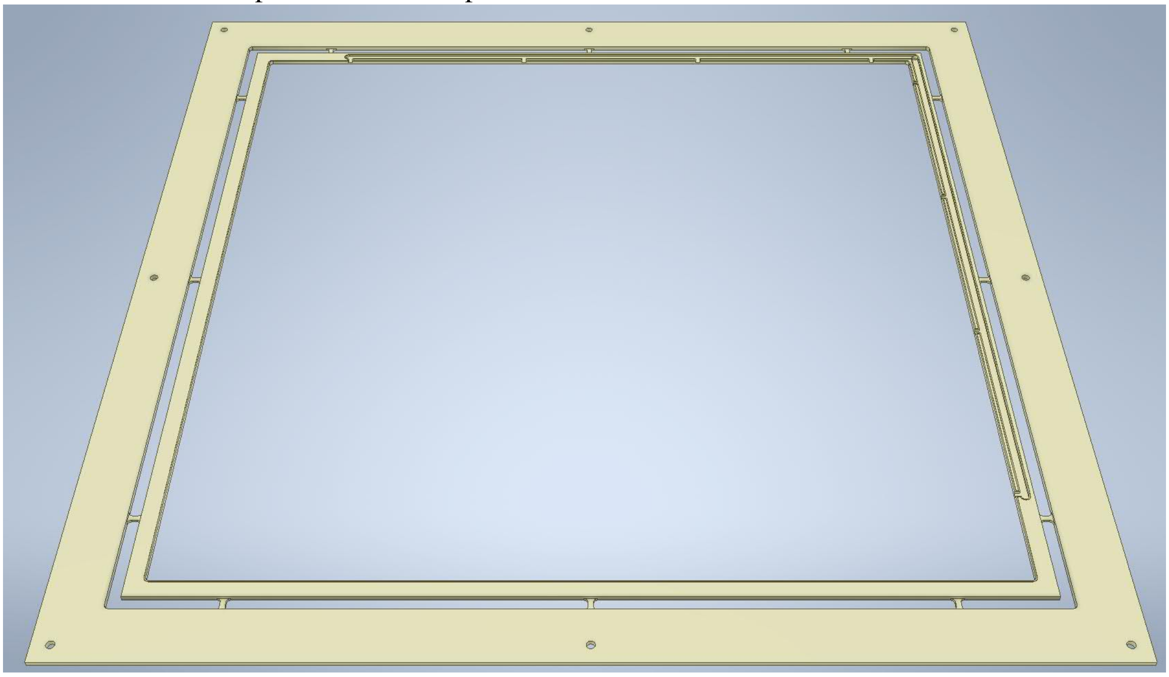

Figure 5.11: View of 2 mm thick readout frame.

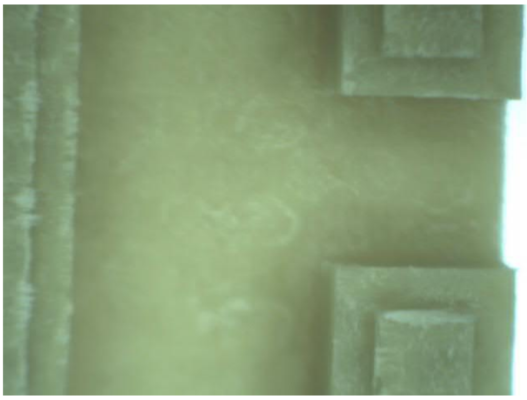

Figure 5.12: Slit for gas back flow.

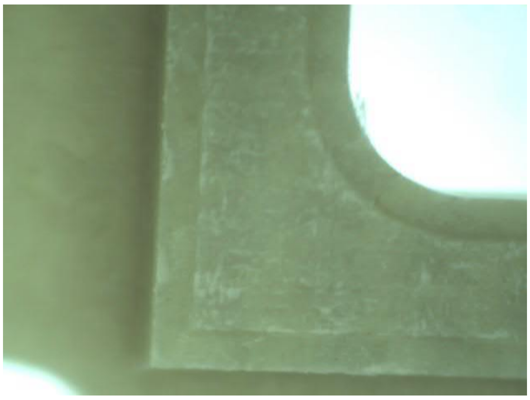

Figure 5.13: Glueing rims of readout frame.

Drift Frame

At last the drift frame which is the only one with a thickness of 3 mm will be discussed. This is defined by the size of the drift gap in the setup.
Like the readout frame it contains two corridors with each four slits for the gas system which can be seen in fig. 5.14 and fig. 5.15. Since here the purpose is an equal distribution of the incoming gas above the stack, the slits are modified in size.

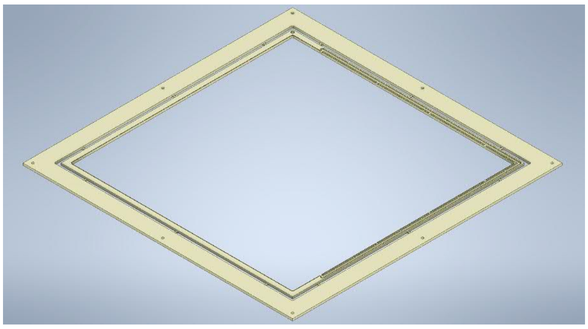

Figure 5.14: View of 3 mm thick drift frame.

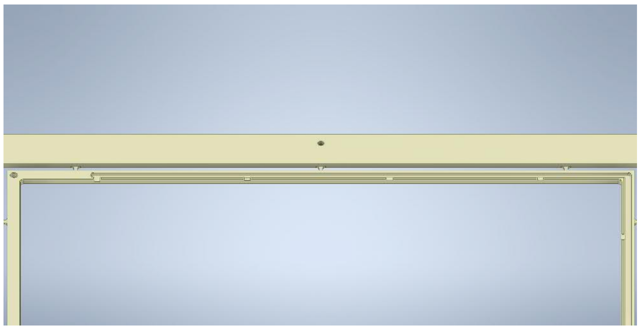

Figure 5.15: Zoom of drift frame.

The different profile surface sizes were taken from the CG2G design because there this advantage was already implemented to ensure a equal gas distribution in the detector. Here, for example, the length and high is adjusted such that all slits have the same width with varying depth. Therefore, one does not need additional milling heads for the different profile surface sizes. How this looks like can be seen in fig. 5.16.
Like for the readout frame here the glueing rims also were used. At the drift frame one can see the beginning and the end of the gas system inside the detector. Looking at fig. 5.15 the gas flows in the right corner and will be distributed by the corridors and slits above the first GEM. After passing to the foils it is guided through the readout frame in the left corner and from there on back over the GEM frames to the drift frame.
As mentioned the hole for the gas backflow can be seen on the left side of the picture 5.15.

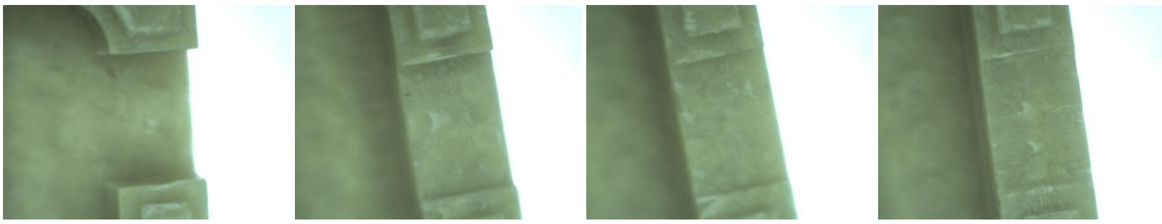

Figure 5.16: Gas distributor slits with decreasing size from left to right.

5.2 Design of Foils

All foils were designed using Altium Designer® under supervision and with support of Christian Honisch. The manufacturing is done by the CERN workshop of Rui de Oliviera. After first designs the workshop was also visited to benefit from the local experience and discuss possible improvements. The final designs will be discussed in the following.

5.2.1 GEM Foils

Since after assembly of one detector, it is not possible to exchange the GEM foils anymore. Even in the case of a short between upper and lower side of one GEM foil (which leads to an effective gain of 0), it is not possible to exchange such a foil.
Therefore, the foils are segmented on one side such that the detector could be operated even with a shorted segment. Without segmentation a whole detector gets unusable with just one shorted GEM foil. The perforation follows certain boundaries as depicted in fig. 5.17. The copper segments were separated by a 200 µm gap.
To avoid holes which are not completely surrounded by copper, there are additional 100 µm between edge of the holes and the copper rim.
The connection to the unsegmented side is made with a special via mentioned by the CERN workshop. As shown in fig. 5.18 it is a copper area with many holes in a smaller area which got filled with conductive metal. This way a high voltage stable connection is ensured.
The design of a foil with the segmented side on top is shown in fig. 5.19. The segmentation was adapted from the CG1G layout. All corners are rounded to avoid sparks. Moreover, the teardrop application from Altium was used to strengthen the transition from pads to tracks.

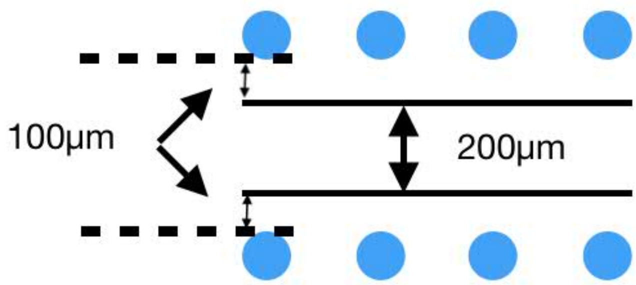

Figure 5.17: Illustration of GEM holes arrangement at edges. Blue dots represent the hole positions while the black lines depict the edges of adjacent segments.

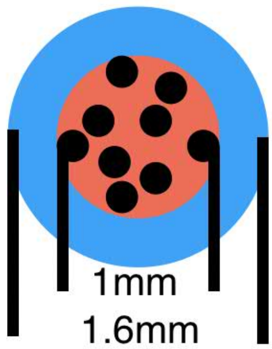

Figure 5.18: Illustration of HV stable via. Blue illustrates the whole via size of 1.6 mm while red defines the region where openings (black dots) will be for the conductive filling.

As one can see all tracks from the different segments are guided to one corner and further more sitting under the frame or in the gas volume after assembly. When coming out of the frame they are protected by a coverlay till the solder pads, which are also perforated to get a stable contact. The four holes further inside are for the gas system. In principal only one is necessary but since one want to use the same layout for all GEM foils at they will be later on rotated a hole for each configuration is implemented. In the vicinity are also crosses which will later be used to check the components of the foil. The four holes further outside are for the alignment system. In the outer region are test segments to later on measure the hole uniformity across the hole foil. The outer perforation, size and shape is compatible with the stretching system of the ALICE IROC which is available due to the production in Bonn for the TPC upgrade (concise: [41], extensive: [42]).

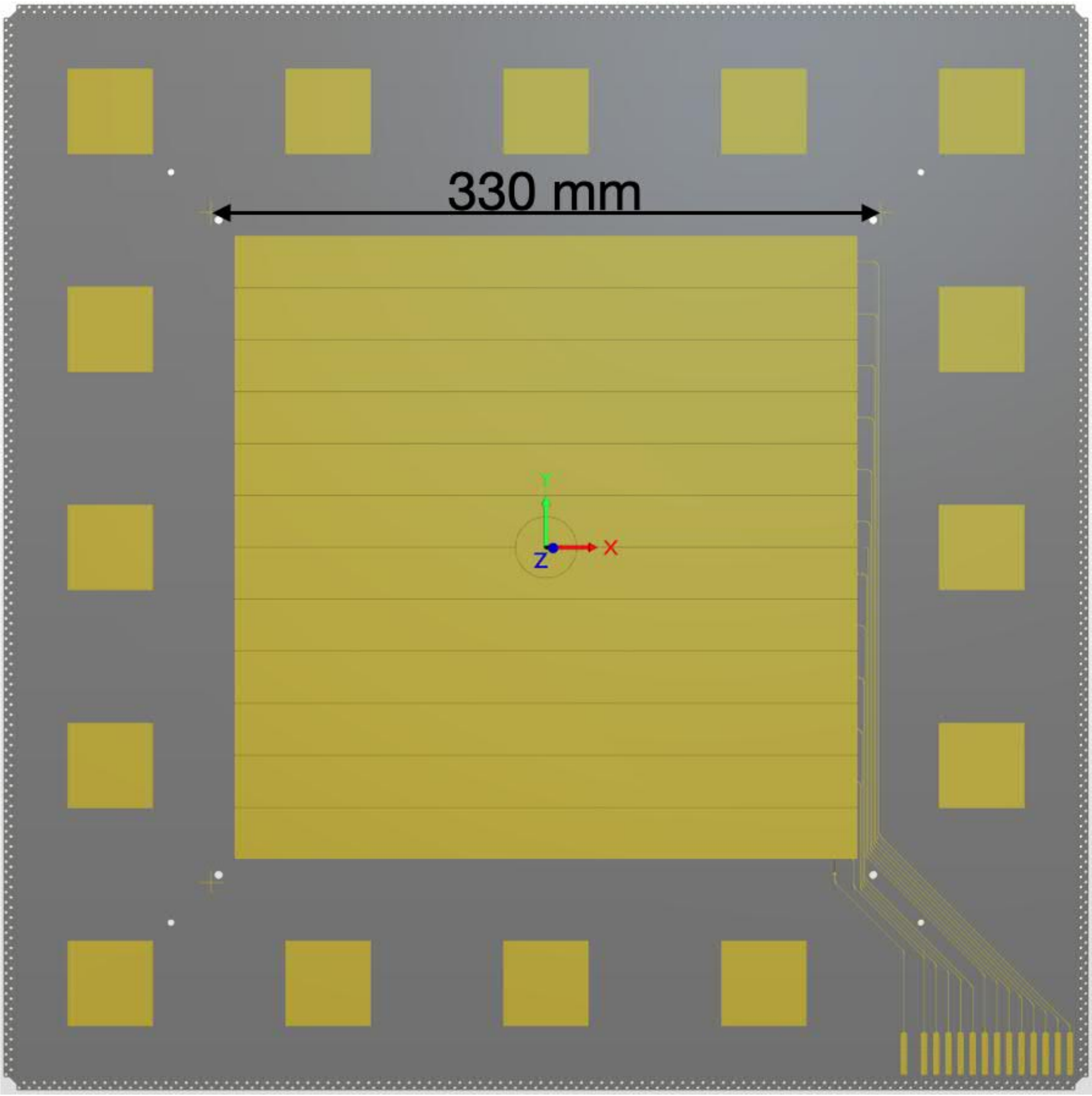

Figure 5.19: Altium 3D view of the GEM foil layout for CG3G.

5.2.2 Drift Foil

A one sided drift foil is used which means that their is only on one side a copper layer.
Double sided foils can be used to avoid charge collection on the insulator of the foil. This only makes sense if both sides are in the gas volume. Since the used drift foil is glued on one side to the support plate this is no issue. Therefore, the design can be derived from the GEM foils, but without the top layer.

5.2.3 Readout Foil

The foil is designed for a readout from all sides. Thereby, the strips are cut in the middle such that the occupancy is reduced. Every side requires six front end cards which will be connected via the Hirose FX10. The same is used for the VMM so that an upgrade to self-triggered readout could be made with the same readout foil.
Each of these connectors manages 128 strips what means that one hole readout foil contains 4 x 768 strips. The geometry is shown in fig. 5.20. The red bars represent the top strips while the bluish bars the bottom ones. Furthermore, it is possible to upgrade to a hybrid readout without additional connectors. By having continues strips for two out of six connectors one can use on each side the resulting two available for pixels in the centre.
By connecting specific pads of the several connectors to ground one can define fixed I^2C addresses. Therefore, the address of a front end card depends on the position where it is connected to the readout foil.

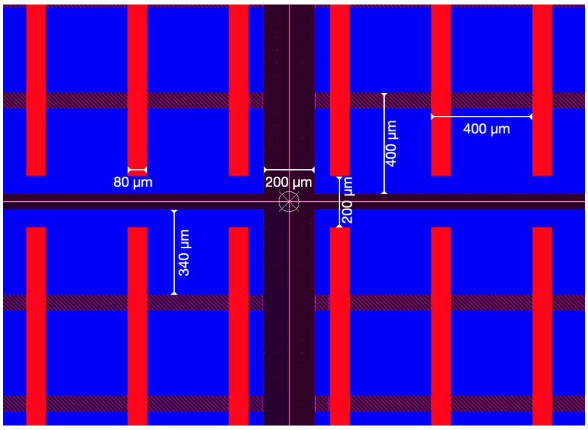

Figure 5.20: Altium construction view of a close-up of the readout foil for CG3G. The pitch is 400 µm for both coordinates. The red bars (top strips) have a width of 80 µm while the bluish (bottom strips) are 340 µm wide. The cut in the centre is a gap of 200 µm.

As one can see in fig. 5.21 five digits are available to define the address. The first defines the sector where one points to the direction, e.g. 11XXX - up, 00XXX - down, 10XXX - left and 01XXX - right. The orientation of the hole plane is given by the logo in the lower right corner. The squares behind each connector are additional grounding meshes on top and bottom side of the foil to limit noise. After consultation with the CERN workshop also vias had been resized and fanned out in more rows. That way one can achieve a higher probability for a successful manufacturing and in addition lower the cost [4].

[4] To guarantee a set of two fine foils the workshop does three and in case of full success one can get the third for less

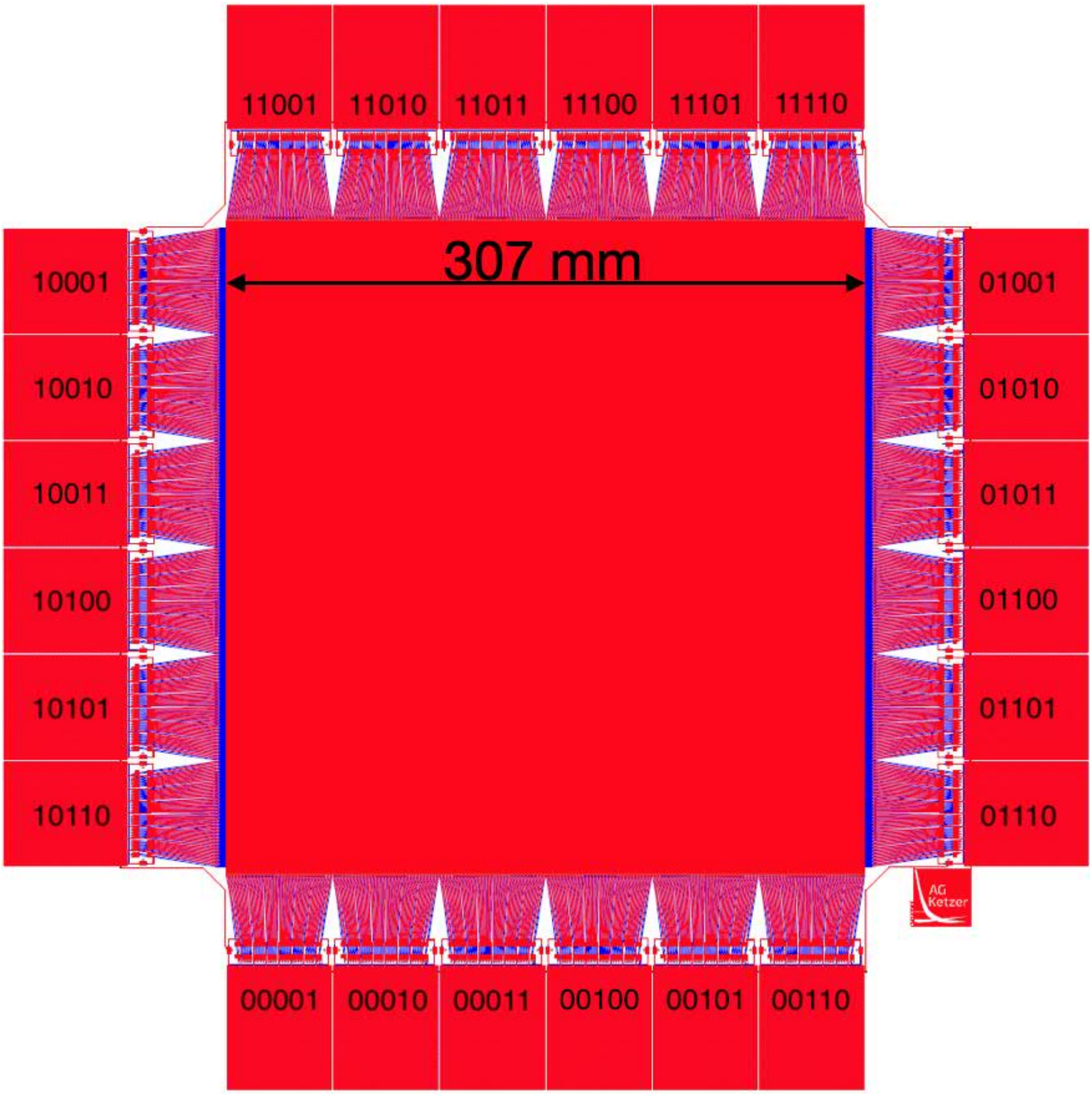

Figure 5.21: Altium construction view of the readout foil layout for CG3G where the layers are separated by different colours (red - top, blue - bottom). The binary numbers behind the connector positions are the corresponding hard mounted I^{2}C addresses.

5.3 Tooling

For the prototype production a hole tooling set has been designed. The aim is to be able to reuse existing equipment from the ALICE production in Bonn.
One part thereby is the stretching frame for an IROC GEM foil depicted in fig. 5.22. As recently mentioned in section 5.2 the design of the CG3G foils fit to this frame.

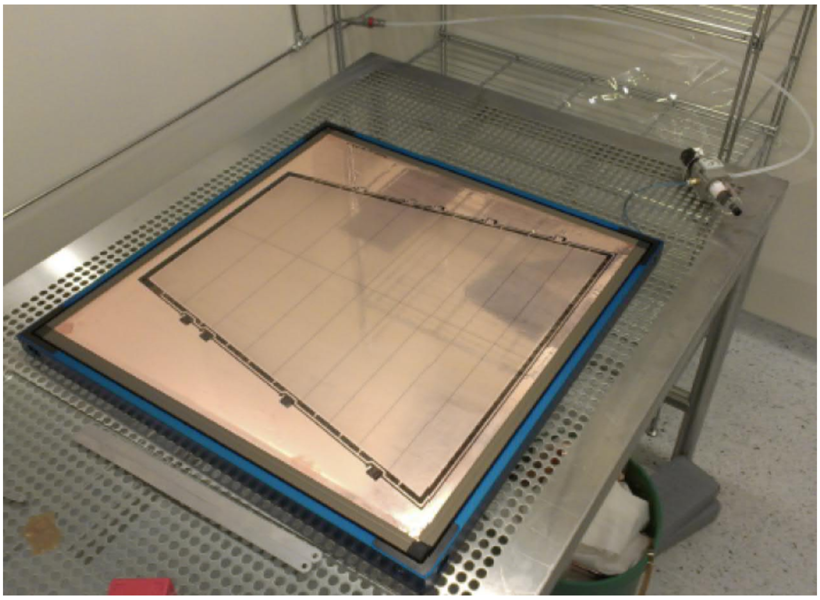

Figure 5.22: ALICE IROC GEM foil in stretching frame [42].

5.3.1 Glueing Equipment

The glueing equipment consists of the ALICE stretching frame, the glueing jig and the cover put on while hardening out. As mentioned in section 5.1.2 all frames came into the dry cabinet after entering the clean room. With inspection under the microscope and removing fibers sticking out the frames they are ready for further assembly.
The jig is modified to avoid any demolitions of the foils or frames. Therefore, the system only has contact through the frame region as well as cut-outs for the sensible GEM foil area in the middle.
Previous productions have shown that the glue can mess up the procedure by flowing in gaps and e.g. stick alignment pillars. To avoid this the glueing region is separated from that of the pillars. If somehow the frames are glued on the jig several holes from the bottom should give the possibility to release it with minimal stress on the material. Therefore, a thin stick would be used to solve each frame region through the holes by pressing up.

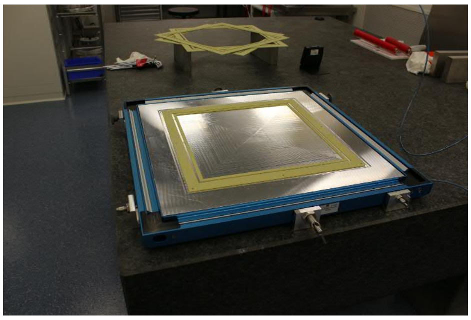

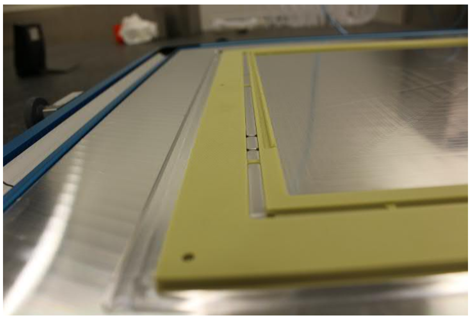

Figure 5.23: Glueing jig with stretching frame and readout frame on the left and a close-up on the right.

5.3.2 SDS Framework

As we have an **SDS** (**S**park **D**etection **S**ystem) in our clean room this should also be used for quality assurance. It also gives the possibility to check if their is any difference after framing or even damaging due to it.
To use this a new SDS inlet has been designed which fits to the foils of the CG3G. This than is put into the acryl glass box such as the electrodes will be automatically connected. One can test the foils in normal air or even in specific gas mixtures e.g. Ar/CO_2 (used in most of our test detectors in the lab). The hole SDS works better with the protective cover and lights out. This yields to lower noise and avoids fake sparks detected by the camera.
In addition of the optical observation with the camera the currents for each segment is monitored.
The SDS can also be used for high voltage cleaning. By applying the voltage normal dust gets burned from the surface of the GEM. Therefore, sometimes one can even "fix" a broken foil by burning away the connection of a short.

5.4 Stabilized Voltage Divider

The first idea was to split up the HV-distribution for each foil, such that one detector needs four smaller and more equal distributed PCBs.
Furthermore, one should be able to use four times the same PCB with adjusted components for the required voltages. The first draft in comparison to the HV-board of CG2G can be seen in fig. 5.24. Based on this a more complex design with active voltage division is in progress by C. Honisch [43] in close consultation.
The result is the **SVD** (**S**abilized **V**oltage **D**ivider), shown in fig. 5.25.
In comparison to the previous one the output impedance is changed to 10 kΩ instead of 10 MΩ. This leads in case of 1 μA load to a voltage drop of 10 mV instead of 10 V. In addition, the current can be limited for each GEM segment, e.g. 100 μA depending on the choice of resistance.
To lower the probability of sparks an over voltage protection is integrated. Therefore, the maximal voltage on a GEM could be limited e.g. to 500 V. One feature is the possibility to monitor the output voltages in the case of wrong settings or malfunctions. For now it is only considered to have this implemented for only the voltage divider without the GEM voltages.

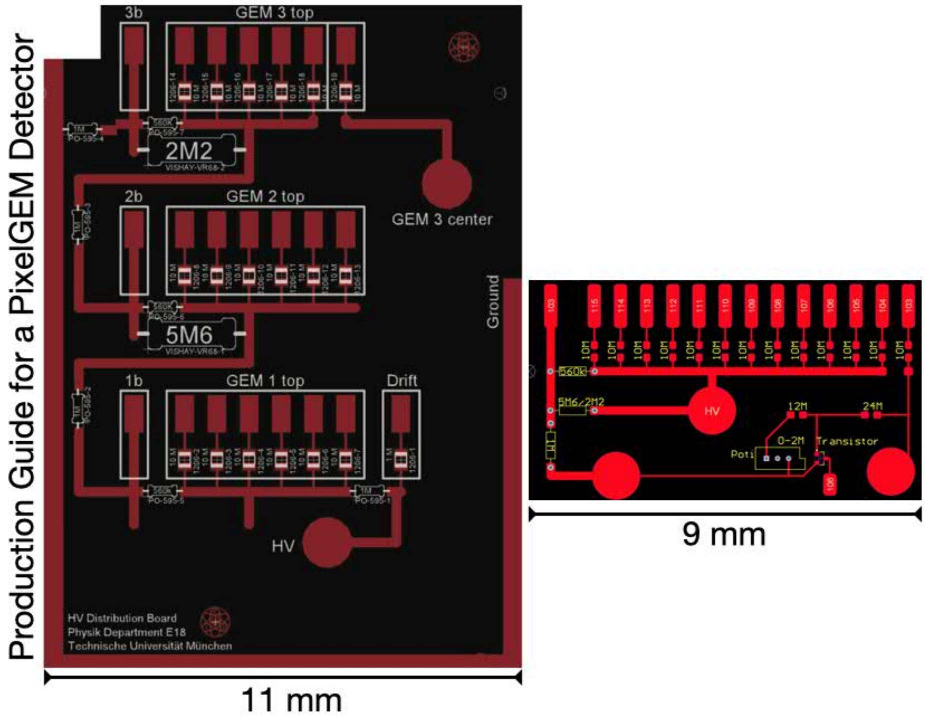

Figure 5.24: Comparison of resistor chain of CG2G [39] (left) and CG3G draft (right).

With the new design also some development is planned, as different voltage settings should be proved depicted in tab. 5.2. One is the standard which was used by COMPASS. The other is optimised[5] for electron transparency to achieve the same gain with a lower total voltage [15]. This should yield to better stability by equivalent performance. For a good comparison one can use the same detector and just switch the configuration on the SVD.

In fig. 5.25 one can see three yellow boxes. The left one is for changing the transfer voltages. In the middle the GEM voltages can be switched. And the right one can be used to adjust the value for the central area.

[5] Values achieved by simulation which can vary all electric fields to find a sweet spot (drift and collection field fixed)

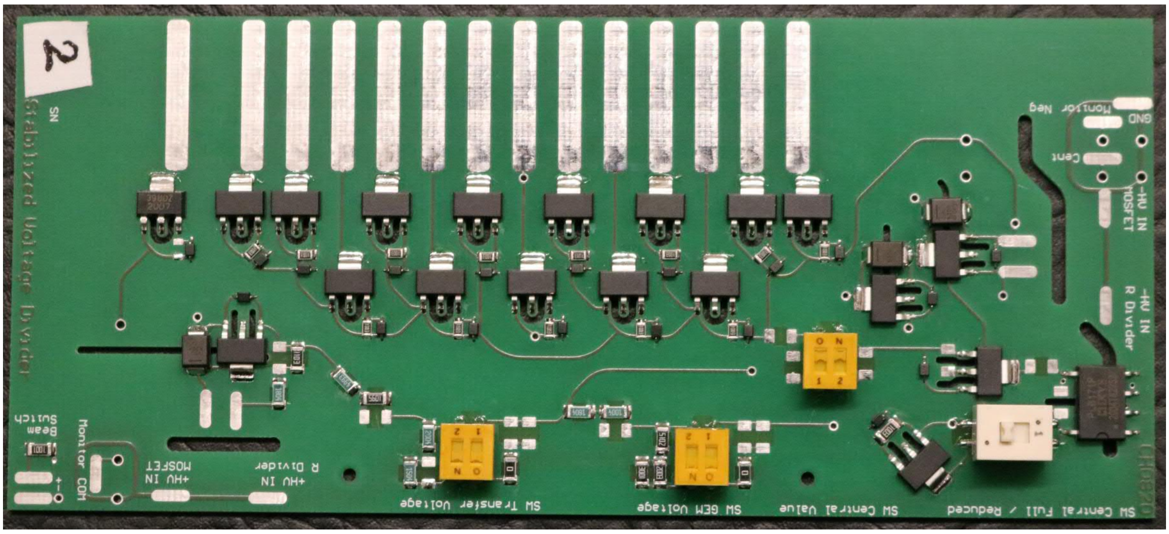

Figure 5.25: Picture of assembled SVD board.

Electrode	COMPASS / V	BONN[6]/ V
Drift	−4100	−3255
GEM1 TOP	−3353	−2508
GEM1 BOT	−2943	−2102
GEM2 TOP	−2196	−1751
GEM2 BOT	−1822	−1384
GEM3 TOP	−1075	−1068
GEM3 BOT	−747	−747
PCB	(GND) 0	(GND) 0

Table 5.2: Standard COMPASS settings [25] and BONN settings [15].

[6] **B**onn-**O**ttnad **N**eu-**N**ormal

5.5 Redesigned Readout chain

The whole readout chain is redesigned to general update the components. E.g. in case of the connectors on the front end card the previous ones are no longer produced. One aim is the possibility to upgrade the readout to be self-triggered. One candidate for this would be based on the VMM3 chip [44].

5.5.1 APV Front-End

The **APV** (**A**nalog **P**ipeline **V**oltage) front-end was designed by C. Honisch [43] with assistance of mine. One can see the sides of the PCB in fig. 5.26 including a close up of the APV25 S1[7] chip [45]. A single front end card will manage 128 channel which means that a total of 24 are needed for one detector as discussed in section 5.2.3.

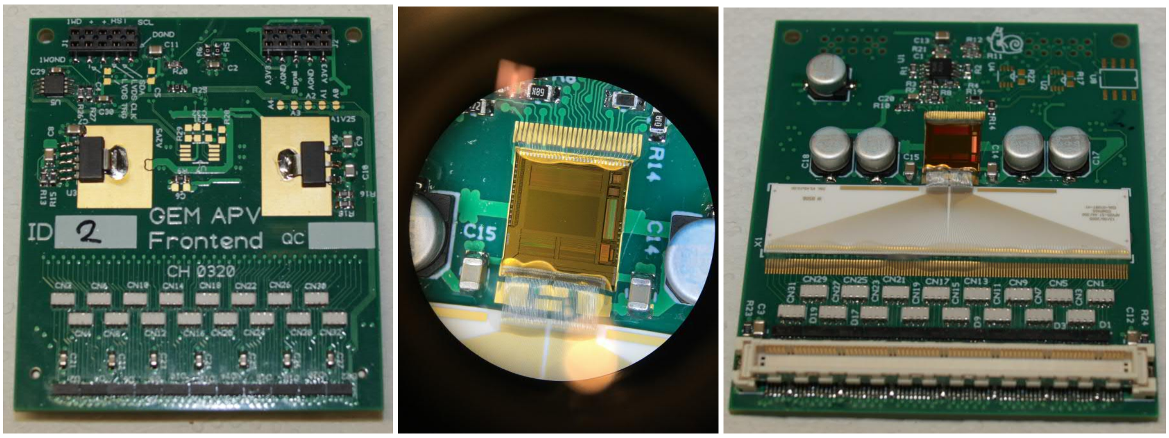

Figure 5.26: Front end card with APV25 S1 chip. The two sides of the board can be seen left and right. In the centre one sees a microscope picture of the chip.

A major change is the improved input protection. The previous small signal diode (BAV99) is thereby exchanged with a genuine ESD protection diode (SP3012-06) - a component which is developed for exactly this. This results in a better over voltage limiting (up to factor 2 with preliminary simulation [43]).
Also the parasitic capacity is lower with 0.5 pF compared to 2 pF. A higher parasitic capacity would directly impair the noise of the detector.
Additional, a temperature sensor is placed on the board which can be controlled over I^2C. While the I^2C address of the front end card is defined over the connection to the detector, explained in sec. 5.2.3.
Connections to the chip and the ceramic substrate were made with wire bonding.
The ceramic substrate with gold tracks is used to fan out the small pitch on the APV side to a larger pitch on the input protection side which is sufficient for common productions. One has to mention that there are only around 50 of this substrates which are already left overs from the last production[8]. Here a other solution could be high precision aerosol jet printing [46]. Currently some older samples will be sent to a company such as they can test the manufacturability. In case this option gets real, ID3-6

[7] Analogue pipeline **ASIC** (**ASICA**pplication-**S**pecific **I**ntegrated **C**ircuit) developed for silicon strip readout by CMS.
[8] Remaining stock which was bought up entirely from the manufacturing company.

are already reseved for this process.

5.5.2 Supply-Card

The supply-card was designed by C. Honisch [43] with assistance of mine.
It is used to connect the front end cards with the ADC. Thereby, the front ends are stacked each on two pairs of pins and the ADC is reachend via a ribbon cable. The supply card can be seen in fig. 5.27.
To avoid shifts clock, trigger and analogue signals are matched with over track lengths which is the reason for the additional curves of some lines. Moreover, it concentrates the analogue signal of six front ends. 3.3 V are required with an maximum consumption of 3 A. One has to mention that this is an upper limit and over the normal operation.
With an input output register which can be used via I^2C it is also planned to maintain the central area of the GEM foils by this.

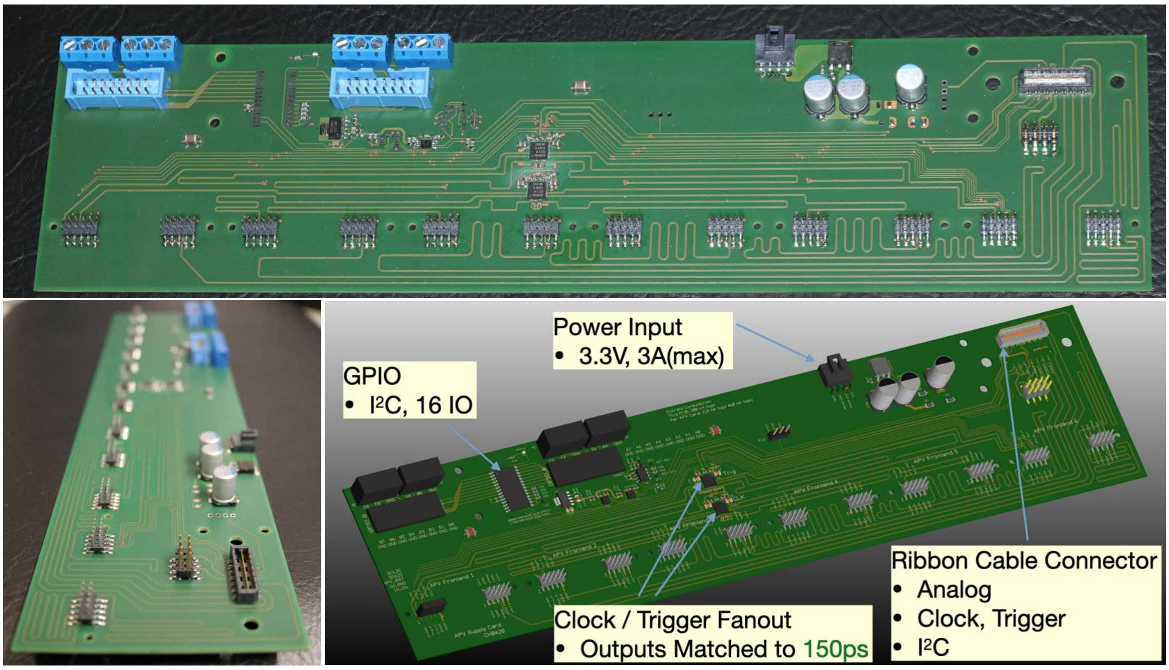

Figure 5.27: Supply card in Altium design view and as equipped PCB [43].

CHAPTER 6

APV Measurements

In this chapter the first measurements with the new APV front-end (APV FE) boards are discussed. The aim is to prove stable operation and figure out some improvements concerning small changes of some electronic components.
Therefore, the test setup that was used for the measurements is explained in section 6.1. After this in section 6.2 it will be shown how one can reconstruct the incoming pulse shape by using the new APV front-end. And therefore, it is tested if the new design behaves as expected. The last section 6.3 focuses on the calculation of the ENC for the different configurations of the new APV front-end design.

6.1 Test Setup

The test setup used for debugging and further measurements is depicted in fig. 6.1.
For the following results the HAMEG HMP 4040 power supply (upper left) was used to power the ADC (board shown in the upper right) while for the APVs the TENMA T2-10505 (upper centre) was taken. Especially during the debug phase the over current protection was very useful to avoid destruction on the circuit boards.
For monitoring the digital outputs, test pulses and the trigger a DSO-X 4034A oscilloscope (shown in the lower centre) from Agilent Technologies were used. During some measurements test pulses were generated with the 33250A function generator (shown in the lower right) from Agilent Technologies.
The schematic of the setup in illustrated in fig. 6.2. The ADC requires ± 5 V and the transition card is powered with $+3.3$ V and -1.7 V. Both are stacked together. Additionally the APV can be stacked on the transition card for test measurements. If test pulses are required or additional capacities are needed a detector dummy is stacked on the APV. In case of test pulse injection the ADC is triggered delayed to the signal generator such that the APV is triggered after the test pulse. The oscilloscope is used to illustrate the trigger signal, the test pulse and the test outputs of the transition cards, e.g. analogue outputs of the APV.

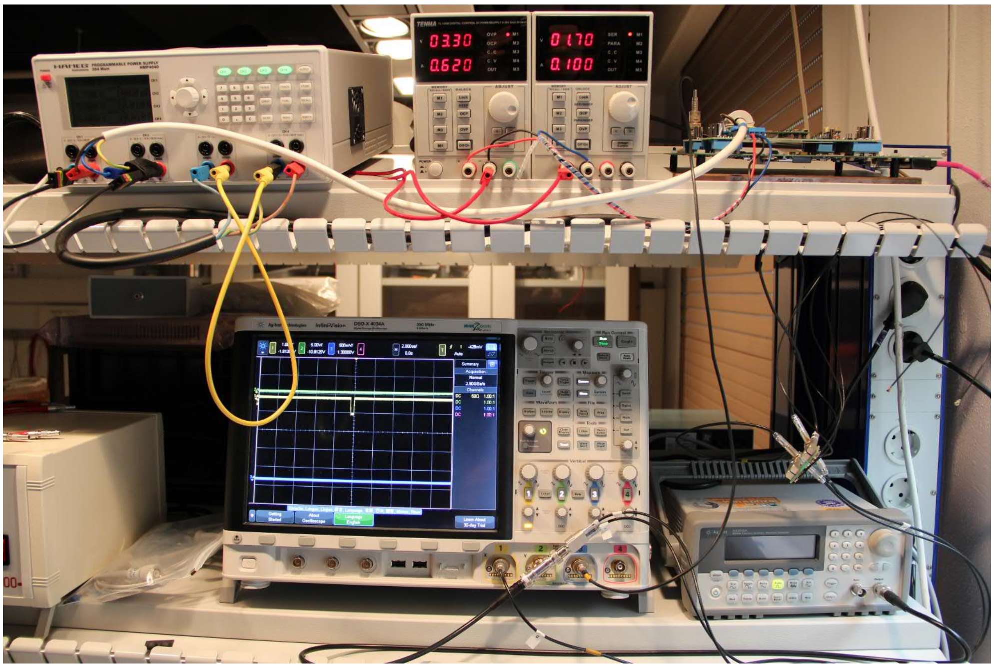

Figure 6.1: Picture of the test setup in the lab.

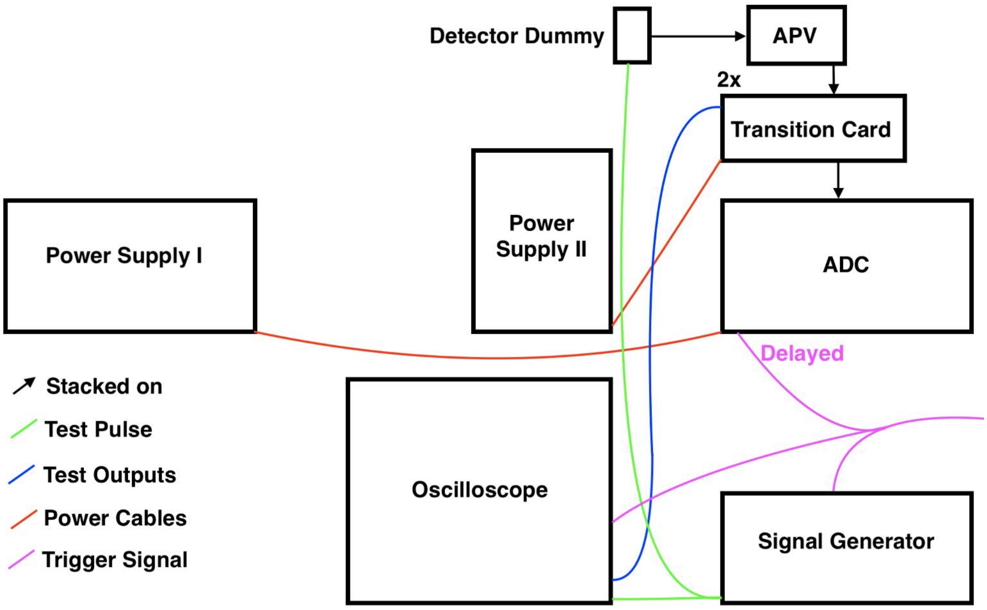

Figure 6.2: Schematic of the test setup in the lab.

6.1.1 Front End Test Station

The current test station is operating with one of the older ADCs. Technically it would be possible to read out 16 APVs with this. For the test phase a transition card was made by C. Honisch [43] which allows the usage of two new APV front end cards on one older ADC. A picture of this can be seen in fig. 6.3.

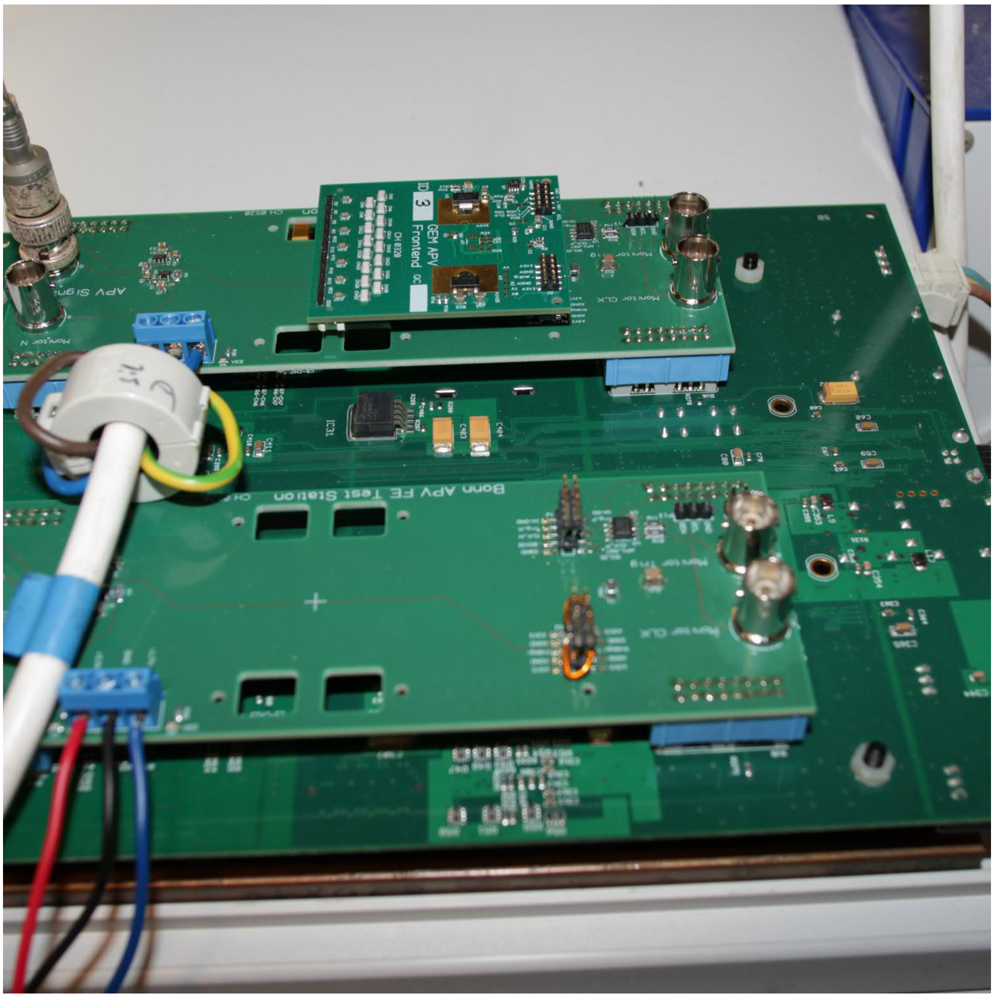

Figure 6.3: Picture of the test station for first APV-FEs. Shown are both transition cards with the ID3 FE stacked on the back one.

One transition card has also four outputs which can be used to display the analogue APV outputs or the trigger and the clock given by the ADC.
For the first test three different configurations were used as listed in tab. 6.1.
The switched polarity was a mistake by ID1&2 and one of the transition cards has been modified for this. Therefore, the analogue signals where bridged with cables to the opposite polarity. To prove if the position of the temperature sensor has an influence on the performance two different spots where used.

For ID3 the line driver is removed as the APV chip should have already something similar implemented. A concise walk through the debug process is mentioned in appendix A.4.

FE ID	Temp.-Sensor Position	Polarity	Line driver
ID1	centre	switched	yes
ID2	left	switched	yes
ID3	left	standard	no

Table 6.1: Different front end configurations.

6.1.2 Detector Dummy

The detector dummy was designed by C. Honisch [43] to imitate the capacity of an detector.
It can be directly put on the APV front end and is also used for some VMM measurements in our lab. One example is shown in fig. 6.4.The standard capacity is 30 pF which would be expected for the strip readout. This yields for all channels expect of channel 0 and 1. There one has 8 pF and it is possible to add independent 30 pF, 68 pF and/or 330 pF. With this it is possible to measure e.g. the noise dependence of the input capacity.
Another six switches can be used to set the I^2C address. Every dummy can also be used to inject test pulses. Here one can choose between eight slots. Each contains 16 channels. Thereby, these are differentiated to even or odd channels. E.g. by connecting the upper right slot one would inject the test pulse to the first 16 odd channels (the 128 front-end channels are divided into eight groups).
For the dummy used in following measurements all slots where tested to deliver almost the same signal. That means that the deviation of single components could not yield to a change monitored with the oscilloscope[1].

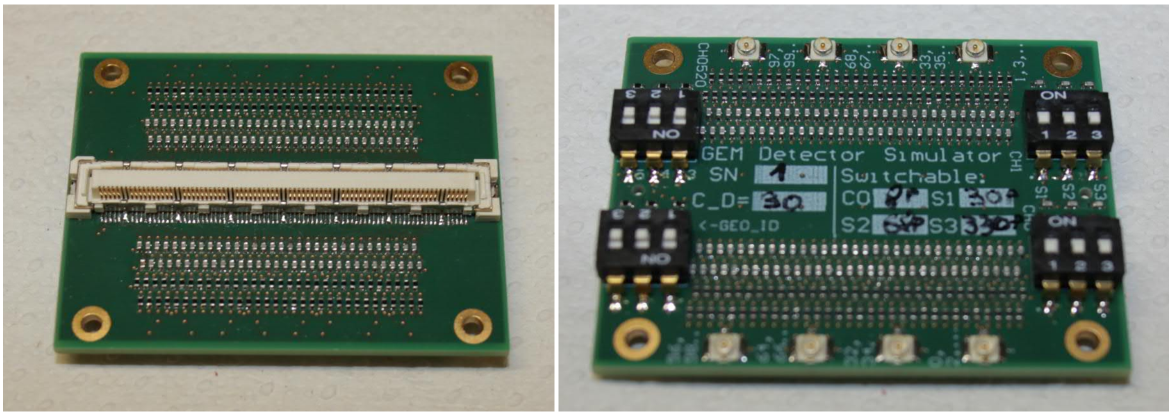

Figure 6.4: Detector dummy to simulate capacities and signals. The bottom side that can be connected to the APV is shown on the left side. On the right side the top side is depicted where the eight injection slots are visible. The switches on the left are used for the I^2C address and the right ones to differ the capacities for the first two channels.

[1] The resulting measured amplitude was identical without displayed fluctuations

6.2 Latency Scan and Pulse Shape

With a latency scan it is possible to reconstruct the shape of a pulse.
Normally, it is used to find the signal to have the latency fixed for later measurements. For such a propose the detector dummy has to be connected.
Before performing a latency scan one has to take pedestals. These will be used to subtract the background from the data while a physics measurement. A detailed description for taking pedestals and performing a latency scan can be found in [47]. By this measurement the functionality of the new APV board is tested. Therefore, the concept of the method is explained in section 6.2.1 before results are presented in section 6.2.2.

6.2.1 Concept

The APV25 S1 chip is operating with a 40 MHz clock by sampling the incoming signal every 25 ns for each of the 128 channels. The signal processing and sampling of the chip is illustrated in fig. 6.5. After preamplification and shaping the signal gets sampled analogue. If a trigger occurs the latency defines which analogue samples are fed in the multi event buffer. If the APV is operated in three sample mode, three consecutive samples are taken from the analogue sampling (known as pipeline). In the last step the 128 channels are reduced by the MUX (Multiplexer) to one outgoing data stream. This process can be optimised by setting the latency. Therefore, one can adjust the processing such that the three samples are sitting on the rising edge of the signal.

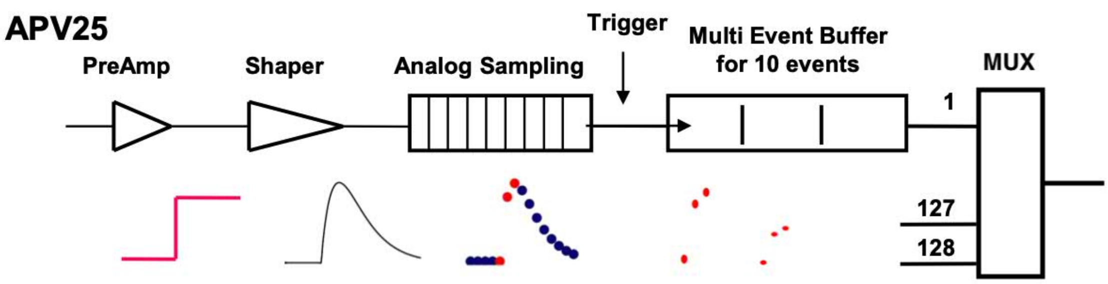

Figure 6.5: Signal processing and sampling of the APV chip [2].

By scanning over the range where some higher amplitudes were observed one can raster over the incoming signal, shown in fig.6.6 and reconstruct it afterwards. For this the three sample mode of the APV is used. That means one can take three samples each shifted by one latency (25 ns). How this is displayed in the analogue output of the APV is shown in fig. 6.7. There it gets visible how the amplitude for hit strips rises during the 25 ns delays. It also clarifies how data bunches sit between the digital information streams. This output can be monitored over the transition card with the oscilloscope while data are taken.

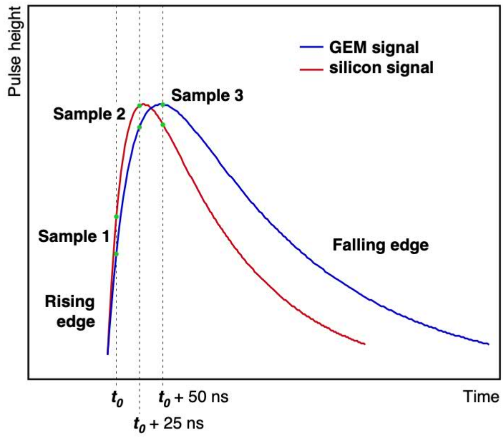

Figure 6.6: Signal shape with optimal timing for three samples [48].

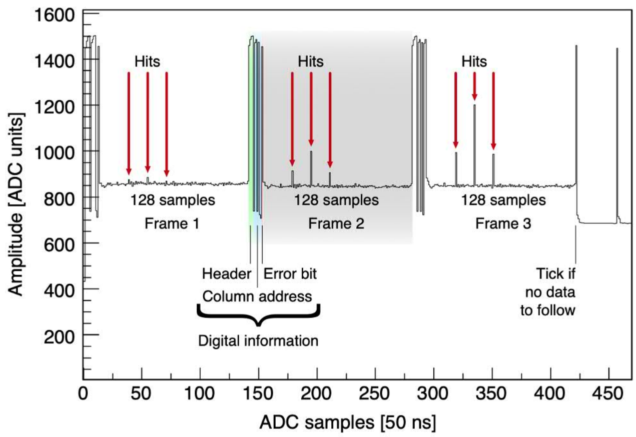

Figure 6.7: APV25 output in three sample mode connected to a GEM detector with hit [48].

To ensure that the test pulse is registered the position of the signal was shifted manual before the measurement. Therefore, the trigger for the pulse generator was just shifted before the trigger of the APV. With some fine adjustment the maximum of the signal was matched to a latency of 26.

6.2.2 Results

The amplitudes were been measured between latency 30 and 14. By knowing that the maximum is positioned at latency 26 this should guarantee a proper scan of the signal shape. In theory one can simply reconstruct the pulse shape inserted on each channel.
Therefore, a histogram has to be filled with all amplitudes for each latency. To demonstrate this the histograms for a random channel of ID1, ID2 and ID3 are depicted in fig. 6.8. The strange pattern for two of three adjacent bins is caused by the APV output combined with binning.
Using the three sample mode there is a different scaling concerning the different samples.
Therefore, the first sample is scaled in multiples of two ADC channels while the others are scaled in multiples of four ADC channels. That results in a continuous filling of every third latency while for the other two every second entry in amplitude is empty. Seeing this in the analysed data is an additional prove that the chip works like expected.
As the test pulse was the same for ID1, ID2 and ID3 one can already see that the output signal without a line driver is higher. The comparison of ID1 and ID2 shows no notable deviations. Overall, it is shown that the redesigned APV front end boards work like expected because the reconstruction works as predicted in section 6.2.1.
First comparisons during the debugging phase have also shown that the noise without additional capacities might be better compared to the previous APV front-end card (both cards were red out with the same ADC during debugging).

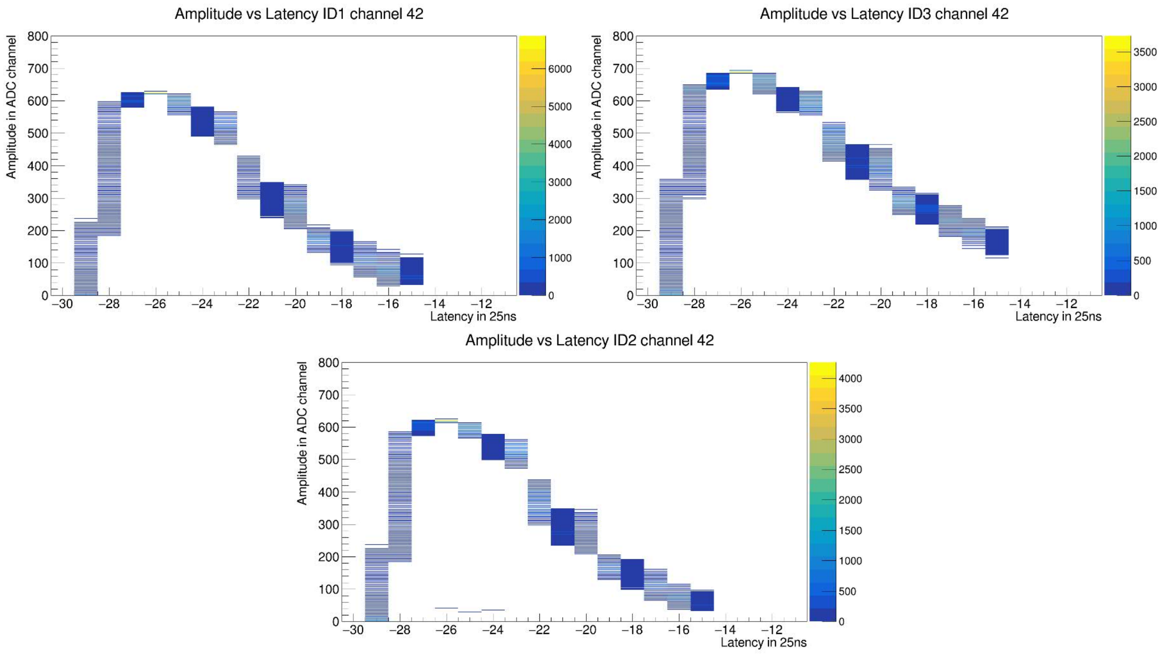

Figure 6.8: Two dimensional histograms of the pulse shape. The latency is plotted against the amplitude. On the the left picture for ID1, the lower for ID2 and on the right for ID3.

6.3 ENC for different APV-Frontends

The calculation of the **ENC** (**E**quivalent **N**oise **C**harge) for the different front end configurations, shown in tab. 6.1, should provide an answer if a line driver improves the performance or can be removed. For that the concept of the measurement is explained in section 6.3.1. Finally, the results are presented and discussed in section 6.3.2.

6.3.1 Concept

The ENC is a quantity which estimates the signal quality regardless of the gain. By definition it gives a ratio of noise and signal in terms of #e$^-$ [43]:

$$ENC = Q_{\text{Signal}} \frac{Noise}{Signal} \tag{6.1}$$

where:

Q_{Signal} = input signal in #e$^-$
$Noise$ = noise in ADC channel
$Signal$ = output signal in ADC channel

To get the $Signal$ the mean of the latency with the highest amplitude was extracted. While the $Noise$ can be taken from the pedestal file in form of the standard deviation. This is done for each channel.

Q_{Signal} can be derived by taking a closer look at the schematic, see fig. 6.9, of the detector dummy where the test pulse is injected.

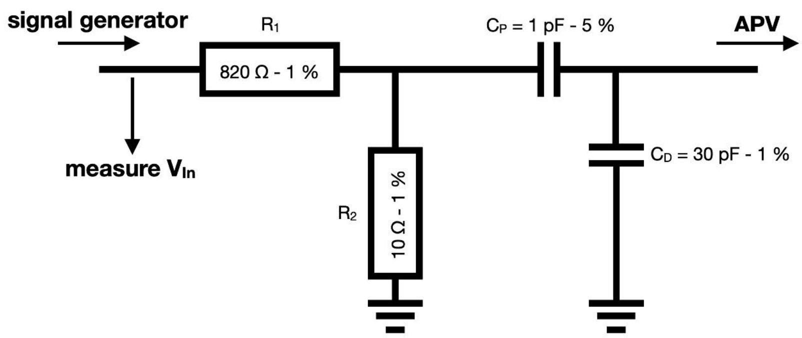

Figure 6.9: Detector dummy circuit for input charge calculations. Manufacturer tolerances given in percent. Important is that these give a range of possible values from the component - the actual fluctuation is lower.

Therefore, it can be calculated in dependence of the input voltage V_{In}:

$$Q_{\mathrm{Signal}} = V_{\mathrm{In}} \frac{R_2}{R_1 + R_2} C_{\mathrm{P}} = V_{\mathrm{In}} \frac{10\,\Omega}{820\,\Omega + 10\,\Omega} 1\,\mathrm{pF} \tag{6.2}$$

To imitate a pulse comparable with the signal of a MIP the input voltage was set to 3.2 V. This is calculated with the typical values[2] for the COMPASS triple GEM tracking detectors. A MIP on average leaves a track with 100 electron–ion pairs/cm in Ar/CO_2 [31]. For a 3 mm drift gap this results in 30 electron–ion pairs between drift cathode and the first GEM stage. After amplification one has 240 000 electrons above the readout. Using equation 6.2 one obtains the 3.2 V.

6.3.2 Results

The results of the measurement can be seen in fig. 6.10 where the ENC is plotted against the channel number. For better comparison the scale is the same for both graphs.
Therefore, one can directly see that in case of no line driver the ENC is lower. The comparison of ID1 and ID2 shows no notable deviations. The errors are a upper limit since the manufacturer errors were taken for Gaussian error propagation[3].

[2] 3 mm drift gap in Ar/CO_2 70/30 with a total effective gain of ~8000 [34] over all GEM stages.
[3] Not 100 % accurate since the manufacturer tolerance defines a window in which the value will lie. The actual fluctuation of the value should be much lower.

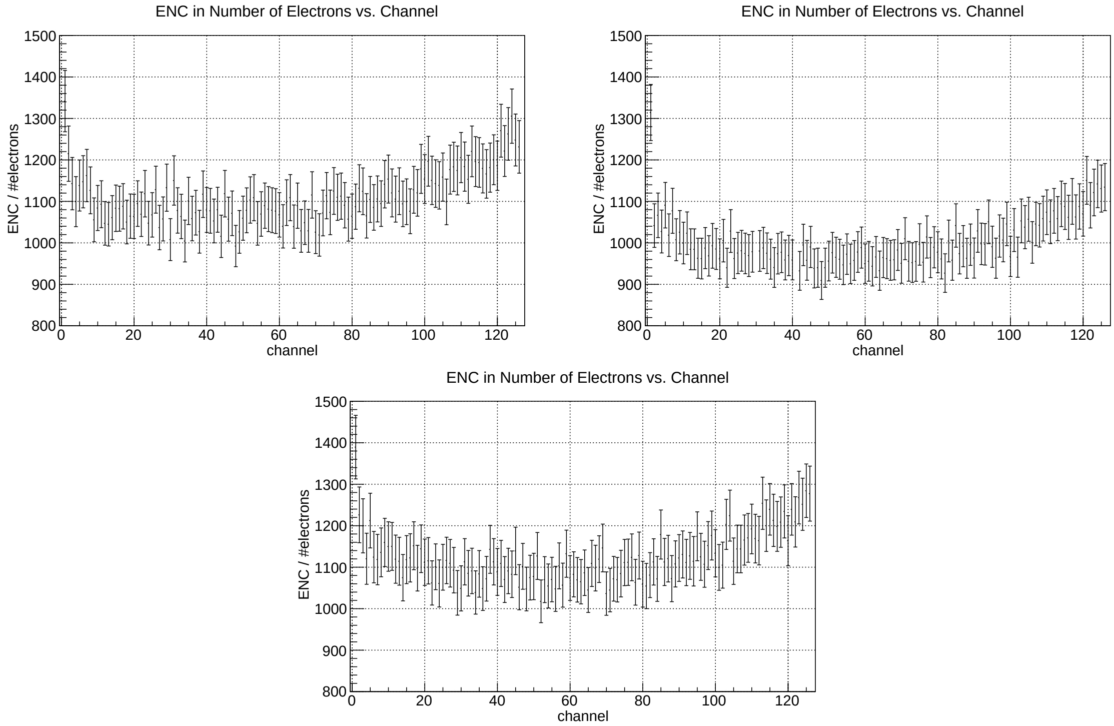

Figure 6.10: ENC results for each channel. Left for ID1 (with line driver), centre for ID2 (with line driver) and right for ID3 (without line driver).

Remarkable about all measurements is the smirk shape created by the data points. The reason for this could be the increasing track length which would yield to a higher noise on the ceramic substrate for outer channels. This could not yet be fully understood and appeared in previous times also. A possible ansatz for this problem could be an aimed variation of different track lengths between connector (on detector side) and chip.

Another strange thing is the increased value for the first two channels. The reason for that is the construction of the detector dummy. By switching on the additional 30 pF for the first two channels the total value is set to 38 pF which is at least 8 pF more than the other channels. This causes higher noise and brings the step in the progression.

With this measurement it is shown that the APV front-end performs even better without the line driver. Thus, it may will be removed in further productions.

Comparing the results with the input noise of the APV25 S0, shown in fig. 6.11, one expects a noise of approximately 1 200 electrons for a input capacity of 30 pF which fits roughly to the measured values of ID1 and ID2. A comparable measurement for the APV S1 is shown in fig. 6.12. By extrapolating a value of the ENC for 30 pF one would expect 1 410 electrons. This value is higher than each measured with our setup. A reason for that could be that they are using a front-end which adds higher noise to the raw chip noise. Interesting in the values of [49] is that they have not observed this smirk shape along the channels since channel 2,43 and 107 (for smirk shape one would expect a higher ENC for channel 2 and 107 in reference to channel 43) show similar results.

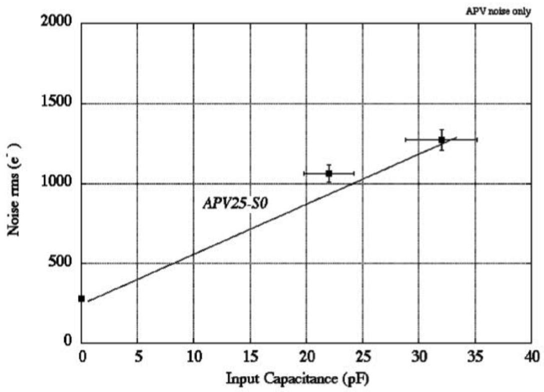

Figure 6.11: Computed (full line) and measured input noise as a function of strip capacitance for the APV25 S0 [33].

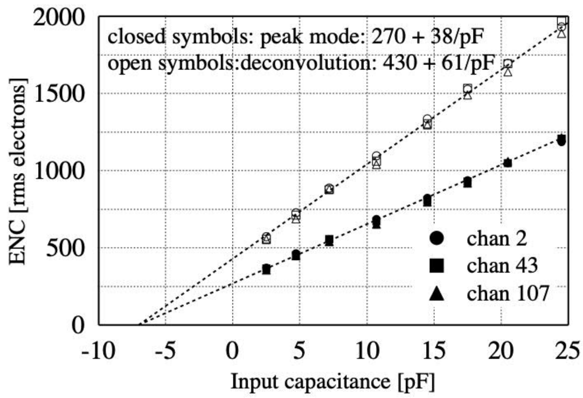

Figure 6.12: APV25 S1 noise against input capacitance [49].

CHAPTER 7

Summary and Outlook

In this thesis a whole triple-GEM-tracking detector for the COMPASS++/AMBER upgrade was designed. Starting with an intense study of previous triple GEM-based detectors to find possible improvements for a new detector series. This process can be find in chapter 4. As a result a design was created to fit to many requirements. On the one hand the usage as replacement for the CG1G detectors which sets hard boundaries for huge developments, e.g. the overall design has to fit in the experiment exactly like the previous versions. Therefore, the new CG3G is suitable for the already existing mounting structures in the COMPASS spectrometer and will have a large active area of 30.7 cm $\times$ 30.7 cm. On the other hand one needs further developments due to the increasing requirements by the experiment itself, e.g. higher rate capabilities. This yields to other modifications in the design which are further explained in chapter 5.
With the claim to hold the backward compatibility and prepare for future upgrades at the same time, e.g. the strip readout is cut in the middle and thus the double amount of front-end cards is needed. With this step it gets more accessible to further upgrade to a hybrid readout with pixels. Another advantage is the exchange of the connectors for the connection to the readout plane because these are also used for the VMM3 chip. Therefore, a test with a new self-triggered readout scheme can be done with minor modifications. This directly corresponds to a possible handling of higher rate capabilities. Additionally, each detector part and corresponding tooling has been designed to optimise either the manufacturing and/or the performance in the experiment. For example, the gas system through the frames should grant a stable and equal flux of the active medium (gas). This is achieved by glueing rims which avoid any blocking in the corridors of the gas system as described in 5.1.
Beside the design of the detector, measurements with the new APV front-end card have been performed and discussed in chapter 6. There it was successfully tested that the new board operates so far like expected by reconstructing the shape of a test pulse. This was done for three different front-end configurations. At last a measurement of the ENC was performed. Thereby, it was found that the performance can be further improved by removing the line driver. A comparison of the used APV25 S1 and the same chip used in another experiment depicts that the measured ENC is lower than the one measured in [49]. A reason for this could be a higher additional noise caused by the different front-end designs.

Finally, this thesis should be interpreted in the context of the triple-GEM-tracking detector development at the COMPASS spectrometer. Fig. 7.1 demonstrates that the detector designed in this thesis is a indispensable part. The CG3G can replace the CG1G and grants a good base for CG4G and CG5G. For that the CG3G has to be build and tested. In addition, further studies of the front-end electronics have to be done.

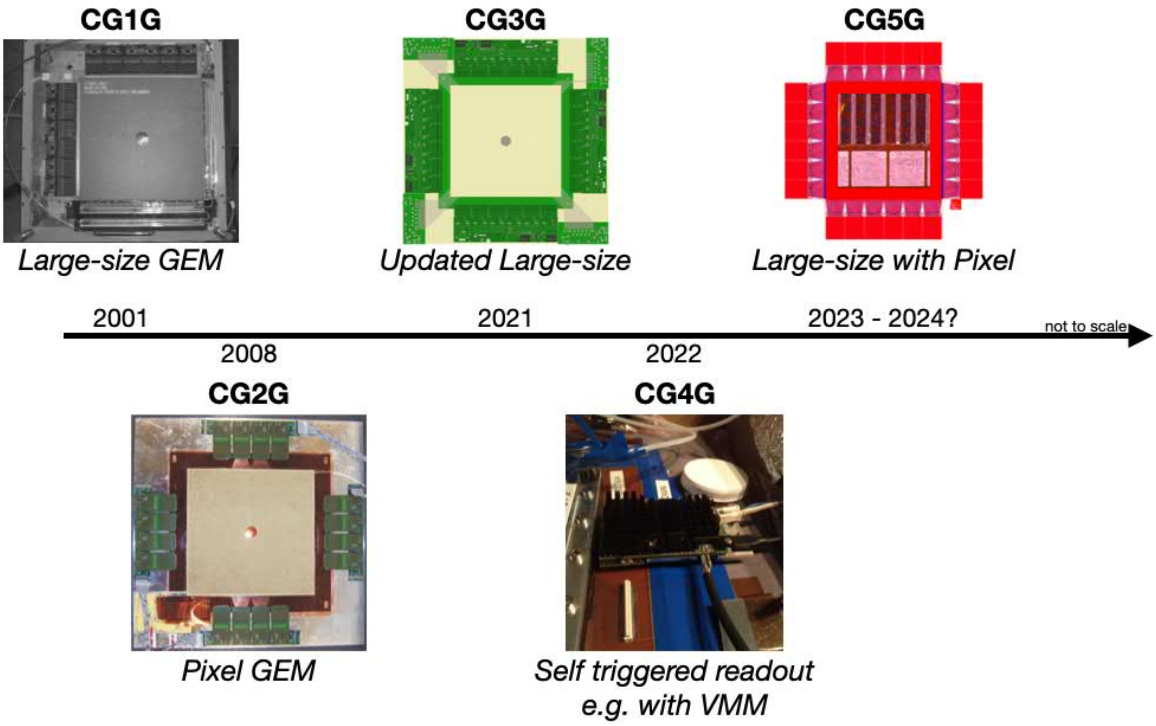

Figure 7.1: Schedule for the COMPASS GEM generations.

Bibliography

[1] A. Einstein, *Die Grundlage der allgemeinen Relativitätstheorie*, Annalen der Physik **49** (1916) 769, URL: http://myweb.rz.uni-augsburg.de/~eckern/adp/history/einstein-papers/1916_49_769-822.pdf (cit. on p. 3).

[2] B. Ketzer, *Advanced Gaseous Detectors - Theory and Practice*, Lecture script, Summer term 2019 (cit. on pp. 4, 10, 17, 22, 51).

[3] H. Kolanoski and N. Wermes, *Teilchendetektoren, Grundlagen und Anwendungen*, 1st ed., Springer, 2016, ISBN: 978-3-662-45349-0, URL: https://doi.org/10.1007/978-3-662-45350-6 (cit. on pp. 4, 5).

[4] K. Kleinknecht, *Detektoren für Teilchenstrahlung*, Teubner Studienbücher, Teubner, 1984, URL: https://cds.cern.ch/record/102101 (cit. on pp. 5, 6).

[5] W. Demtröder, *Experimentalphysik 4: Kern-, Teilchen- und Astrophysik; 2nd ed.* Springer, 2005, URL: https://cds.cern.ch/record/829123 (cit. on p. 6).

[6] M. Titov, *Perspectives of Micro-Pattern Gaseous Detector Technologies for Future Physics Projects*, 2013, arXiv: 1308.3047 [physics.ins-det] (cit. on p. 6).

[7] M. Altunbas et al., *Aging measurements with the Gas Electron Multiplier (GEM)*, Nuclear Instruments and Methods in Physics Research Section A: Accelerators, Spectrometers, Detectors and Associated Equipment **515** (2003) 249, Proceedings of the International Workshop on Aging Phenomena in Gaseous Detectors, ISSN: 0168-9002, URL: http://www.sciencedirect.com/science/article/pii/S016890020302477X (cit. on p. 6).

[8] D. Watts et al., "Performance of MPGDs with portable readout electronics", *2008 IEEE Nuclear Science Symposium and Medical Imaging Conference and 16th International Workshop on Room-Temperature Semiconductor X-Ray and Gamma-Ray Detectors*, 2008 919 (cit. on p. 6).

[9] R. Bouclier et al., *The Gas electron multiplier (GEM)*, IEEE Trans. Nucl. Sci. **44** (1997) 646 (cit. on p. 6).

[10] R. Bouclier et al., *The Gas electron multiplier (GEM)*, (1996), ed. by E. Barsotti, E. Hoffman and F. Kirsten (cit. on p. 6).

[11] F. Sauli, *GEM: A new concept for electron amplification in gas detectors*, Nucl. Instrum. Meth. A **386** (1997) 531 (cit. on p. 6).

[12] P. Hauer et al., *Measurements of the Charging-Up Effect in Gas Electron Multipliers*, arXiv: Instrumentation and Detectors (2019) (cit. on pp. 6, 9).

[13] F. Sauli, *The gas electron multiplier (GEM): Operating principles and applications*, Nucl. Instrum. Meth. A **805** (2016) 2 (cit. on p. 7).

[14] S. Duarte Pinto et al., *Progress on large area GEMs*, JINST **4** (2009) P12009, arXiv: `0909.5039 [physics.ins-det]` (cit. on pp. 7, 8).

[15] Jonathan Ottnad,
Optimierung der GEM-basierten Verstärkungsstufe einer TPC für das CB/TAPS-Experiment, PhD thesis: Rheinische Friedrich-Wilhelms-Universität Bonn, 2020,
URL: `http://hdl.handle.net/20.500.11811/8516` (cit. on pp. 9, 42, 43).

[16] B. Ketzer, *A Time Projection Chamber for High-Rate Experiments: Towards an Upgrade of the ALICE TPC*, Nucl. Instrum. Meth. A **732** (2013) 237, ed. by T. Bergauer et al., arXiv: `1303.6694 [physics.ins-det]` (cit. on p. 9).

[17] Viktor Ratza, *Multi-stage Micropattern Gaseous Detectors for the ALICE TPC Upgrade - Studying and Modelling Charge Transfer and Energy Resolution*,
PhD thesis: Rheinische Friedrich-Wilhelms-Universität Bonn, 2020,
URL: `http://hdl.handle.net/20.500.11811/8421` (cit. on p. 9).

[18] M. Capeáns, *Estudio del envejecimiento de los detectores gaseosos y soluciones para la utilizacion de MSGCs en experimentos de alta luminosidad*,
PhD thesis: Santiago de Compostela U., 1995 (cit. on p. 10).

[19] M. Capeans, *Aging of gaseous detectors: Assembly materials and procedures*, ICFA Instrum. Bull. **24** (2002) 85 (cit. on p. 10).

[20] M. Capeans, “Materials and gases: Lessons for detectors and gas systems”, 2001, URL: `https://doi.org/10.1007/978-3-662-45350-6` (cit. on p. 10).

[21] M. Capeans, *Aging and materials: Lessons for detectors and gas systems*, Nucl. Instrum. Meth. A **515** (2003) 73 (cit. on p. 10).

[22] J. A. Kadyk, *Wire chamber aging*, Nuclear Instruments and Methods in Physics Research Section A: Accelerators, Spectrometers, Detectors and Associated Equipment **300** (1991) 436, ISSN: 0168-9002,
URL: `http://www.sciencedirect.com/science/article/pii/016890029190381Y` (cit. on p. 11).

[23] , Lawrence Berkeley Nat. Lab., Lawrence Berkeley Nat. Lab., 1986,
URL: `https://cds.cern.ch/record/110508` (cit. on p. 11).

[24] P. Abbon et al., *The COMPASS experiment at CERN*,
Nuclear Instruments and Methods in Physics Research Section A: Accelerators, Spectrometers, Detectors and Associated Equipment **577** (2007) 455, ISSN: 0168-9002,
URL: `http://dx.doi.org/10.1016/j.nima.2007.03.026` (cit. on pp. 13, 21).

[25] P. e. a. (Abbon, *The COMPASS setup for physics with hadron beams*,
Nuclear Instruments and Methods in Physics Research Section A: Accelerators, Spectrometers, Detectors and Associated Equipment **779** (2015) 69, ISSN: 0168-9002,
URL: `http://www.sciencedirect.com/science/article/pii/S0168900215000662` (cit. on pp. 13, 43).

[26] *A laboratory for the world*, (2020), URL: https://cds.cern.ch/record/2723148 (cit. on p. 14).

[27] E. Mobs, *The CERN accelerator complex - August 2018. Complexe des accélérateurs du CERN - Août 2018*, (2018), General Photo, URL: http://cds.cern.ch/record/2636343 (cit. on p. 14).

[28] "LHC Guide", 2017, URL: https://cds.cern.ch/record/2255762 (cit. on p. 15).

[29] B. e. a. (Adams, *COMPASS++/AMBER: Proposal for Measurements at the M2 beam line of the CERN SPS Phase-1: 2022-2024*, tech. rep. CERN-SPSC-2019-022. SPSC-P-360, The collaboration has not yet constituted itself, thus instead of a Spokesperson currently the nominated Contact Person is acting in place.: CERN, 2019, URL: http://cds.cern.ch/record/2676885 (cit. on pp. 15, 16, 20, 67).

[30] *Gas Detectors Development Group*, https://gdd.web.cern.ch/gem-performance, Accessed: 2020-10-05 (cit. on p. 17).

[31] M. T. et al. (Particle Data Group), *Review of Particle Physics*, Phys. Rev. D **98** (3 2018) 030001, URL: https://link.aps.org/doi/10.1103/PhysRevD.98.030001 (cit. on pp. 17, 31, 54).

[32] B. Ketzer, "Running Experience with the COMPASS Triple GEM Detectors", 2006, URL: https://indico.cern.ch/event/473/contributions/1983753/attachments/954019/1353772/Ketzer.pdf (cit. on p. 18).

[33] C. Altunbas et al., *Construction, test and commissioning of the triple-gem tracking detector for compass*, Nuclear Instruments and Methods in Physics Research Section A: Accelerators, Spectrometers, Detectors and Associated Equipment **490** (2002) 177, ISSN: 0168-9002, URL: http://www.sciencedirect.com/science/article/pii/S0168900202009105 (cit. on pp. 19–21, 56).

[34] M. Altunbas et al., *Aging measurements with the Gas Electron Multiplier (GEM)*, Nuclear Instruments & Methods in Physics Research Section A-accelerators Spectrometers Detectors and Associated Equipment **515** (2001) 249 (cit. on pp. 20, 54).

[35] B. Ketzer et al., *Performance of triple GEM tracking detectors in the COMPASS experiment*, Nucl. Instrum. Meth. A **535** (2004) 314, ed. by M. Jeitler et al., [Erratum: Nucl.Instrum.Meth.A 648, 293 (2011)] (cit. on pp. 20, 21).

[36] A. Austregesilo et al., *First Results of the PixelGEM Central Tracking System for COMPASS*, Nuclear Physics B - Proceedings Supplements **197** (2009) 113, 11th Topical Seminar on Innovative Particle and Radiation Detectors (IPRD08), ISSN: 0920-5632, URL: http://www.sciencedirect.com/science/article/pii/S0920563209007671 (cit. on pp. 21, 22).

[37] F. Haas, *Two-Dimensional Partial-Wave Analysis of Exclusive 190 GeV $\pi^- p$ Scattering into the $\pi^-\pi^-\pi^+$ Final State at COMPASS (CERN)*, PhD thesis: Munich, Tech. U., 2013 (cit. on p. 21).

[38] A. Bondar et al., *Light multi-GEM detector for high-resolution tracking systems*, Nucl. Instrum. Meth. A **556** (2006) 495, arXiv: physics/0511037 (cit. on p. 22).

[39] E18 PixelGEM group, *Production Guide for a PixelGEM Detector*, tech. rep., Physik Department, Technische Uinversität München, 2008 (cit. on pp. 22, 42).

[40] A. Mathis, *From gated to continuous readout - the GEM upgrade of the ALICE TPC*, 2018, arXiv: 1803.04140 [physics.ins-det] (cit. on p. 32).

[41] A. L. Gera, "Upgrade of the ALICE Time Projection Chamber for the LHC Run 3", *2019 European Physical Society Conference on High Energy Physics*, 2020, arXiv: 2004.10520 [physics.ins-det] (cit. on p. 37).

[42] C. Lippmann, *Upgrade of the ALICE Time Projection Chamber*, (2014) (cit. on pp. 37, 40).

[43] C. Honisch, Private Communication, 2020 (cit. on pp. 41, 44, 45, 49, 50, 53).

[44] G. Iakovidis, *VMM3, an ASIC for Micropattern Detectors*, tech. rep. ATL-MUON-PROC-2018-003, CERN, 2018, URL: http://cds.cern.ch/record/2309951 (cit. on p. 44).

[45] L. Jones, *APV25-S1: User guide version 2.2*, RAL Microelectronics Design Group, 2001, URL: https://cds.cern.ch/record/1069892 (cit. on p. 44).

[46] N. Wilkinson et al., *A review of aerosol jet printing—a non-traditional hybrid process for micro-manufacturing*, The International Journal of Advanced Manufacturing Technology **105** (2019) (cit. on p. 44).

[47] Michael Hösgen, *GEM Detectors for the Tracking System of the Missing Energy Experiment NA64 at CERN SPS*, Master Thesis, 2017 (cit. on p. 51).

[48] Boris Grube, *The Trigger Control System and the Common GEM and Silicon Readout for the COMPASS Experiment*, Diploma Thesis, 2001, URL: https://wwwcompass.cern.ch/compass/publications/theses/2001_dpl_grube.pdf (cit. on p. 52).

[49] M. Raymonda et al., "The CMS Tracker APV 25 0.25 um CMOS Readout Chip", 2000 (cit. on pp. 55–57).

[50] M. Brice, "View from the crane of the COMPASS experiment facility.", 2011, URL: https://cds.cern.ch/record/1370231 (cit. on p. 67).

APPENDIX A

Appendix

The appendix contains impressions of the COMPASS spectrometer (A.1), data sheets of materials (A.2), a cost saving design of the GEM frame (A.3) and content of the APV front-end debugging (A.4).

A.1 Impressions of the COMPASS Spectrometer

In this part some pictures are shown which were taken while the unmounting of a GEM station at the COMPASS spectrometer. At the end a detailed view of the 2009 spectrometer setup is shown with pictures of the crain view in different positions along the setup.

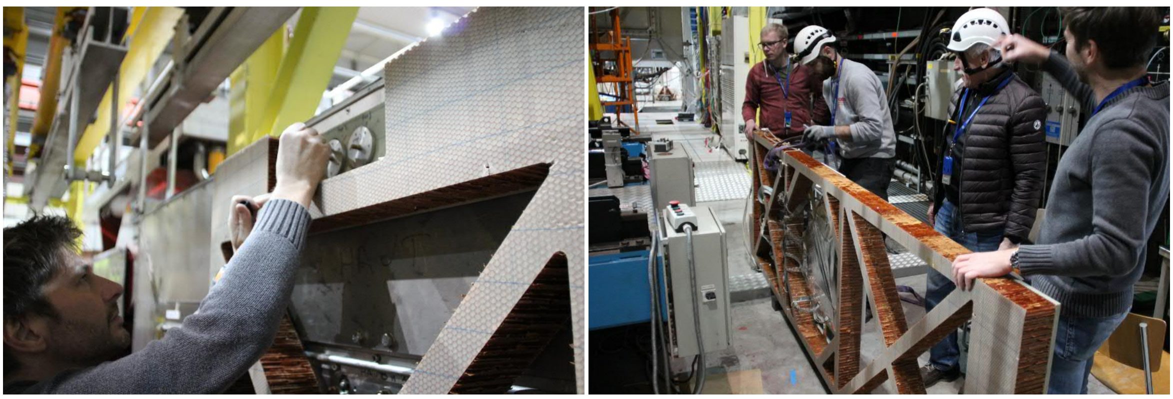

Figure A.1: Unmounting of the GEM station and preparation for the transport with the crane.

Figure A.2: Transport and temporal placement on SM1 and covering with foil.

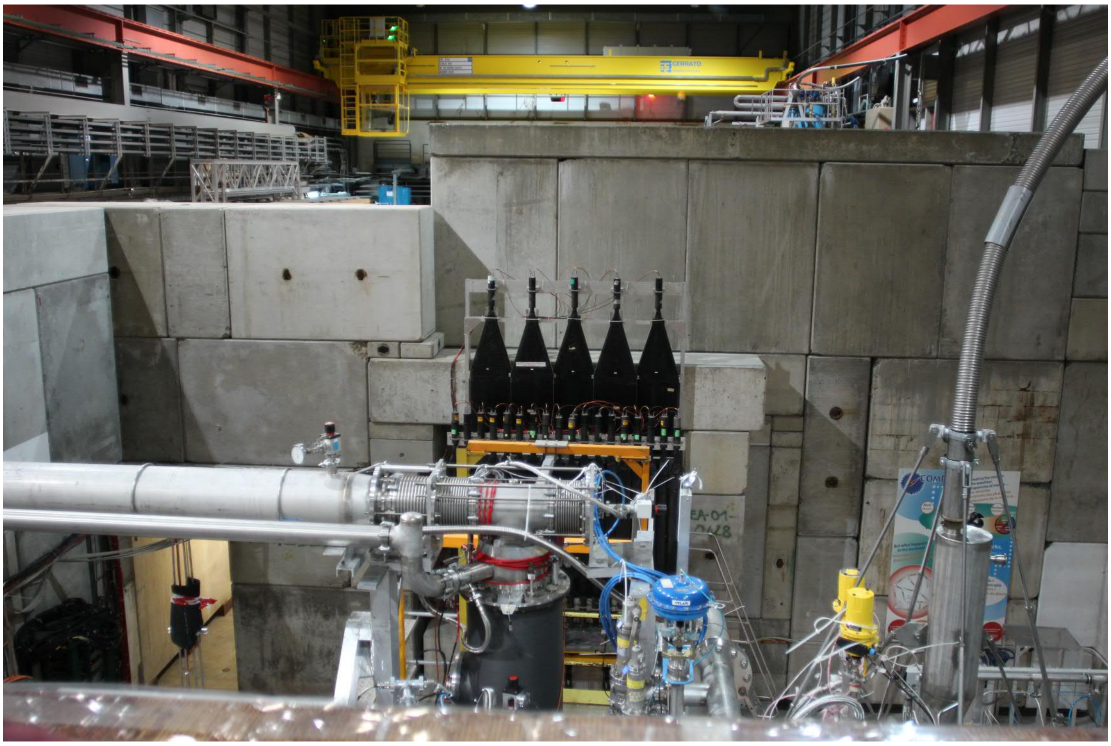

Figure A.3: Upstream view from the top of SM1.

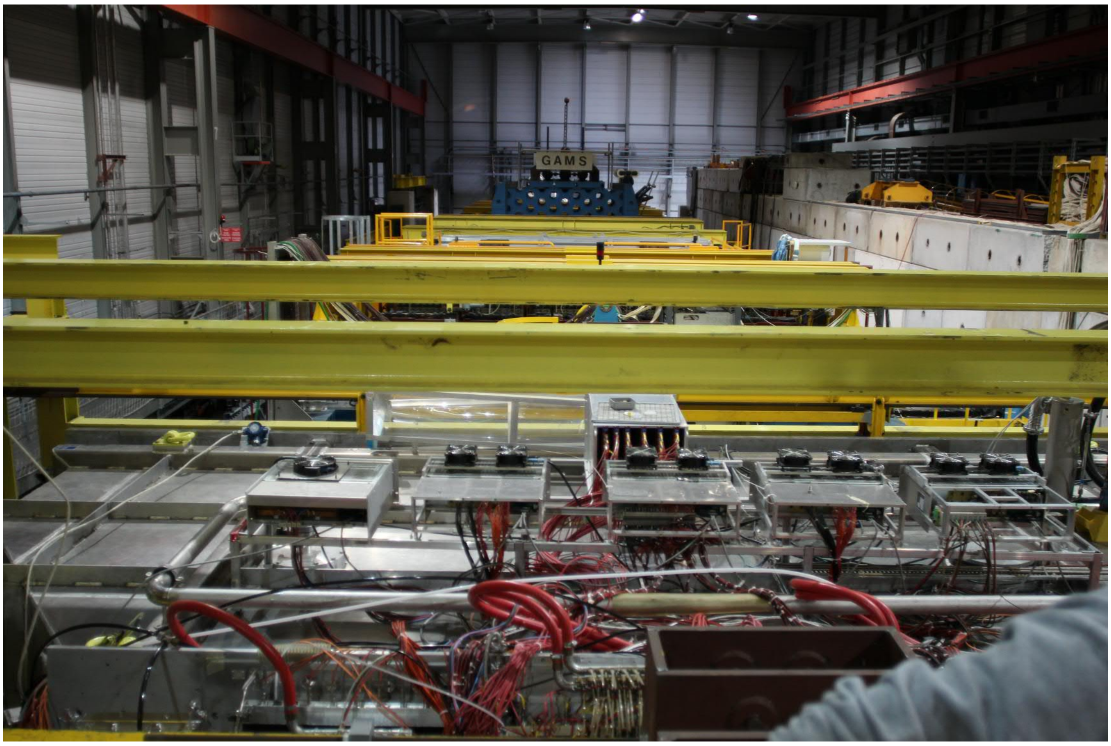

Figure A.4: Downstream view from the top of SM1.

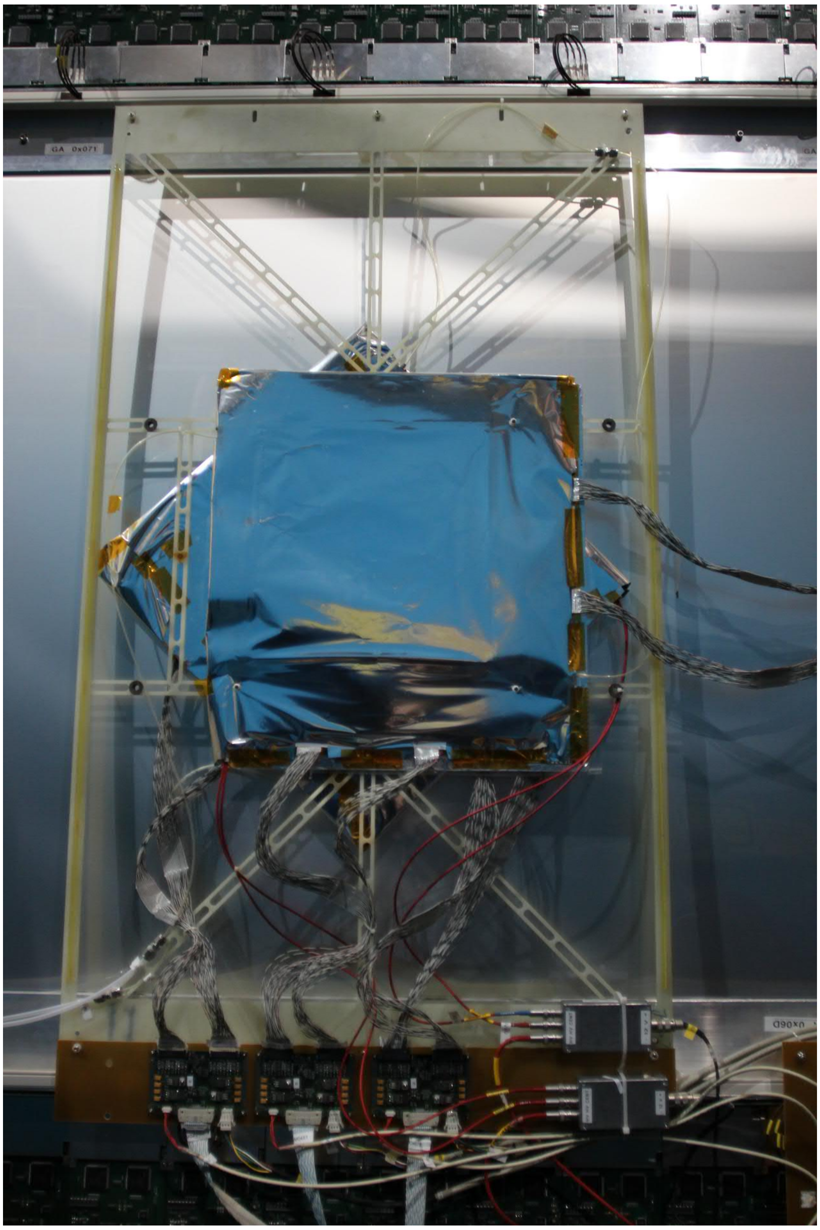

Figure A.5: CG1G station in front of a MWPC.

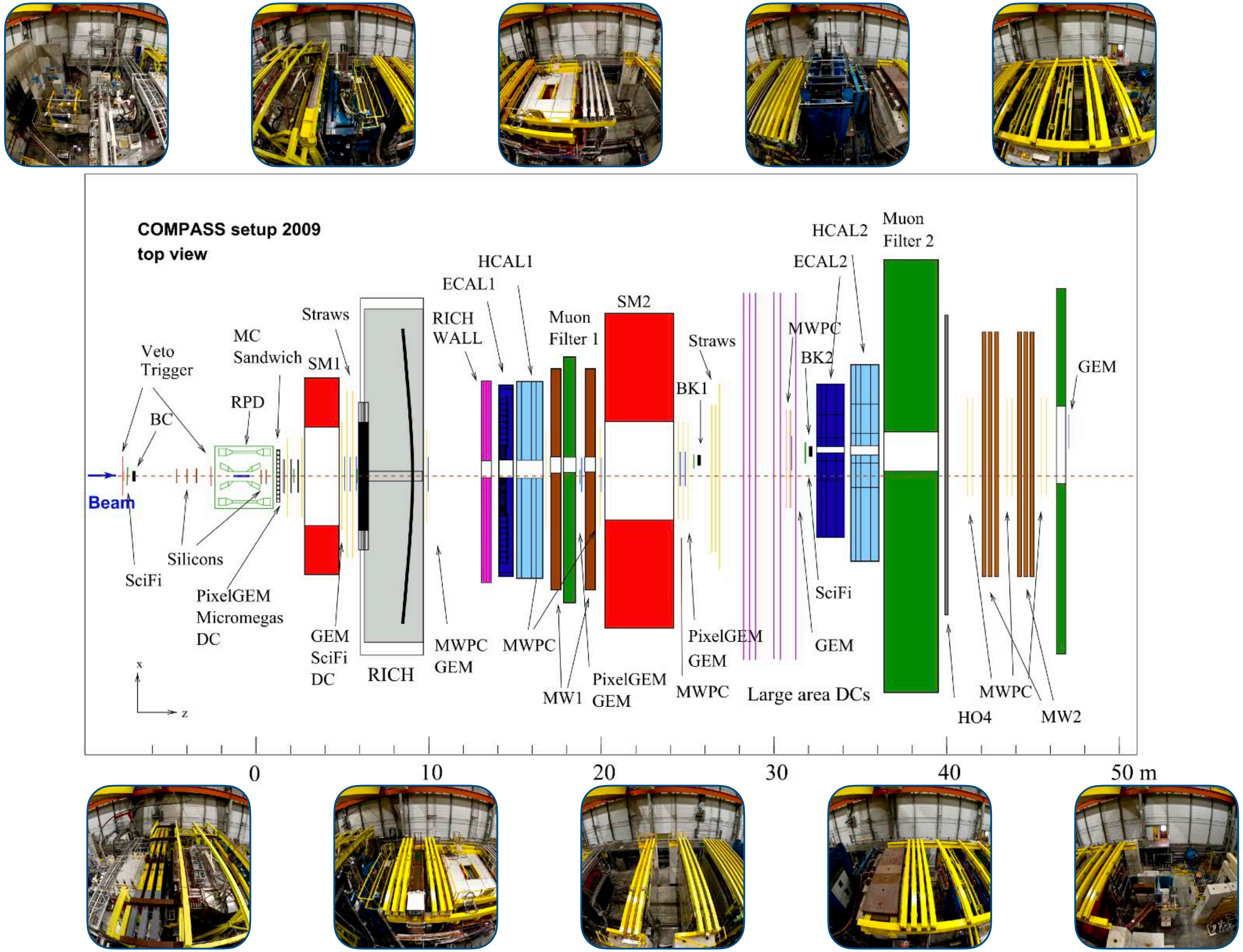

Figure A.6: Top view of the 2009 Compass spectrometer setup [29]. Pictures taken from [50].

A.2 Data Sheets

Laminates

VETRONIT EGS 103

- High Pressure Laminate suitable for demanding mechanical and electrical applications even at elevated temperatures
- Good electrical properties
- G-11 type, TI 155°C

General description
Vetronit EGS 103 is an insulating laminate made of glass fabric bonded with epoxy resin. It has a temperature index of 155°C.

Specifications
IEC/DIN EN 60893 EP GC 203
DIN 7735 HGW 2372.4 (*)
NEMA LI-1 G-11

(*) no longer valid since March 2003

RoHS Directive
Hazardous products listed in the EU-directive 2002/95/CE (RoHS-directive), §4 section 1, are not used as ingredients in this material.

Colour
Light beige

Application
Electrical insulation
High temperature resistant machine parts
Vanes and slides for compressors and vacuum pumps
Thermal insulation
Construction of jigs and fixtures

Former denominations
EGS 103
Vetronite 64.010

Form of delivery
Sheet formats 1170 x 1070 mm and 2070 x 1070 mm (up to 40 mm thickness).
Special size 4270 x 1270 mm (and others) on request.
Tolerance of formats 0 / - 30 mm
Thickness in range of 0,2 to 100 mm
Thickness tolerances acc. to DIN EN 60893-3-2

Material also available as cut to size panels and machined parts.
Other dimensions and thicknesses on request.

Processing
Machining with carbide or diamond tools.
For water jet cutting we recommend to add silica sand to the water and to drill through-holes prior to machine.

		Value	Test norm
Mechanical properties			
Flexural strength	MPa	400	ISO 178
Flexural strength at 150°C / 1h	MPa	200	ISO 178
Modulus of elasticity	MPa	24000	ISO 178
Edgewise notched impact strength Charpy	kJ/m²	55	ISO 179
Flatwise compressive strength	MPa	400	ISO 604
Compressive strength //, at 23°C	MPa	250	ISO 604
Tensile strength	MPa	300	ISO 527
Electrical properties			
Insulation resistance after the immersion in water	Ω	1.00E+12	IEC 60167
Breakdown voltage //, 90°C in oil	kV	80	IEC 60243-1
Flatwise electric strength, 90°C in oil	kV/mm	20	IEC 60243-1
Dissipation factor at 1 MHz		0.02	IEC 60250
Relative permittivity at 1 MHz		5.0	IEC 60250
Comparative tracking index CTI	V	180	IEC 60112
Thermal properties			
Temperature index (TI)	°C	155	IEC 60216
Thermal conductivity	W/m.K	0.30	DIN 52612
Coefficient of linear expansion //	1.0E-6 / K	15	DIN 53752
Physical properties			
Density	g/cm³	1.85	ISO 1183
Water absorption 24h 23°C	mg / %	12 / 0.06	ISO 62

Von Roll Deutschland GmbH
D-86199 Augsburg
www.vonroll.com

VETRONIT EGS 103

WH QGEMA 06-03-2012

Figure A.7: Material used for the Frames delivered by vonRoll©.

Art.Nr. 11755-03

B-Cool 755

Beschreibung

B-Cool 755 ist ein wassermischbarer, chlorfreier Kühlschmierstoff auf Mineralölbasis. Das Produkt zeichnet sich durch seine Schaumarmut in Hart- und Weichwasser, gute Stabilität, gute Ferrokorrosionsschutzeigenschaften und geringen Verbrauch aus.

Einsatzbereich

B-Cool 755 ist für die Zerspanung von weichen und harten Aluminiumlegierungen, Titan, Nickelbasislegierungen, hitzebeständigen Stählen und INOX geeignet.

Produkteigenschaften		Nutzen
Herrvorragende Verträglichkeit zu allen Alulegierungen	➔	ausgezeichnete Anwendungsbreite auch bei anspruchsvollem Materialmix
Sehr hohe Stabilität der Emulsion	➔	lange Standzeit geringe Entsorgungskosten
Sehr schaumarm in Hart- und Weichwasser	➔	ideal für hohe Schnittgeschwindigkeiten und Hochdruckanwendungen
Hervorragendes Spülvermögen und Abfliessverhalten	➔	äusserst geringer Verbrauch

Physikalisch-chemische Daten

	Konzentrat	Emulsion
Farbe	gelblich	milchig
Mineralölgehalt	24 %	
Wassergehalt		
Dichte bei 20°C	0.94 g/cm^3	
Viskosität bei 40°C	168 mm^2/s	
Flammpunkt	128°C	
pH-Wert (Frischemulsion)		8.6 – 9.6
pH-Wert (nach 2-3 Tagen)		9.2
Faktor Refraktometer		1.0

Hinweis

Im Produkt nicht enthalten sind:
*Chlor, Schwermetalle, Bor, Silikon, Bakterizid, Formaldehyddepot, Nitrosamine, Glycolether.

Die aufgeführten Chemikalien sind nicht Teil der Formulierung, jedoch können Spuren davon nicht vollständig ausgeschlossen werden.

Blaser Swisslube AG
CH-3415 Hasle-Rüegsau • Tel. 034 460 01 01 • Fax 034 460 01 00
www.blaser.com

Blaser. SWISSLUBE

Figure A.8: Cutting fluid used by the HISKP workshop to wet mill the Frames.

Technisches Datenblatt

Beschreibung: CM-Preg F-T40 580/1270 CP002 32

Die CP002 Systeme sind schlagzäh und brandgehämmte modifizierte Epoxy Systeme. Das Harzsystem ist hervorragend für industrielle Anwendungen geeignet um hohe Lasten aufzunehmen. Das CP002 kann mit Gelegen, Geweben und UD verarbeitet werden

Besondere Merkmale:

FAR 25.853
Gute Klebe Eigenschaften
Schlagzäh Modifiziertes System
Einsetzbar in einem weiten Temperaturbereich

Matrixeigenschaften:

		CP002
min Viskosität	mPas	600
T_g (1h/120°C)	°C	125
Farbe		natur
Sonstiges		tbd

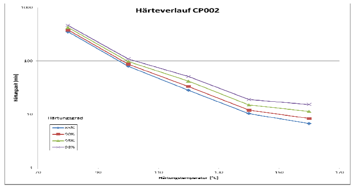

Für weiterführende Informationen wenden Sie sich bitte an
c-m-p GmbH Industrieparkstr 15, 52525 Heinsberg, Tel.: +49 (0) 2452 1572110
www.c-m-p-gmbh.de support@c-m-p-gmbh.de 1 / 3

Technisches Datenblatt

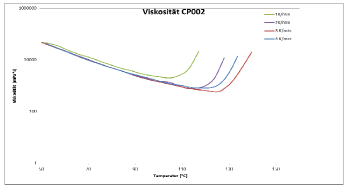

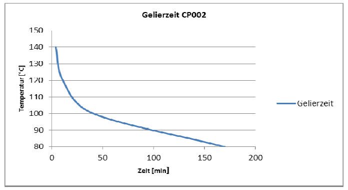

Lagerzeit und Lagerkonditionen:

21 Wochen	bei	20 °C
12 Monate	bei	-18 °C

Verarbeitungshinweise:

Prepregs mit den CP002 Harzsystemen können mit allen gängigen Methoden verarbeitet werden. Dabei liegt das typsiche Temperaturfenster zwischen 75°C und 160°C. Die Aushärtezeit variiert dadurch von 10 Minuten bis zu 4 Stunden.

Für weiterführende Informationen wenden Sie sich bitte an
c-m-p GmbH Industrieparkstr 15, 52525 Heinsberg, Tel.: +49 (0) 2452 1572110
www.c-m-p-gmbh.de support@c-m-p-gmbh.de 2 / 3

Technisches Datenblatt

Prepreg Eigenschaften:

Textur: Epoxid-Glas-Gewebe-Prepreg Köper 2/2

Faserflächengewicht:	g/m²	DIN	29971	580
Harzgehalt:	%	DIN	2557 C	32
Prepregflächengewicht	g/m²	DIN	2557 C	853
Breite:	mm			1.270

Laminat-Eigenschaften (Beispiele - HT - Kohlenstofffaser / 60 Vol%)

Artikel				CM-Preg F	CM-Preg T
Art				Köper 2/2	UD
FFG	g/m²			245	200
Zugfestigkeit 0°	MPa	DIN	ISO 527	1100	2300
E-Modul 0°	GPa	DIN	ISO 527	70	140
Biegesteifigkeit	MPa	DIN	ISO 14125	1050	1700
Biege-Modul 0°	GPa	DIN	ISO 14125	62	125
ILSF	MPa	DIN	EN 2563	70	85

weiter mechanische Kennwerte auf Anfrage möglich

Sonstiges:

Alle vorstehende Daten und Angaben basieren auf internen Untersuchungen nach unseren Qualitätsrichtlinien und sollen als Hinweise und Anhaltspunkte für eine weitere Verwendung dienen. Aus den angegebenen Daten ergibt sich keine Tauglichkeitsgarantie für bestimmte kundenspezifische Anwendungen. Anwender müssen in jedem Fall eine eigene, zweckgebundene Prüfung des Produktes durchführen.

Druckdatum 22.01.2020

Für weiterführende Informationen wenden Sie sich bitte an
c-m-p GmbH Industrieparkstr 15, 52525 Heinsberg, Tel.: +49 (0) 2452 1572110
www.c-m-p-gmbh.de support@c-m-p-gmbh.de 3 / 3

Figure A.9: Skin Material used by Piekenbrink Composite: CM-Preg-F-T40 580/1270 CP 002 32 from CMP.

A.3 Alternative GEM Frame Design

The idea behind the fragmentation of the frames is to lower the cost for mass production. The fragment that can be used to build a GEM frame is shown in fig. A.10. Four of these could be made from the cut out in the centre of a readout frame. That means that the raw material can be used with less wastage which directly lowers the overall costs.

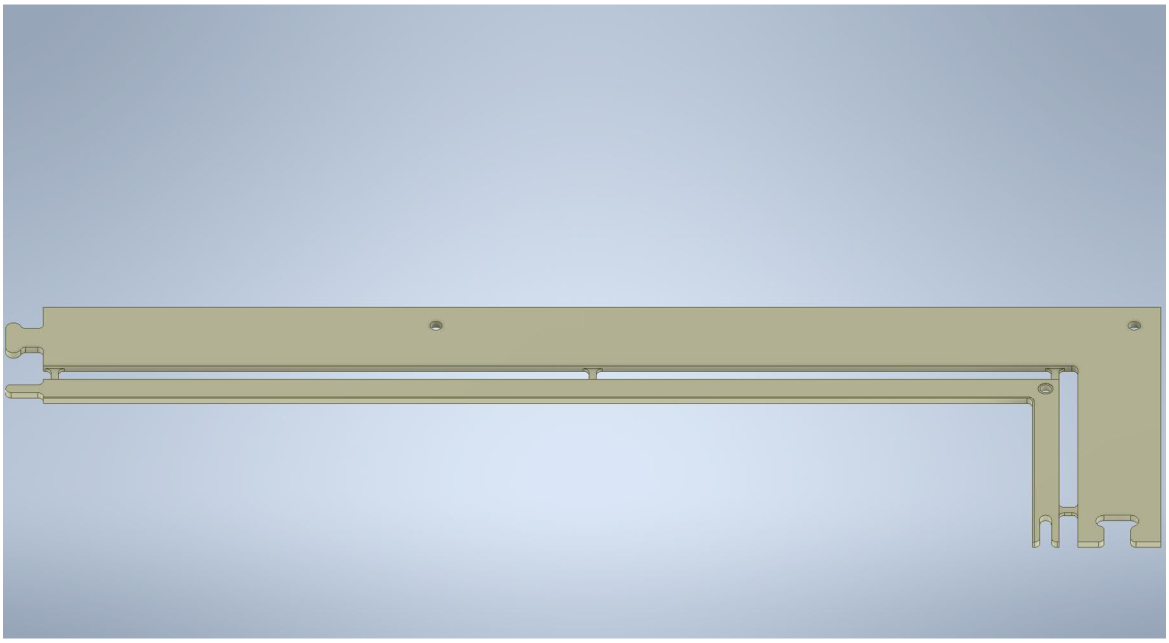

Figure A.10: Fragment of a GEM frame. Four of these result in one GEM frame.

The feasibility of this solution has not been tested until now. But it should be considered in further prototyping.

A.4 APV Debugging

In the following the new APV front-end board will be called new APV (ID1 was used) and the old APV front-end board old APV. In this part the debugging process of new APV will be described. For comparison an old APV was used for cross checking behaviours. Therefore, the pictures are discussed in parts of two.

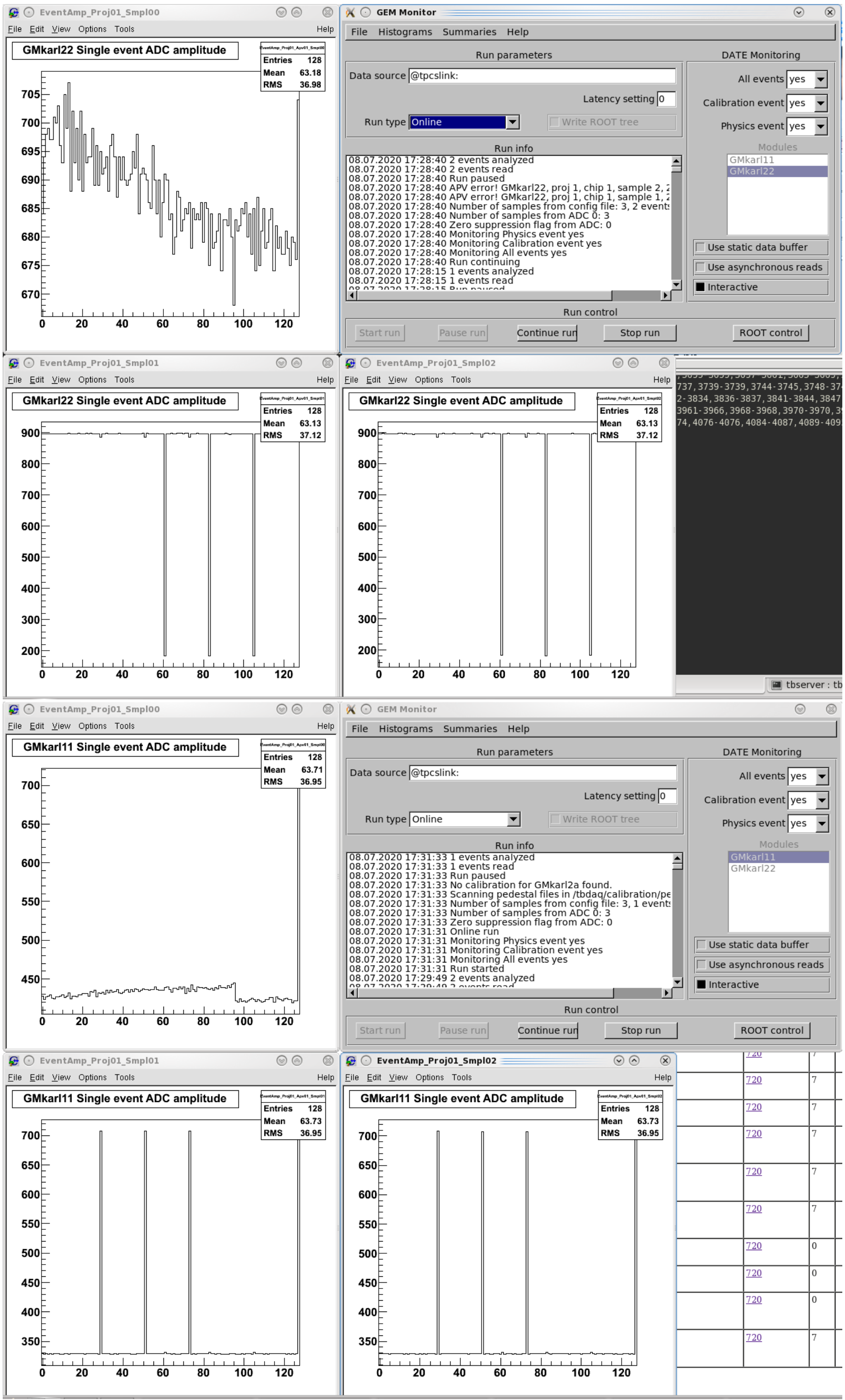

Figure A.11: Old APV seen in the upper picture and the new APV in the lower. APVs operated in single sample mode with gemMonitor reading three samples. By this one sees the synchronisation tics in the last two samples. This tics are send over the whole range by the APV. Here one sees that this seems to be turned around for the new APV. This issue was solved by switching the polarity off the analogue signal from the new APV.

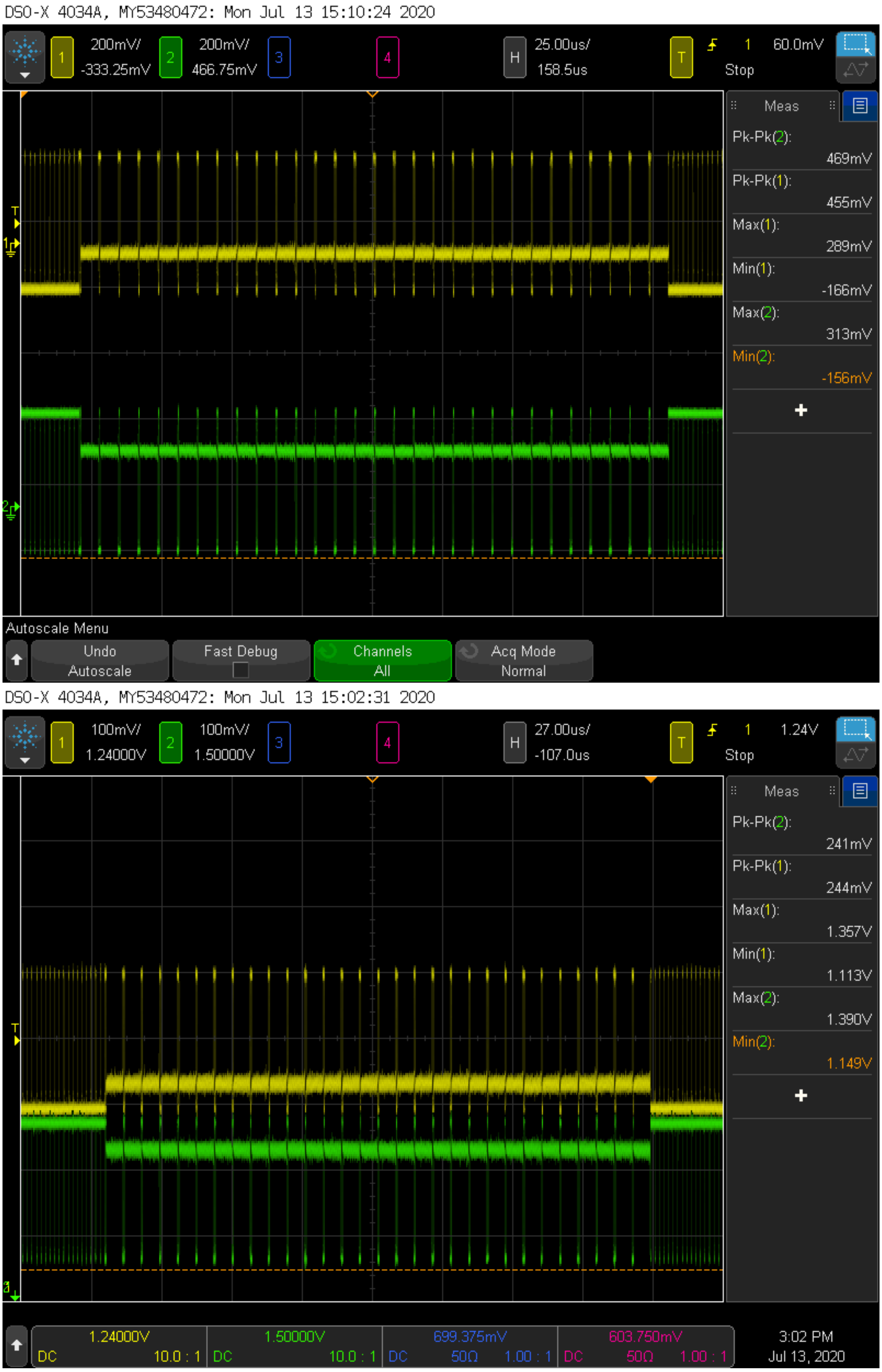

Figure A.12: Old APV seen in the upper picture and the new APV in the lower. Here the analogue outputs of the APVs were monitored with the oscilloscope. The shape is equal for both but the amplitude differs roughly by a factor of two. This was solved by a change of resistor-values on the new APV.

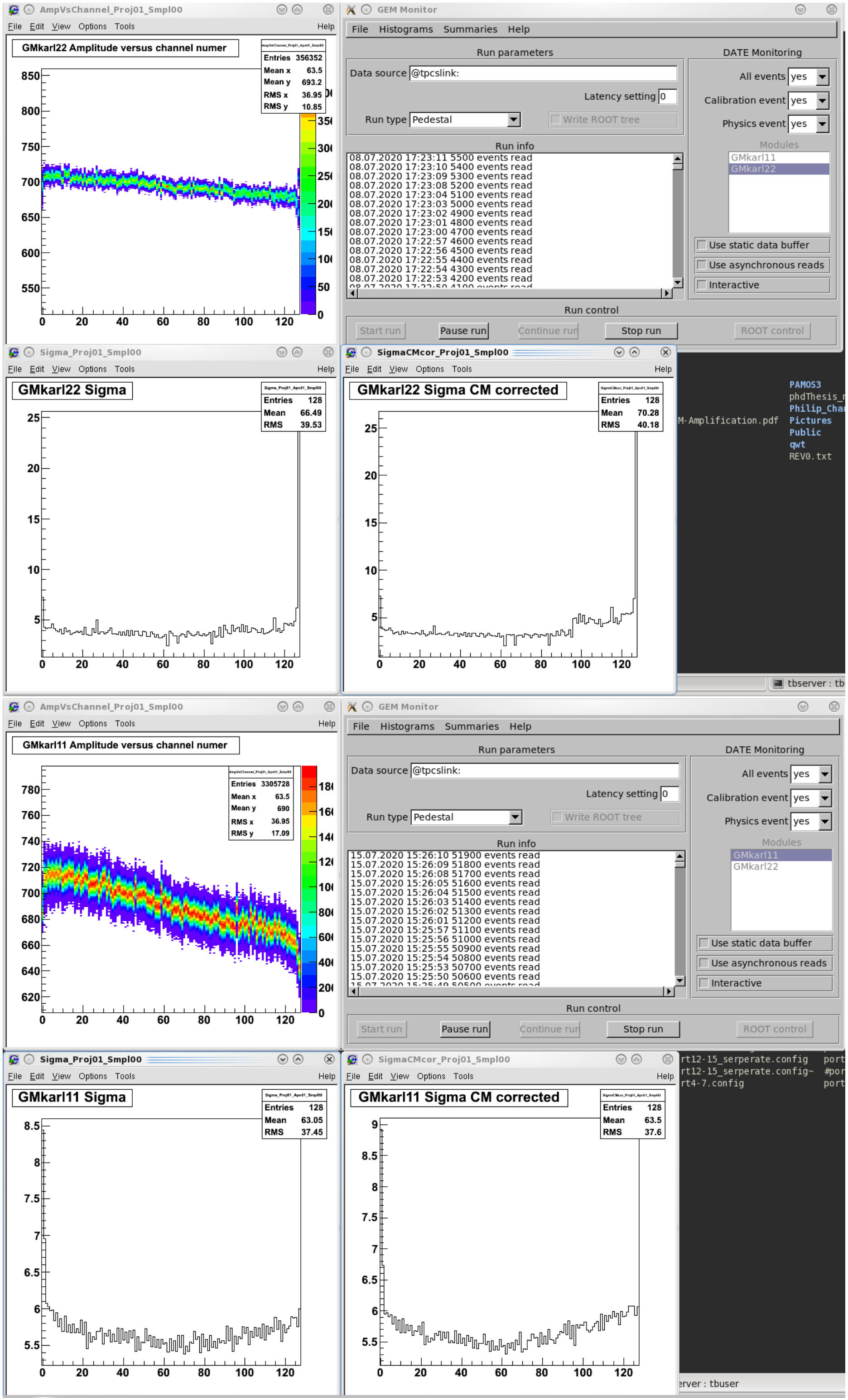

Figure A.13: Old APV seen in the upper picture and the new APV in the lower. Here the gemMonitor is used to have a look at the pedestals. The new APV has an additional input capacitance (additional 30 pF for channel 2-128) due to the detector dummy.

List of Figures

List of Tables